Emulsification in microfluidic Y- and T-junctions

Maartje Louisa Josepha Steegmans

Propositions

1. The small difference in angle between Y- and T-junctions has surprisingly great influence on the droplet formation.
   This thesis

2. The effect of the disperse phase on the droplet size in a microfluidic Y-junction is negligible compared to the effect of the continuous phase.
   This thesis

3. The association of the word 'chips' makes research with microchips hard to digest for a layman.

4. For two emulsion droplets to be as identical as the Dutch proverbial 'two droplets of water', it is advisable to use a hydrophobic Y-junction.

5. Interfacial dynamics is generally wrongfully neglected in process technological literature.

6. Organising life takes time.

7. A dual nationality makes you always feel being abroad.

Propositions accompanying the thesis
'Emulsification in microfluidic Y- and T-junctions'
Maartje Louisa Josepha Steegmans
Wageningen, 30 October 2009

Stellingen

1. Het kleine verschil in invalshoek tussen Y- en T-splitsingen heeft verrassend grote gevolgen voor de druppelvorming.
   Dit proefschrift

2. Het effect van de disperse fase op de druppelgrootte in een Y-splitsing valt in het niet vergeleken bij het effect van de continue fase.
   Dit proefschrift

3. De associatie bij het woord 'chips' maakt onderzoek met microchips moeilijk behapbaar voor de leek.

4. Om twee emulsiedruppels als twee druppels water op elkaar te laten lijken, valt het aan te bevelen een hydrofobe Y-splitsing te gebruiken.

5. Grensvlakdynamica wordt doorgaans ten onrechte verwaarloosd in procestechnologische literatuur.

6. Het leven organiseren kost tijd.

7. Een dubbele nationaliteit zorgt ervoor dat je je altijd in het buitenland waant.

Stellingen behorend bij het proefschrift
'Emulsification in microfluidic Y- and T-junctions'
Maartje Louisa Josepha Steegmans
Wageningen, 30 oktober 2009

Emulsification in microfluidic Y- and T-junctions

Maartje Louisa Josepha Steegmans

Thesis committee

Thesis supervisor

Prof. dr. ir. R.M. Boom

Professor of Food Process Engineering, Wageningen University

Thesis co-supervisor

Dr. ir. C.G.P.H. Schroën

Assistant professor, Food Process Engineering group, Wageningen University

Other members

Prof. dr. E. van der Linden

Wageningen University

Dr. ir. M.F. Kemmere

FrieslandCampina Corporate Research, Deventer

Prof. dr. J. Meuldijk

Hasselt University, Belgium

Prof. dr. ir. P.M.M. Bongers

Eindhoven University of Technology

This research was conducted under the auspices of graduate school VLAG.

Emulsification in microfluidic Y- and T-junctions

Maartje Louisa Josepha Steegmans

Thesis

submitted in partial fulfilment of the requirements for the degree of doctor
at Wageningen University
by the authority of the Rector Magnificus,
Prof. dr. M.J. Kropff,
in the presence of the
Thesis Committee appointed by the Doctorate Board
to be defended in public
on Friday 30 October 2009
at 4 PM in the Aula

Maartje Louisa Josepha Steegmans
Emulsification in microfluidic Y- and T-junctions, 142 pages.

Thesis Wageningen University, Wageningen, NL (2009)
with summaries in Dutch and English

ISBN: 978-90-8585-457-9

Contents

Chapter 1

Introduction

In this chapter, emulsions and currently available emulsification techniques are introduced. Subsequently, the basics of the emulsion droplet-formation process will be described, including the effect of interfacial tension. From this, the aim and outline of the thesis follow.

Emulsions

Many everyday products consist partly or entirely of emulsions, *i.e.* dispersions of two immiscible liquids. Milk is an example found ready-made in nature [1, 2]. Most other emulsion-based products are manufactured: *e.g.* mayonnaise, salad cream, butter, cream-liqueurs, ice cream, but also non-food products like body lotion, paint, and bitumen. Food industry mainly uses emulsions consisting of oil and water, which are divided into oil-in-water emulsions for oil droplets in water and water-in-oil emulsions for water droplets in oil [3].

Emulsification

Traditionally, emulsions are prepared (homogenised) in high pressure, rotor-stator, ultrasound or high-speed systems [2, 4, 5]. Unfortunately, these techniques require a lot of energy [6], which is mostly dissipated in the product in the form of heat, therewith possibly causing damage to (heat-)sensitive compounds like proteins. Besides, traditionally prepared emulsions are polydisperse. For a rotor-stator system [7] and a microfluidiser [8] a polydispersity index (standard deviation to

average droplet size ratio) of roughly 60 % was observed. Finally, it is hard to control the mean droplet size with traditional techniques.

Therefore, industry is looking for milder techniques with which droplet size can be better controlled. Membrane emulsification meets these criteria with respect to reproducibility in droplet size and lower energy input [9-11], and further both oil-in-water and water-in-oil emulsions can be formed depending on the surface properties of the chosen membrane, *i.e.* hydrophilic or hydrophobic, respectively [10-13]. The polydispersity index for membranes is lower than for traditional emulsification techniques. Typically a value between 10 and 17 % is mentioned for SPG-membranes [14, 15], while a value of 30 % is observed for ceramic membranes [8].

Microfluidic emulsification

Emulsification with microfluidic devices tops the advantages of membrane emulsification concerning monodispersity with a polydispersity index below 5 % [16-18]. Microfluidic devices are defined geometries with channels in the order of several to hundreds of micrometers. These geometries can be used for either pre-mix emulsification (a method in which a coarse emulsion is broken up by passing through a geometry [19, 20]) or direct emulsification (a method where disperse and continuous phase are introduced separately to the device and the emulsion is formed when they contact). Depending on the surface properties of the microfluidic device either oil-in-water (hydrophilic device) or water-in-oil (hydrophobic device) emulsions are formed. In this thesis, only direct emulsification of oil-in-water emulsions will be discussed; for details on pre-mix emulsification the reader may consult the work of van der Zwan [21].

Direct emulsification with microfluidic devices is advantageous as the resulting emulsions are monodisperse. Therefore, phase separation due to Ostwald ripening is prevented (see section 'Surfactants and interfacial tension'). Besides, the emulsion droplets are in the order of micrometers and therefore product instability due to gravitational separation, *i.e.* creaming for oil-in-water emulsions or

sedimentation for water-in-oil emulsions, is delayed, and sometimes even prevented.

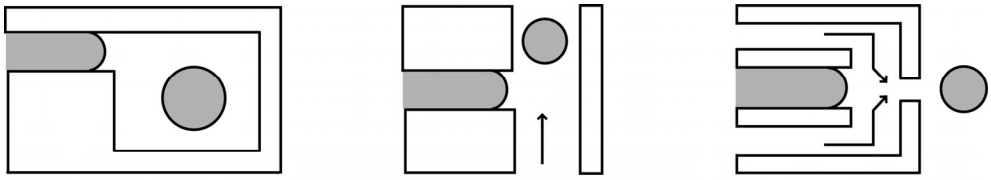

Figure 1: Outline of some microfluidic emulsification geometries. a. cross-section of a microdevice with a depth difference at the junction (a microchannel). An emulsion droplet is formed when the disperse phase 'falls' from the terrace into the deeper well. Picture after van der Zwan [21] b. top view of a T-junction with a uniform depth around the junction. The disperse phase comes from the left and at the T-junction droplets detach due to the cross-flowing continuous phase (marked by the arrow). c. top view of a flow-focusing device (ψ-junction) with a uniform depth around the junction. The disperse phase indicated in grey comes from the centre and is forced through the orifice together with the continuous phase (marked by the arrows). The emulsion droplets detach due to elongation.

Various direct microfluidic emulsification geometries are discussed in literature, *e.g.* (straight-through) microchannels, T-, and ψ-junctions [22-24] (see Figure 1). Two droplet-formation mechanisms can be distinguished: one uses Laplace pressure differences for spontaneous droplet generation and the other uses shear flow to form droplets. For spontaneous droplet formation, a difference in dimensions is needed (*e.g.* a depth difference as shown in Figure 1a.) In these (straight-through) microchannels, the incipient oil droplet spontaneously changes from a flat disc shape to a spherical droplet [17, 25-27] and detaches. For the second mechanism, shear flow is deployed to detach emulsion droplets by cross-flow or by co-flow [28-32]. The droplet size is determined by the flow rates of the continuous and disperse phases, and by other properties like interfacial tension and viscosity [28, 33-35].

The spontaneous and shear-driven mechanisms yield a comparable polydispersity index (below 5 %), but the droplet-formation rate is notably higher for shear-driven mechanisms [17, 33]. Nevertheless, for both mechanisms, many microfluidic

geometries in parallel are needed in order to obtain industrially relevant volume throughputs. In literature, some studies with a limited number of parallelised geometries are available [26, 32, 35, 36]. However, it is expected that truly large-scale application is only feasible when the droplet-formation mechanism is understood in more detail than is currently the case. Specifically, the influence of the dynamic interfacial tension during emulsification is still a field in need of thorough investigation.

Droplet-formation mechanism

In general, it is assumed that emulsification with membranes or microfluidic devices can be described with a two-step model consisting of a droplet growth step and a detachment step (*i.e.* break-up) [30, 37, 38]. In some cases, when detachment is very fast, the droplet size is solely determined by the droplet growth step and therefore droplet formation can be described with a one-step model.

In shear-driven (microfluidic) emulsification, the droplet growth step is usually described with a force-balance model. The main force keeping the incipient droplet attached to the oil bulk is the interfacial tension force, which is proportional to the interfacial tension. An oil droplet detaches when this force is exceeded, in general by the shear force exerted by the aqueous phase. Based on this force-balance model, the droplet size is dependent on the (dynamic) interfacial tension and the continuous-phase flow. Other parameters like the design of the microfluidic geometry do play a role and therefore it is important to understand the droplet-formation mechanism in more detail.

Surfactants and interfacial tension

Emulsion droplets are thermodynamically unstable and therefore a surfactant or emulsifier is added to extend physical shelf-life [2]. Surfactants are surface-active compounds, which adsorb to the interface and may form a protective layer against

coalescence. In addition, surfactant adsorption causes a decrease in interfacial tension (Gibbs adsorption) until an equilibrium value is reached. This decrease reduces the driving force for Ostwald ripening in polydisperse emulsions and facilitates droplet break-up during emulsification, as described in the previous section.

During emulsification the interfacial tension may not be constant (*i.e.* dynamic) since fresh interface is formed and surfactants adsorb continuously. As a result, the interfacial tension can be equal to or anything in between the interfacial tension of the pure liquids and the equilibrium interfacial tension. Non of the current tensiometric techniques allow measurement at liquid-liquid interfaces subjected to shear and expanding at rates relevant to (microfluidic) emulsification. Therefore, it is difficult to evaluate the actual (dynamic) interfacial tension value at droplet break-up and in literature mostly the equilibrium interfacial tension or the interfacial tension of the pure liquids is used, even though this might not reflect the actual value. If better estimates of the actual interfacial tension during emulsification would be available, this would immediately be reflected in better understanding of the droplet-formation mechanism.

Essentials for new emulsification technologies

In summary, to make a significant step forward in emulsification technology, the emulsion droplets should be monodisperse and small. For this purpose, microfluidic devices are suited. However, to come to large-scale application, it is essential that the droplet-formation mechanisms are known in detail, including effects of dynamic interfacial tension, and that the devices can be used in parallel, ideally at high droplet formation frequencies.

Research aim and thesis outline

The aim of this project was to develop a new microfluidic emulsification technique with potential for scale up towards production of large volumes of monodisperse emulsion. We chose to study shear-driven microfluidic devices, especially Y-junctions, due to the high emulsion droplet-formation frequency per junction and the successful parallelisation (see sections 'Microfluidic emulsification' and 'Essentials for future emulsification technologies'). Y-junctions are very little studied in literature [31, 35, 39], and their droplet-formation mechanism is hardly understood. Therefore, in this thesis the effect of (dynamic) interfacial tension, but also flow rate, viscosity, and junction design, on the emulsion droplet-formation mechanism and the emulsion droplet size were studied.

In literature, studies on microfluidic T-junctions are reported considerably more frequently than those on Y-junctions. As the geometry of Y-junctions seems very close to that of T-junctions, data from the latter were used as a starting point to investigate the properties involved in shear-driven microfluidic emulsification. Therefore, in Chapter 2 we bring together T-junction data from various literature sources, and use statistical analysis to investigate them.

Chapter 3 is the first chapter which reports on emulsification with microfluidic Y-junctions. To characterise droplet formation in these devices a model system with a static interfacial tension was used. The droplet size was described with a force-balance model that uses the capillary number of the continuous phase and the channel dimensions as parameters.

As only one Y-junction design was investigated in Chapter 3, in Chapter 4 the effect of (Y-)junction design on droplet size was investigated. The influence of Y-junction angle, channel length and width were experimentally tested and used as the basis for an outline of a mass-parallelised setup. Besides, Y-junctions were compared to T-junctions.

The disperse phase viscosity was not varied in Chapter 3 and 4, and therefore in Chapter 5 this aspect was covered. The force-balance model derived in Chapter 3 was adapted based on the cross-sectional area of the incipient squeezed droplet (head), and the effects of the continuous phase, channel dimensions, resistance with the wall, and disperse-phase viscosity were charted.

In Chapter 6, Y-junctions were used as a new tensiometric technique to quantify dynamic interfacial tension at sub-millisecond time scales and under high shear conditions relevant to emulsification and which are inaccessible with any current tensiometric technique.

Finally, in Chapter 7 the characteristics for Y-junctions obtained in this thesis were compared to other shear-driven (microfluidic) emulsification techniques. Moreover, the feasibility of emulsification with Y-junctions is discussed through the specific volume and area of a mass-parallelised microfluidic Y-junction device which can process disperse phase at 1 $m^3 \cdot h^{-1}$, and through the energy input.

References

1. A. J. Gijsbertsen-Abrahamse, A. van der Padt and R. M. Boom, *Journal of Membrane Science*, 2004, **230**, 149-159.
2. D. J. McClements, *Food Emulsions - principles, practices and techniques*, 2nd edn., CRC Press, 2005.
3. V. Schröder, O. Behrend and H. Schubert, *Journal of Colloid and Interface Science*, 1998, **202**, 334-340.
4. V. Schröder and H. Schubert, *Colloids and Surfaces A-Physicochemical and Engineering Aspects*, 1999, **152**, 103-109.
5. S. M. Joscelyne and G. Trägårdh, *Journal of Food Engineering*, 1999, **39**, 59-64.
6. P. Walstra and P. E. A. Smulders, in *Modern aspects of emulsion science*, ed. B. P. Binks, The royal Society of Chemistry, Cambridge, 1998, pp. 56-99.

7. K. Urban, G. Wagner, D. Schaffner, D. Roglin and J. Ulrich, *Chemical Engineering & Technology*, 2006, **29**, 24-31.
8. U. Lambrich and H. Schubert, *Journal of Membrane Science*, 2005, **257**, 76-84.
9. A. Gijsbertsen-Abrahamse, *membrane emulsification: process principles*, Wageningen University, 2003.
10. S. M. Joscelyne and G. Trägårdh, *Journal of Membrane Science*, 2000, **169**, 107-117.
11. M. Rayner and G. Trägårdh, *Desalination*, 2002, **145**, 165-172.
12. R. Katoh, Y. Asano, A. Furuya, K. Sotoyama and M. Tomita, *Journal of Membrane Science*, 1996, **113**, 131-135.
13. K. Sotoyama, Y. Asano, K. Ihara, K. Takahashi and K. Doi, *Journal of Food Science*, 1999, **64**, 211-215.
14. C. Charcosset, *Journal of Food Engineering*, 2009, **92**, 241-249.
15. G. T. Vladisavljevic, I. Kobayashi, M. Nakajima, R. A. Williams, M. Shimizu and T. Nakashima, *Journal of Membrane Science*, 2007, **302**, 243-253.
16. J. H. Xu, S. W. Li, J. Tan, Y. J. Wang and G. S. Luo, *AIChE Journal*, 2006, **52**, 3005-3010.
17. I. Kobayashi, K. Uemura and M. Nakajima, *Colloids and Surfaces A-Physicochemical and Engineering Aspects*, 2007, **296**, 285-289.
18. M. L. J. Steegmans, C. G. P. H. Schroën and R. M. Boom, *Langmuir*, 2009, **25**, 3396-3401.
19. D. R. Link, S. L. Anna, D. A. Weitz and H. A. Stone, *Physical Review Letters*, 2004, **92**, 054503-054501-054503-054504.
20. E. van der Zwan, K. Schroën, K. van Dijke and R. Boom, *Colloids and Surfaces A-Physicochemical and Engineering Aspects*, 2006, **277**, 223-229.
21. E. van der Zwan, *Emulsification with microstructured systems - process principles*, Wageningen University, 2008.
22. S. v. d. Graaf, T. Nisisako, C. G. P. H. Schroën, R. G. M. v. d. Sman and R. M. Boom, *Langmuir*, 2006, **22**, 4144-4152.
23. M. Nakajima, *RIKEN Review*, 2001, **36**, 21-23.
24. T. Nisisako, T. Torii and T. Higuchi, *Chemical Engineering Journal*, 2004, **101**, 23-29.

25. T. Kawakatsu, G. Trägårdh, Y. Kikuchi, M. Nakajima, H. Komori and T. Yonemoto, *Journal of Surfactants and Detergents*, 2000, **3**, 295-302.
26. I. Kobayashi, M. Nakajima, K. Chun, Y. Kikuchi and H. Fujita, *AIChE*, 2002, **48**, 1639-1644.
27. K. C. van Dijke, K. Schroën and R. M. Boom, *Langmuir*, 2008, **24**, 10107-10115.
28. S. L. Anna, N. Bontoux and H. A. Stone, *Applied Physics Letters*, 2003, **82**, 364-366.
29. P. Garstecki, H. A. Stone and G. M. Whitesides, *Physical Review Letters*, 2005, **94**, 164501-164501-164501-164504.
30. S. v. d. Graaf, M. L. J. Steegmans, R. G. M. v. d. Sman, C. G. P. H. Schroën and R. M. Boom, *Colloids and Surfaces A-Physicochemical and Engineering Aspects*, 2005, **266**, 106-116.
31. A. Kubo, H. Shinmori and T. Takeuchi, *Chemistry Letters*, 2006, **35**, 588-589.
32. T. Nisisako and T. Torii, *Lab On A Chip*, 2008, **8**, 287-293.
33. T. Nisisako, T. Torii and T. Higuchi, *Lab On A Chip*, 2002, **2**, 24-26.
34. T. Thorsen, R. W. Roberts, F. H. Arnold and S. R. Quake, *Physical Review Letters*, 2001, **86**, 4163-4166.
35. A. Kawai, S. Matsumoto, H. Kiriya, T. Oikawa, K. Hara, T. Ohkawa, T. Futami, K. Katayama and K. Nishizawa, *TOSOH Research and Technology Review*, 2003, **47**, 3-9.
36. I. Kobayashi, S. Hirose, T. Katoh, Y. P. Zhang, K. Uemura and M. Nakajima, *Microsystem Technologies-Micro-and Nanosystems-Information Storage and Processing Systems*, 2008, **14**, 1349-1357.
37. S. J. Peng and R. A. Williams, *Trans IChemE*, 1998, **76**, 894-901.
38. S. Sugiura, M. Nakajima and M. Seki, *Langmuir*, 2002, **18**, 5708-5712.
39. L. Capretto, S. Mazzitelli, C. Balestra, A. Tosi and C. Nastruzzi, *Lab on a Chip*, 2008, **8**, 617-621.

Chapter 2

Generalised insights in droplet formation at T-junctions through statistical analysis

Abstract

Though much experimental work has been done on droplet formation in microfluidic T-junctions, the field is fragmented due to differences in channel dimensions, flow rates, and materials used. The same is true for models, which describe a limited range of the droplet formation spectrum, due to obvious boundary conditions. In this paper, we tried to unify the available data into a more general model using statistical analysis. This approach was chosen because of its accessibility and ease of use for unbiased analysis of available data. We found that data from various literature sources, and therefore different regimes, were described with a two-step model, which distinguishes between a droplet growth and a droplet detachment phase. The two-step model was found statistically valid over the whole range of observed droplet shapes (viz plugs, discs, or drops) and encompassed all systems and sources. Channel dimensions were found to determine droplet growth, while both continuous- and disperse-phase flow rate govern the subsequent time needed for detachment. By using a statistical approach, we were able to generalise data available on T-junctions into general rules of behaviour.

This chapter is published as: M.L.J. Steegmans, C.G.P.H. Schroën, R.M. Boom, Generalised insights in droplet formation at T-junctions through statistical analysis, Chemical Engineering Science, 2009, 64 (13), 3042-3050.

Introduction

Thorsen *et al.* [1] were the first to show emulsification at T-junctions in 2001. Ever since, the use of T-junctions has been reported for the preparation of *e.g.* double emulsions [2-4] and microspheres [5, 6], as well as in (bio)chemical analysis [7, 8]. Droplets prepared at T-junctions are typically between several up to hundreds of micrometres in size [6, 9-13] (see Table 1) and have a polydispersity index (standard deviation to average droplet size ratio) below 5 % [5], which implies acceptable monodispersity. Per T-junction, up to several thousands of droplets can be produced per second [11]. Though this production rate is quite adequate, the accompanying volume throughput is too low to meet demands for industrial-scale emulsification [5]. Therefore, T-junctions have been parallelised [5, 14, 15]. Nisisako *et al.* [5] were the first to operate 256 T-junctions simultaneously and showed that neither droplet size nor monodispersity is influenced by parallelisation, which is an important step towards actual application.

An even more important step that needs to be taken before T-junctions can be applied is control over the droplet size over a broad range of process conditions. Currently in literature, microfluidic devices from different materials with diverse microchannel dimensions (depths and widths) are reported to emulsify entirely different materials (Table 1 gives an impression of this diversity). As a result, the available data vary widely in almost every possible aspect (*e.g.* viscosities, interfacial tension, and wetting properties) and consequently cannot be compared directly. Until now, it was never attempted to bring data from different studies together to obtain the broader overview necessary to ultimately direct conditions and T-junction dimensions toward actual applications.

Table 1: Overview of in literature studied device materials, channel dimensions (near the T-junction), emulsified materials, continuous-, and disperse-phase flow rates (ϕ). For these data we assume monodisperse droplet formation. The produced droplet radii are given as the equivalent diameter of unrestricted spheres with volumes equal to the droplet volume (R_{3Ddr}). The first five entries are experimental studies and the last entry is a numerical study.

Device material	Continuous-phase channel		Disperse-phase channel		Continuous phase	ϕ_c	Disperse phase	ϕ_d	R_{3Ddr}	Reference
	width [μm]	depth [μm]	width [μm]	depth [μm]		[mL·h^{-1}]		[mL·h^{-1}]	[μm]	
PDMS	100	33	50	33	silicon oil	0.01-1	water (Milipore)	0.002-1.8	37-87	Fig. 2 & 4 [12]
borosilicate glass	303	5	24	5	ethanol-, SDS-, or Tween 20-water	0.5-0.7	hexadecane	$6\cdot10^{-4}$–$4\cdot10^{-3}$	4.5-14[a]	[9]
PMMA	500	100	100	100	high oleic sunflower oil	1-29	water (ultra pure)	0.1-1.5	52-190	Fig. 6 left [11]
(modified) PMMA	600	300	600	300	water (de-ionised)	12-956	kerosene	0.6-59	47-346	Fig. 9 [13]
quartz glass	220	30	120	30	2 wt.% PVA-water	0.9-18	1,6-hexanediol diacrylate	0.05 & 0.1	18-60[b]	Fig. 3 [6]
quartz glass	100	100	100	100	2 wt.% PVA-water	1-4	1,6-hexanediol diacrylate	0.05-0.40	24-75	[10]

[a] these droplets have a polydispersity index (standard deviation to average droplet size ratio) below 3 %.

[b] droplets with a radius between 15 and 60 μm have a polydispersity index of 1-2 % [6].

In this chapter, data from various literature sources are investigated and eventually brought together. We start very basic with a summary of various aspects mentioned for T-junctions in literature, such as the various droplet-formation regimes that are distinguished, and our interpretation on how this links to various droplet shapes. Subsequently, we present models from various literature sources that were derived to describe droplet formation at T-junctions; a part which is concluded with the more general two-step model. Next, the results of statistical analysis carried out with the various models are presented and we will show that statistical analysis is a useful tool to bring together the broad range of literature data available. Eventually, the essence of the statistically valid two-step model is used to give guidelines for the design and operation of T-junctions for emulsification purposes.

General aspects

Droplet formation at T-junctions

Description of the T-junction system

A T-junction consists of two microchannels positioned perpendicular to one another with a uniform depth around the T-junction. Continuous and disperse phase (from now on we will use this term also prior to droplet detachment) are introduced through separate channels usually perpendicular to one another [6, 7, 9, 10, 12], but occasionally head-on [13, 16].

Droplet formation and droplet-formation regimes

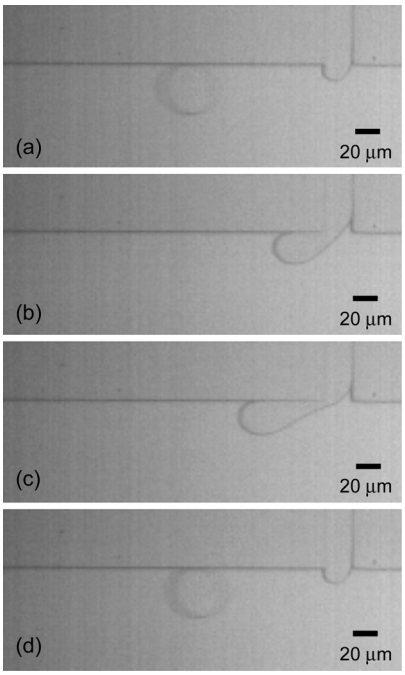

Figure 1: Droplet formation at a T-junction using water as continuous phase flowing from right to left at 0.6 mL·h^{-1} and hexadecane as disperse phase flowing from the top at 2 μL·h^{-1}. (a) The interface between water and hexadecane is hemispherical, (b) in time the hexadecane droplet gains volume and is deformed in the direction of flow, (c) the incipient droplet is only kept to the T-junction with a (thin) neck, (d) the droplet has detached, and the interface is hemispherical again. These images were obtained in borosilicate glass microdevices with a uniform depth of 5 μm, a continuous-phase channel width of 303 μm, and a disperse-phase channel width of 24 μm (for further details see van der Graaf *et al.* [9]).

In literature, three droplet-formation regimes are distinguished: squeezing, dripping, and jetting [17]. In the squeezing and the dripping regime, droplet formation starts at the opening of the disperse-phase channel (see Figure 1(a)). In time, the incipient droplet grows and is deformed by the cross-flowing continuous phase (see Figure 1(b)), until it is only attached to the bulk by a thin neck (see

Figure 1(c)). The incipient droplet detaches when the neck breaks at the downstream corner of the T-junction (see Figure 1(d)), or slightly downstream from the T-junction. The difference between squeezing and dripping is that in the squeezing regime the incipient droplet ultimately blocks the continuous-phase channel completely, while in the dripping regime continuous phase can still flow past the incipient droplet (see Figure 1). In the jetting regime, droplet formation starts downstream from the T-junction with a disperse-phase filament ('jet') near the wall and parallel to the flow direction of the continuous phase. The incipient droplet grows at the tip of this filament and detaches when the neck keeping the droplet attached to the bulk snaps-off, obviously also downstream from the T-junction.

Just before detachment, the incipient droplet is kept to the disperse-phase bulk with a filament. The smallest diameter of this filament, the neck diameter, is equal to the smallest dimension of the T-junction (usually the depth of the microchannel), and its Laplace pressure $\Delta P_{L,filament}$ is given by:

$$\Delta P_{L,filament} = \frac{2\gamma}{D_{filament,d}} + \frac{2\gamma}{D_{filament,p}} \approx \frac{2\gamma}{z} \text{ as } D_{filament,d} << D_{filament,p} \text{ (Pa)} \quad (1),$$

where γ is the interfacial tension, $D_{filament,d}$ is the diameter of the curvature of the filament in the depth of the T-junction, $D_{filament,p}$ is the diameter of the curvature of the filament in the plane perpendicular to the depth of the T-junction, and z is the (uniform) depth of the T-junction. Please note, that z can be used instead of $D_{filament,d}$ as the diameter of the filament equals the depth of the channel.

Any part of the filament becoming thinner than the depth of the T-junction will experience a higher Laplace pressure of:

$$\Delta P_{L,neck} = \frac{2\gamma}{D_{neck,d}} + \frac{2\gamma}{D_{neck,p}} \approx \frac{2\gamma}{D_{neck,d}} \text{ as } D_{neck,d} << D_{neck,p} \quad \text{(Pa)} \quad (2),$$

where γ is the interfacial tension, $D_{neck,d}$ is the diameter of the curvature of the neck in the depth of the T-junction, and $D_{neck,p}$ is the diameter of the curvature of the neck in the plane perpendicular to the depth of the T-junction. When the neck

becomes smaller than the smallest dimension of the microchannel, the neck breaks (due to the Laplace pressure difference) and a droplet detaches [9, 12].

Capillary number and process conditions

In literature, the observed droplet-formation regime is mostly linked to the capillary number of the continuous phase (Ca_c) [‡]; generally it is reported that an increase in Ca_c causes transitions from squeezing into dripping and subsequently into jetting [7, 12, 17]. However, Nisisako *et al.* [6] reported that at low continuous-phase flow rates (*i.e.* low Ca_c), parallel flow (without any droplet formation) was observed. This changed to jetting (droplet formation downstream from the T-junction) at higher flow rates. Upon further increase in the continuous-phase flow rate (*i.e.* higher Ca_c), the regime changed to dripping at the T-junction and eventually reverted to jetting (droplet formation downstream from the T-junction). The difference in the observations might be caused by the fact that the disperse-phase flow rate was fixed in this work [6].

Some authors do not distinguish between the various regimes (squeezing, dripping, and jetting) and find that droplet size decreases with increase in continuous-phase flow rate and increases with increase in disperse-phase flow rate [1, 6, 7, 9-13]. Since no abrupt changes in droplet size were observed, going from one regime to another, it seems reasonable to treat all regimes in the same way, as was applied in this research.

[‡] Capillary number of the continuous phase is defined as: $Ca = (\eta_c v_c)/\gamma$, where η_c is the dynamic viscosity of the continuous phase, v_c is the velocity of the continuous phase, and γ is the interfacial tension.

Comparison of droplet-formation regimes and droplet shapes

Three 'types of droplets' are distinguished: plugs, discs, and drops. Plugs are droplets in contact with all four channel walls [7, 14], discs are droplets in contact with two parallel channel walls, and drops are not in contact with channel walls and therefore will be spherical. Table 2 shows how this classification compares to the three droplet-formation regimes generally distinguished in literature.

Table 2: Overview of the type of droplets (plugs, discs, or drops) formed in each droplet-formation regime (squeezing, dripping, and jetting). A cross indicates that this type of droplet is formed.

	squeezing	dripping	jetting
plugs	x	x	
discs		x	x
drops		? [b]	x

[b] From the available literature it was not conclusive whether drops are formed in the dripping regime.

T-junction models

Model by Thorsen et al.

Various T-junction models are known. The first ever model reported by Thorsen *et al.* [1] assumes that a droplet detaches when the Laplace pressure equals the shear force and therefore droplet size is estimated with the following equation:

$$R_{3Ddr} \sim \frac{\gamma}{\eta_c \dot{\gamma}_{c,gap}} \quad \text{(m)} \qquad (3),$$

where R_{3Ddr} is the equivalent radius of an unrestricted spherical drop of the same volume as the droplet, γ is the interfacial tension, η_c is the dynamic viscosity of the continuous phase, and $\dot{\gamma}_{c,gap}$ is the shear rate of the continuous phase in the gap between the incipient disperse-phase droplet and the continuous-phase channel wall. Literature shows that this model systematically overestimates droplet size [1, 17] and therefore this model was not further considered.

Models by Zhao et al. and van der Graaf et al.

Zhao *et al.* [13] and van der Graaf *et al.* [10] both derived empirical models which describe drop, disc, and plug size, and therewith all droplet-formation regimes at once (see Table 2). The Zhao model is based on their own experimental data and includes the flow rates and the Weber numbers (*We*) §:

$$\frac{R_{3Ddr}}{D_{H,c}} = -0.1276 \ln\left[\frac{We_c\left(1-\left(\frac{\phi_d}{\phi_d+\phi_c}\right)\right)}{\left(We_d\left(\frac{\phi_d}{\phi_d+\phi_c}\right)\right)^{0.15}}\right] + 0.5595 \qquad (-) \qquad (4),$$

where R_{3Ddr} is the radius of an unrestricted spherical drop of the same volume as the droplet, $D_{H,c}$ is the hydraulic diameter of the continuous-phase channel, We_c is the Weber number of the continuous phase, We_d is the Weber number of the disperse phase, ϕ_d is the disperse-phase flow rate, and ϕ_c is the continuous-phase flow rate.

The van der Graaf model [10] is based on the assumption that the total droplet volume V_{dr} consists of an initial volume generated during the growth phase (in which detachment cannot yet take place) plus a volume increase during detachment ('neck' phase). According to van der Graaf *et al.* both volume contributions are functions of the capillary number of the continuous phase and the following equation was proposed:

$$V_{dr} = V_{growth,ref} Ca_{c,vdG}^{m} + t_{neck,ref}\phi_d Ca_{c,vdG}^{o} \qquad (m^3) \qquad (5),$$

where $V_{growth,ref}$ is the volume that needs to be reached in the growth phase at a capillary number ($Ca_{c,vdG}$) of one, $t_{neck,ref}$ is the time needed for detachment to be complete (*i.e.* for the neck to break) at a capillary number ($Ca_{c,vdG}$) of one, and m

§ Weber number is defined as: We = $(D_H v^2 \rho)/\gamma$, where D_H is the hydraulic diameter, v is the velocity, ρ is the density, and γ is the interfacial tension.

and *o* are exponents. The capillary number of the continuous phase $Ca_{c,vdG}$ is defined by van der Graaf *et al.* [10] as:

$$Ca_{c,vdG} = \frac{\dot{\gamma}_c \cdot z \cdot \eta_c}{2\gamma} \quad (-) \quad (6),$$

where $\dot{\gamma}_c$ is the shear rate of the continuous phase, z is the depth of the T-junction, η_c is the dynamic viscosity of the continuous phase, and γ is the interfacial tension. For T-junctions with 100 μm by 100 μm channels, van der Graaf *et al.* found that $V_{growth,ref}$ = 2.5·10^{-5} μL (assuming spherical drops $R_{growth,ref}$ = 18.1 μm), $t_{neck,ref}$ = 135 μs, and m = o = -0.75.

Model by Garstecki et al.

The last model is restricted to plugs formed in the squeezing regime. Garstecki *et al.* [12] estimate plug length by assuming that plug volume consists of a volume increase during the time needed for the plug to block the channel plus a volume increase during snap-off (which is proportional to the flow rate ratio). The following equation was proposed to estimate plug length L:

$$\frac{L}{w_c} = 1 + \frac{D_{neck}}{w_c}\left(\frac{\phi_d}{\phi_c}\right) \quad (-) \quad (7),$$

where w_c is the width of the continuous-phase channel and D_{neck} is the diameter of the neck.

Basic two-step droplet-formation model

The general notion that droplets are formed in two-stages when influenced by shear is mentioned in literature for various systems, including T-junctions [9, 18, 19]. A droplet growth and a droplet detachment ('neck') phase are distinguished. This suggests that the total droplet volume V_{dr} results from the volume a droplet needs to reach before it starts to detach ('growth' volume, V_{growth}) and a subsequent volume increase within the time needed for detachment ($t_{neck}\phi_d$). Assuming spherical drops this can be described with the following model [9, 18]:

$$R_{3Ddr} = \left(R_{growth}^3 + \frac{3}{4\pi} t_{neck} \phi_d \right)^{1/3} \quad \text{(m)} \quad (8),$$

where R_{3Ddr} is the equivalent radius of an unrestricted spherical drop of the same volume as the droplet, R_{growth} is the radius that needs to be reached in the growth phase (after which detachment starts), and t_{neck} is the time needed for detachment (*i.e.* for the neck to break). Please note that when droplets detach very fast, R_{growth} approaches R_{3Ddr} (see Equation 8). This occurs *e.g.* at flat microfluidic Y-junctions [20].

For the initial growth phase, it is suggested that R_{growth} can be derived from a force balance between the forces exerted on the incipient droplet. The main force keeping the droplet attached to the disperse-phase bulk is proportional to the interfacial tension. This force is balanced by the shear force exerted by the continuous phase and therefore droplets start to detach when the shear force exceeds the interfacial tension force [18]. Please note that for plugs in the squeezing regime, the effect of the shear force is surpassed by the force arising from the pressure drop over the incipient plug blocking the channel and therefore detachment starts when this latter force exceeds the interfacial tension force [12].

Method

Data collection

Quantitative droplet size data from microfluidic T-junctions with rectangular channels with a hydraulic channel diameter below 1000 μm and at conditions with Ca_c values between $3 \cdot 10^{-4}$ and 0.2 were obtained from literature (Table 1 lists the used sources). Due to the small channel sizes, *i.e.* low Reynolds numbers, flow can be assumed laminar for all data sets. In addition, for all data we assumed monodisperse droplet formation and ideal wetting conditions of the continuous phase. The latter seems reasonable as van der Graaf et al. [10] showed that the contact angle hardly affected droplet size. Please note that for the data (and model) by Zhao et al. [13] continuous and disperse phase were introduced head on, in

contrast to the other data; they were evaluated to see whether there is a systematic difference between these two ways of operation.

To compare the literature data, the equivalent diameter or radius of an unrestricted spherical drop of the same volume (D_{3Ddr} or R_{3Ddr}) is used. We read R_{3Ddr} directly from the figures in these sources or calculated R_{3Ddr} from the droplet volume assuming the droplets to be spheres. For Garstecki's data [12], R_{3Ddr} was calculated from the plug length, assuming plugs enclosed between channel walls to be flat ellipses, so that R_{3Ddr} followed from:

$$R_{3Ddr} = \left(\frac{\left(\pi \frac{L}{2} \frac{w_c}{2} z \right)}{\frac{4}{3}\pi} \right)^{\frac{1}{3}} = 0.572 (w_c L z)^{\frac{1}{3}} \quad \text{(m)} \qquad (9).$$

Statistical analysis

Statistical analysis is used to evaluate whether models are useful to describe droplet size data other than those the model was originally derived for, *i.e.* from different literature sources. Parity plots were used in which the predicted droplet size was calculated and plotted as function of the (experimental) droplet size. The match between model and (experimental) data follows from the scatter of data around the line of parity. The closer the data are to the line of parity, and the more even their distribution, the better model and data correspond. The dashed line in the plots indicates the line of parity while the dotted-dashed lines mark 30 % deviation of the experimental droplet size. Please note that we just compare the models to other data to find out whether they are useful to apply more generally; we do not intend to suggest that the original models are incorrect.

The two-step model (Equation 8) was fitted to the literature data assuming a linear relation between droplet volume and disperse-phase flow rate. Since the two-step model contains two parameters (R_{growth} and t_{neck}), at least three data points were needed to calculate these parameters with any statistical significance (to estimate

the standard deviations of the parameters, the number of data points n has to exceed the number of parameters p; see further). Therefore, only literature data with at least three (but preferably many more) disperse-phase flow rates at constant continuous-phase flow rate were considered for further analysis. In addition, the continuous-phase viscosity, disperse-phase viscosity, device dimensions, droplet shape, and interfacial tension should be constant, but mostly this was the case. From Table 1 only data by Nisisako *et al.* [6] did not meet these criteria.

The two-step model was fitted to the selected data by adapting R_{growth} and t_{neck} using the least squares method; which uses the minimal sum of squares (sum of squares is a measure for the spread of data around a fitted model). The minimal sum of squares [**] and accompanying parameters (R_{growth} and t_{neck}) were found with the Levenberg-Marquardt method in Mathcad 13. The standard deviations of parameters R_{growth} and t_{neck} were estimated as the product of the square root of the residual mean square [††] and the square root of the variance of the parameter. For the fits, the radius was used (see Equation 8); if the volume was used the largest droplet would completely dominate the fit.

Parity plots were used to evaluate the performance of the two-step model (see previously). In addition, a fit was regarded unsuitable when the values of R_{growth} or t_{neck} assumed physically impossible values (*e.g.* negative values) or when their 95 % confidence interval (estimated parameter plus or minus 1.96 times the standard deviation) included zero. In that case, the respective parameter is superfluous.

[**] Sum of squares SS is defined as: $SS = \sum_i \left(Y_i - \hat{Y}_i\right)^2$, where Y_i is the (experimental) droplet size, and $\hat{Y}_i$ is the droplet size predicted by the two-step model.

[††] Residual mean square MSE is defined as: $MSE = SS/(n\text{-}p)$, where SS is the sum of squares, n is the number of data points, and p is the number of parameters in the model (p is two for the two-step model from Equation 8).

Results and discussion

T-junction models

In first instance, we check whether models specific to T-junctions (see section 'T-junction models') are comprehensive enough to describe droplet size data from different literature sources with comparable Ca_c values. Parity plots were used to get a first impression of the usefulness of the models. The dashed line indicates the line of parity, and ideally, the points are close to this line and evenly distributed. The dotted-dashed lines mark 30 % deviation of the (experimental) droplet size.

Models by Zhao et al. and Garstecki et al.

Parity plots of the models by Zhao *et al.* (Equation 4) [13] and by Garstecki *et al.* (Equation 7) [12] are shown in Figure 2. When the predicted droplet sizes were compared to the data for which the models were initially derived, the match was satisfactory. However, when the models were compared to data from other literature sources, neither the model from Zhao *et al.* [13], nor the model from Garstecki *et al.* [12] were adequate to bring the various data together, in spite of being appropriate for the data points for which they were derived. Please note that by no means we tend to suggest that therefore these models are incorrect.

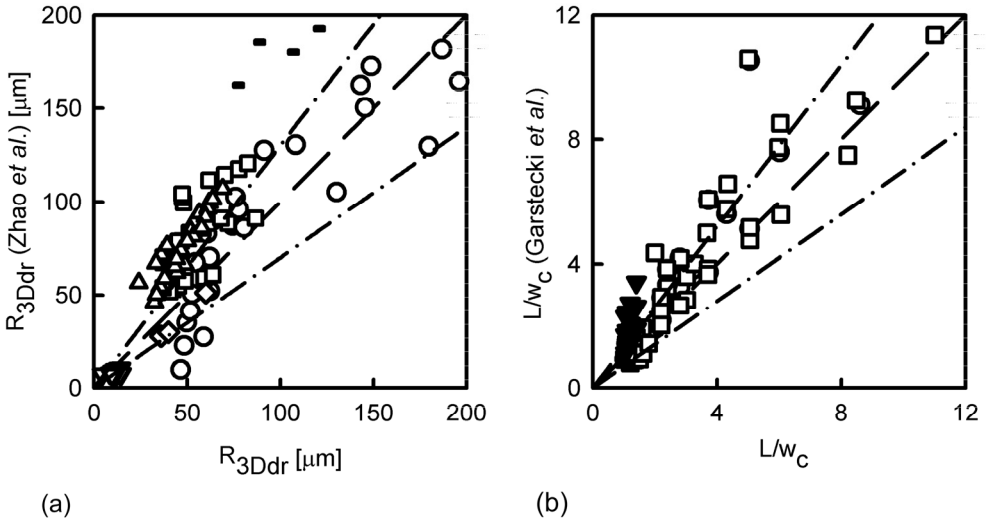

Figure 2: (a) Parity plot of the droplet size generated with the model by Zhao *et al.* [13] (Equation 4) (R_{3Ddr}(*Zhao et al.*)) as function of the (experimental) droplet size from various literature sources (R_{3Ddr}). Droplet size is described with the equivalent radius of an unrestricted spherical drop with the same volume. Literature data with Ca_c values comparable to the ones the model was validated with, *i.e.* Ca_c between $4{\cdot}10^{-4}$ and $4{\cdot}10^{-2}$, were from: Zhao *et al.* [13] (O), Garstecki *et al.* [12] (□), van der Graaf *et al.*, 2006 [10] (△), van der Graaf *et al.*, 2005 [9] (▽), Nisisako *et al.*, 2002 [11] (-), and Nisisako *et al.*, 2004 [6] (◊). (b) Parity plot of the plug length-to-continuous-phase-channel-width ratio generated with the model by Garstecki *et al.* [12] (Equation 7) (L/w_c (*Garstecki et al*)) as function of the L/w_c values for plug data from data with Ca_c values comparable to the ones the model was validated with, *i.e.* Ca_c between $4{\cdot}10^{-4}$ and 0.2, from: Garstecki *et al.* fig.2 (O) and fig. 4 (□) [12], and van der Graaf *et al.*, 2006 [10] (▼). The dashed line indicates the line of parity, while the dotted-dashed lines mark 30 % deviation of the experimental droplet size.

Model by van der Graaf et al.

Figure 3 shows that the van der Graaf model (Equation 5) [10] describes the data for which it was derived well, but does not describe all data from other literature sources. Most probably, the parameters that were derived for the original set of data are only valid for T-junctions with 100 μm by 100 μm channels.

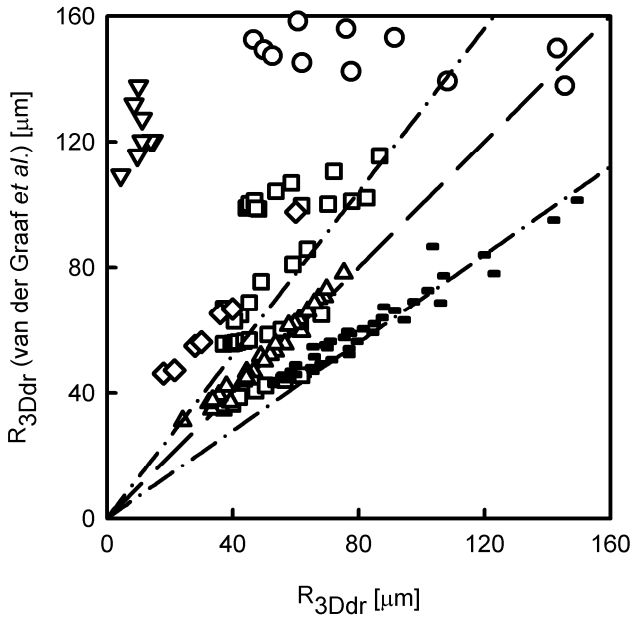

Figure 3: Parity plot of the droplet size generated with the empirical model by van der Graaf *et al.* [10] (Equation 5) (R_{3Ddr}(*van der Graaf et al.*); assuming $V_{growth,ref}$ = 2.5·10^{-5} μL, $t_{neck,ref}$ = 135 μs, and m = n = -0.75) as function of the (experimental) droplet size from various literature sources (R_{3Ddr}). Droplet size is described with the equivalent radius of an unrestricted spherical drop with the same volume. Literature data with Ca_c values comparable to the ones the model was validated for, *i.e.* Ca_c between 4·10^{-3} and 0.1, were from: Zhao *et al.* [13] (O), Garstecki *et al.* [12] (□), van der Graaf *et al.*, 2006 [10] (△), van der Graaf *et al.*, 2005 [9] (▽), Nisisako *et al.*, 2002 [11] (-), and Nisisako *et al.*, 2004 [6] (◊). The dashed line indicates the line of parity, while the dotted-dashed lines mark 30 % deviation of the experimental droplet size.

In summary, the primary statistical analysis has shown that none of the models is general enough to describe both the original data and data from other literature sources. Therefore, in the next section the more general two-step droplet-formation model (see section 'Basic two-step droplet-formation model') is fitted to the data.

Basic two-step droplet-formation model

Primary analysis

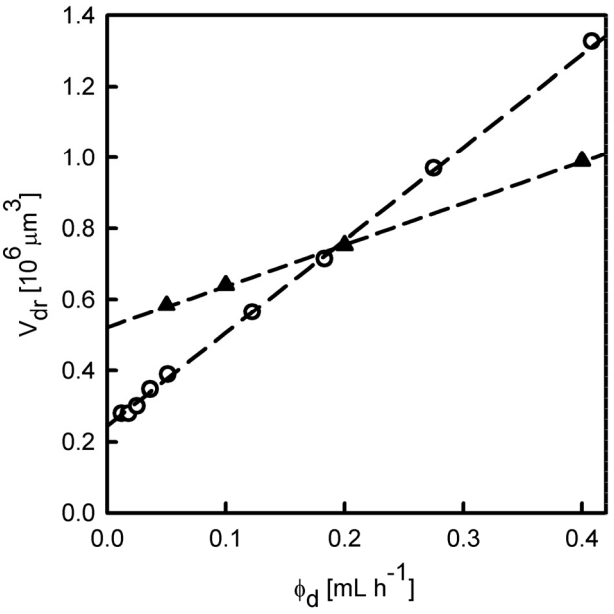

Figure 4: Droplet volume V_{dr} as function of disperse-phase flow rate ϕ_d for plug data from van der Graaf *et al.* [10] with continuous-phase flow rate 1 mL·h^{-1}, dynamic viscosity of the continuous phase 1.95 mPa·s, and interfacial tension 5 mN·m^{-1} (▲) and plug data from Garstecki *et al.* [12] with continuous-phase flow rate 0.1 mL·h^{-1}, dynamic viscosity of the continuous phase 100 mPa·s, and interfacial tension 36.5 mN·m^{-1} (O). The dashed lines are the fits obtained with the two-step model (Equation 8), for parameter values R_{growth} 49.9 µm and t_{neck} 4.2 ms for van der Graaf *et al.* and R_{growth} 38.8 µm and t_{neck} 9.4 ms for Garstecki *et al.*. The intercepts of these lines are equal to V_{growth} and the slopes are equal to t_{neck}.

An example of the results of the basic two-step model is shown in Figure 4, and it shows that the two-step model fits the data well. Not only these data, but data from all other literature sources could be described and significant R_{growth} and t_{neck} values were obtained (see Appendix A for all data). These results strongly suggest that droplet formation at T-junctions occurs in two steps, and that there is no

direct relation with the droplet shape, the way the phases are introduced to the T-junction, or the device material (see Figure 5 and 6, Appendix A, and Table 1). As data from all literature sources are successfully described, parameters R_{growth} and t_{neck} are now used to relate the various data.

Parameter analysis

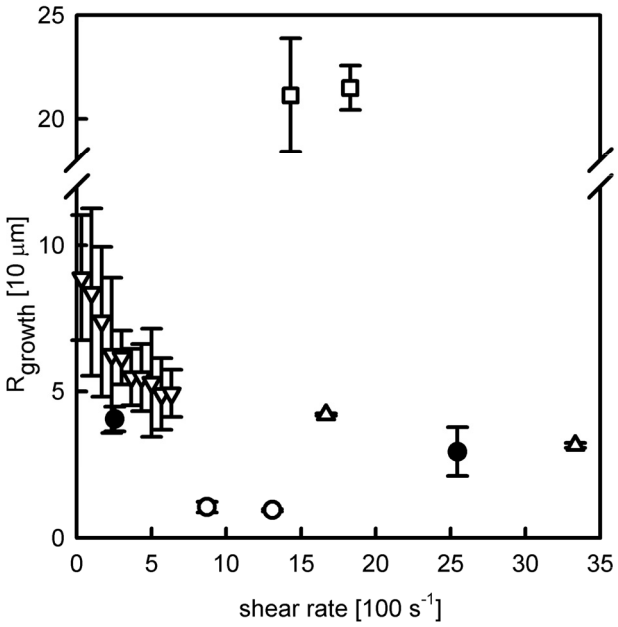

Figure 5: Fitted R_{growth} values as function of continuous-phase shear rate for: disc data from Zhao *et al.* [13] (η_c = 1 mPa·s, η_d = 1.2 mPa·s, and γ = 45 mN·m^{-1}) (□), plug data from Garstecki *et al.* [12] (η_c = 10 mPa·s, η_d = 1 mPa·s, and γ = 36.5 mN·m^{-1}) (•), drop data from van der Graaf *et al.*, 2006 [10] (η_c = 1.95 mPa·s, η_d = 6.7 mPa·s, and γ = 5 mN·m^{-1}) (△), disc data from van der Graaf *et al.*, 2005 [9] (η_c = 1 mPa·s, η_d = 3.3 mPa·s, and γ = 44 mN·m^{-1}) (O), and disc data from Nisisako *et al.*, 2002 [11] (η_c = 33 mPa·s, η_d = 1 mPa·s, and γ = 26.6 mN·m^{-1}) (▽). The error bars represent the 95 % confidence intervals.

The 95 % confidence intervals in Figure 5 and the following Figures are quite large, due to the limited amount of quantitative data available in literature, but the values still show a general direction. Figure 5 shows that the 95 % confidence intervals of almost all R_{growth} values for experimental studies overlap within one set of data and therefore statistically, R_{growth} is independent of the continuous-phase shear rate ‡‡. Only for the lowest continuous-phase shear rate used by Nisisako *et al.* [11] this is not the case.

Interestingly, for the numerical (simulated) drop data by van der Graaf *et al.* [10] a significant decrease in R_{growth} with increase in continuous-phase shear rate is observed. It is also obvious, that for the numerical data the confidence intervals are much smaller, therewith allowing this distinction. Whether this effect is real can only be checked if more experimental data points become available.

Zhao *et al.* [13] and van der Graaf *et al.* [9] emulsified materials with comparable properties (interfacial tension and continuous-phase viscosity). For the data from van der Graaf *et al.* a lower R_{growth} value was found (see Figure 5). As Zhao *et al.* used larger continuous-phase channels than van der Graaf *et al.* (see Table 1); it is only logical that R_{growth} increases with increase in continuous-phase channel size.

R_{growth} depends not only on channel dimensions, but also on droplet shape as could be derived from data of Garstecki *et al.* [12]. Table 3 shows that plugs have a larger R_{growth} than discs at further equal process conditions and material properties. As t_{neck} is equal, plugs will have both a larger growth volume and final droplet volume than discs (see Equation 8). Assuming that the growth volume can be described with a force balance [18], the difference in R_{growth} might be caused by a difference in the force needed to overcome the retaining force and therewith induce detachment (see section 'Basic two-step droplet-formation model').

‡‡ The continuous phase shear rate is defined as: $\dot{\gamma} = 3v_c/w_c$, where v_c is the velocity of the continuous phase and w_c is the width of the continuous-phase channel.

Table 3: Parameters R_{growth} and t_{neck} fitted with the basic two-step model (Equation 8) shown with their 95 % confidence intervals for discs and plugs. The data are for fits at constant continuous-phase flow rate (ϕ_c = 0.1 mL·h^{-1}), dynamic viscosity of the continuous phase (η_c = 100 mPa·s) and disperse phase (η_d = 1 mPa·s), chip dimensions (see Table 1), and interfacial tension (γ = 36.5 mN·m^{-1}) using n data points. The data source is given in the last column.

Droplet shape	R_{growth} [μm]	t_{neck} [ms]	n	Data source
Discs	36.1 ± 0.2	9.7 ± 0.2	4	[12]
Plugs	38.8 ± 0.4	9.4 ± 0.4	9	[12]

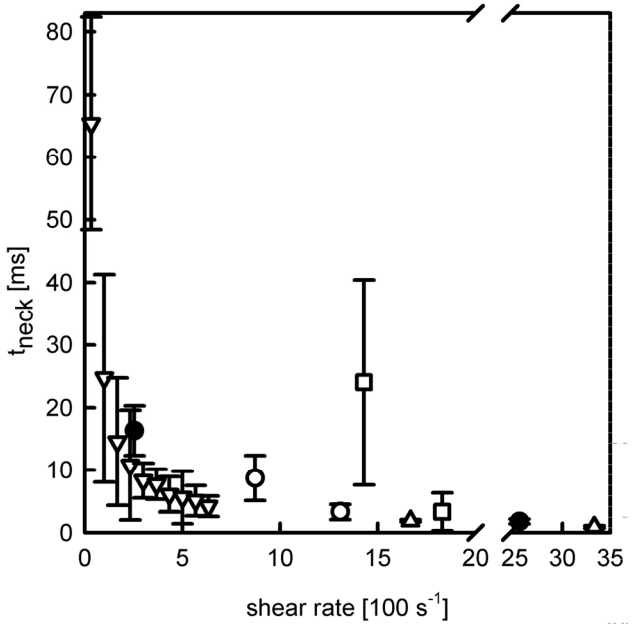

Figure 6: Fitted t_{neck} values as function of continuous-phase shear rate for disc data from Zhao *et al.* [13] (η_c = 1 mPa·s, η_d = 1.2 mPa·s, and γ = 45 mN·m^{-1}) (□), plug data from Garstecki *et al.* [12] (η_c = 10 mPa·s, η_d = 1 mPa·s, and γ = 36.5 mN·m^{-1}) (•), drop data from van der Graaf *et al.*, 2006 [10] (η_c = 1.95 mPa·s, η_d = 6.7 mPa·s, and γ = 5 mN·m^{-1}) (△), disc data from van der Graaf *et al.*, 2005 [9] (η_c = 1 mPa·s, η_d = 3.3 mPa·s, and γ = 44 mN·m^{-1}) (O), and disc data from Nisisako *et al.*, 2002 [11] (η_c = 33 mPa·s, η_d = 1 mPa·s, and γ = 26.6 mN·m^{-1}) (▽). The error bars represent the 95 % confidence intervals.

Figure 6 shows that t_{neck} decreases significantly in some cases with increase in continuous-phase shear rate, in contrast to R_{growth}. This decrease might result from the fact that the evolving neck elongates faster at increasing shear rate and thus breaks faster. At constant disperse-phase flow rate and further constant conditions, these results suggest that the second phase of droplet formation is shorter at increasing continuous-phase shear rate. Since the first stage renders a constant volume, the total volume of the droplet will also decrease with increase in continuous-phase flow rate, which is in agreement with observations in various literatures [6, 9, 12].

Interfacial properties

Besides process related effects on the R_{growth} and the t_{neck}, also effects derived from the used materials can be discerned. As an example, the effect of interfacial tension is discussed here, based on the numerical (simulation) work by van der Graaf *et al.* [10].

Figure 7 shows that R_{growth} increases with increase in interfacial tension while t_{neck} increases only initially (*i.e.* the 95 % confidence intervals start to overlap). The effects on R_{growth} can be qualitatively understood assuming that the main force keeping the droplet attached is proportional to the interfacial tension [18] (see section 'Basic two-step droplet-formation model'). The higher the interfacial tension value, the higher the retaining force, the less fast it is exceeded, and the larger the droplets. The effect on t_{neck} may arise from the fact that an interface resists expansion to a greater degree with increase in interfacial tension; thus, at constant continuous-phase flow rate, t_{neck} is longer.

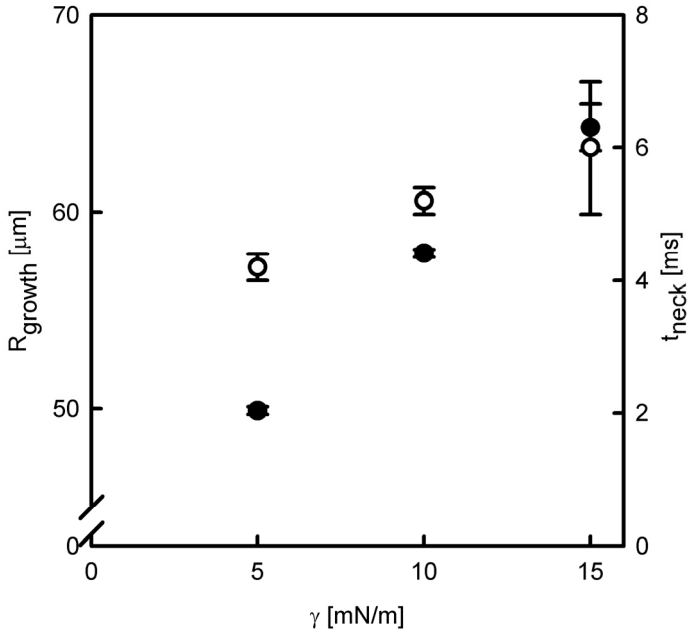

Figure 7: Fitted R_{growth} (filled symbols) and t_{neck} (open symbols) values as function of the interfacial tension γ for disc data from van der Graaf *et al.*, 2006 [10] (η_c = 1.95 mPa·s and η_d = 6.7 mPa·s). The error bars represent the 95 % confidence interval.

Our results show that in order to control droplet size at T-junctions channel dimensions need to be customised, and the continuous- and disperse-phase flow rate need to be precisely controlled. However, the large 95 % confidence intervals and limited amount of data are of influence on our conclusions. Therefore, to maximize the potential of statistical analysis and verify the observed trends, additional systematic quantitative T-junction data are of essence.

Conclusion

T-junction data which differ in many aspects, like flow conditions and channel dimensions, were related via a two-step model consisting of a growth phase and a detachment phase. The model is statistically relevant for the description of droplet size data from widely different literature sources and it covers different droplet

shapes and device materials. Our results suggest that droplet size at T-junctions can be controlled by either controlling growth volume through channel dimensions or detachment time through continuous- and disperse-phase flow rate.

By finding similarities between T-junction data, which seem scattered, more information essential for process design can be generated. Besides, it helps to formulate guidelines to control droplet size. Therefore, we feel that the type of statistical analysis that is performed here, which is fast, relatively straightforward and assessable, has considerable benefit over less available options such as *e.g.* CFD simulations.

Acknowledgement

The authors wish to thank MicroNed for supporting this research.

Appendix

Table A: parameters R_{growth} and t_{neck} fitted with the two-step droplet-formation model (Equation 8) shown with their 95 % confidence intervals. The fits are for data at constant continuous-phase shear rate $\dot{\gamma}_c$, constant dynamic viscosity of the continuous phase η_c, and constant interfacial tension γ using n data points for plugs, discs, or drops. R_{3Ddr} is the droplet radius calculated with Equation 8 using fitted R_{growth} and t_{neck}, $R_{3D,exp}$ is the droplet radius obtained from literature. The data source is given in the last column.

$\dot{\gamma}_c$	η_c	γ	R_{growth}	t_{neck}	n	Shape	R_{3Ddr} range		$R_{3D,exp}$ range		Data source
[100s^{-1}]	[mPa·s]	[mN·m^{-1}]	[µm]	[ms]	[-]		[µm]		[µm]		
537	1	44	10.4 ± 1.8	8.7 ± 3.6	4	Disc	12.5	14.4	12.6	14.4	[9]
805	1	44	9.4 ± 0.4	3.3 ± 1.2	3	Disc	10.2	11.0	10.1	11.0	[9]
17	1.95	1	31.7 ± 1.6	2.2 ± 0.6	3	Drop	34.0	39.4	33.3	39.3	[10]
17	1.95	5	49.9 ± 0.2	4.2 ± 0.2	4	Plug	51.7	61.8	51.8	61.8	[10]
17	1.95	10	57.9 ± 2.2	5.2 ± 0.2	4	Plug	59.6	69.2	59.7	69.0	[10]
17	1.95	15	64.3 ± 1.2	6.0 ± 1.0	4	Plug	65.9	75.2	66.0	75.2	[10]
33	1.95	5	42.1 ± 0.4	1.9 ± 0.2	4	Drop	43.3	50.0	46.6	50.0	[10]
67	1.95	5	31.6 ± 0.8	0.9 ± 0.2	4	Drop	32.6	38.1	32.5	38.0	[10]
2	33	26.6	88.8 ± 21.4	65.4 ± 17	3	Disc	104.3	193.1	102.0	190.0	[11]
6	33	26.6	83.8 ± 38.6	24.7 ± 16.6	3	Disc	90.9	144.9	86.5	140.5	[11]
10	33	26.6	73.8 ± 25.6	14.5 ± 10.2	3	Disc	79.3	122.6	75.0	118.5	[11]
14	33	26.6	62.4 ± 25.6	10.8 ± 8.8	3	Disc	68.0	109.6	64.0	105.5	[11]

(Table A continued)

$\dot{\gamma}_c$ [100s^{-1}]	η_c [mPa·s]	γ [mN·m^{-1}]	R_{growth} [μm]	t_{neck} [ms]	n [-]	Shape	R_{3Ddr} range [μm]		$R_{3D,exp}$ range [μm]		Data source
18	33	26.6	61.5 ± 9.2	8.3 ± 2.8	3	Disc	66.0	101.9	64.5	100.5	[11]
22	33	26.6	54.8 ± 9.6	7.7 ± 2.4	3	Disc	60.0	97.6	58.5	96.0	[11]
26	33	26.6	54.7 ± 11.4	6.1 ± 2.8	3	Disc	58.9	91.7	57.0	90.0	[11]
30	33	26.6	52.9 ± 18.4	5.6 ± 4.2	3	Disc	57.0	89.0	54.0	86.0	[11]
34	33	26.6	49.1 ± 12.2	5.1 ± 2.4	3	Disc	53.4	85.5	51.5	83.5	[11]
38	33	26.6	49.3 ± 8.0	4.2 ± 1.6	3	Disc	52.9	81.3	51.5	80.0	[11]
1	100	36.5	43.9 ± 3.6	106.6 ± 16.8	7	Plug	46.2	85.7	48.2	82.6	[12]
10	10	36.5	40.6 ± 4.2	16.3 ± 4.0	10	Plug	42.3	79.8	44.4	86.7	[12]
10	100	36.5	36.3 ± 0.2	9.7 ± 0.2	4	Disc	36.6	37.6	37.1	39.6	[12]
10	100	36.5	38.8 ± 0.4	9.4 ± 0.4	9	Plug	40.4	67.9	40.6	68.2	[12]
103	10	36.5	29.4 ± 8.4	1.8 ± 0.4	6	Plug	39.5	62.3	40.6	63.7	[12]
21	1	45	211.4 ± 27.4	24.0 ± 16.4	3	Disc	236.3	257.3	237.7	258.5	[13]
27	1	45	215.0 ± 11.6	3.3 ± 3.0	3	Disc	219.6	232.3	217.6	231.3	[13]

References

1. T. Thorsen, R. W. Roberts, F. H. Arnold and S. R. Quake, *Physical Review Letters*, 2001, **86**, 4163-4166.
2. S. Okushima, T. Nisisako, T. Torii and T. Higuchi, *Langmuir*, 2004, **20**, 9905-9908.
3. T. Nisisako, S. Okushima and T. Torii, *Soft Matter*, 2005, **1**, 23-27.
4. V. Barbier, M. Tatoulian, H. Li, F. Arefi-Khonsari, A. Ajdari and P. Tabeling, *Langmuir*, 2006, **22**, 5230-5232.
5. T. Nisisako and T. Torii, *Lab On A Chip*, 2008, **8**, 287-293.
6. T. Nisisako, T. Torii and T. Higuchi, *Chemical Engineering Journal*, 2004, **101**, 23-29.
7. J. D. Tice, A. D. Lyon and R. F. Ismagilov, *Analytica Chimica Acta*, 2004, **507**, 73-77.
8. B. Zheng and R. F. Ismagilov, *Angewandte Chemie-International Edition*, 2005, **44**, 2520-2523.
9. S. v. d. Graaf, M. L. J. Steegmans, R. G. M. v. d. Sman, C. G. P. H. Schroën and R. M. Boom, *Colloids and Surfaces A-Physicochemical and Engineering Aspects*, 2005, **266**, 106-116.
10. S. v. d. Graaf, T. Nisisako, C. G. P. H. Schroën, R. G. M. v. d. Sman and R. M. Boom, *Langmuir*, 2006, **22**, 4144-4152.
11. T. Nisisako, T. Torii and T. Higuchi, *Lab On A Chip*, 2002, **2**, 24-26.
12. P. Garstecki, M. J. Fuerstman, H. A. Stone and G. M. Whitesides, *Lab On A Chip*, 2006, **6**, 437-446.
13. Y. Zhao, G. Chen and Q. Yuan, *AIChE Journal*, 2006, **52**, 4052-4060.
14. B. Zheng, J. D. Tice and R. F. Ismagilov, *Analytical Chemistry*, 2004, **76**, 4977-4982.
15. V. Barbier, H. Willaime, P. Tabeling and F. Jousse, *Physical Review E*, 2006, **74**.
16. P. Guillot and A. Colin, *Physical Review E*, 2005, **72**.
17. M. De Menech, P. Garstecki, F. Jousse and H. A. Stone, *Journal of Fluid Mechanics*, 2008, **595**, 141-161.

18. S. J. Peng and R. A. Williams, *Trans IChemE*, 1998, **76**, 894-901.

19. S. v. d. Graaf, C. G. P. H. Schroën, R. G. M. v. d. Sman and R. M. Boom, *Journal of Colloid and Interface Science*, 2004, **277**, 456-463.

20. M. L. J. Steegmans, C. G. P. H. Schroën and R. M. Boom, *Langmuir*, 2009, **25**, 3396-3401.

Chapter 3

Characterisation of emulsification at flat microchannel Y-junctions

Abstract

Y-junctions with a large width-to-depth ratio were used for the emulsification of hexadecane in various ethanol-water mixtures with different static interfacial tension and viscosity. The resulting droplets were monodisperse. To describe droplet size a force-balance model was derived and was found to apply well. The model shows that the droplet size scales with the channel depth, and with the square root of the inverse capillary number ($Ca^{-1/2}$) based on the continuous phase. The disperse-phase flow rate was found not to be of influence.

This chapter is based on: Maartje L.J. Steegmans, Karin G.P.H. Schroën, Remko M. Boom, Characterization of Emulsification at Flat Microchannel Y junctions, Langmuir, 2009, 25 (6), 3396-3401.

Introduction

Microfluidic devices are a promising tool for controlled emulsification, *i.e.* the production of immiscible droplets of one phase in a continuous second phase. In contrast to other emulsification techniques such as high-pressure homogenisers, colloid mills, or membranes, in principle, droplet size and monodispersity can be controlled in microfluidic devices. The emulsification mechanism in microfluidic devices is, amongst others, determined by the geometric design. Regularly studied microfluidic geometries are, for example, microchannels using a so-called terrace-system, Ψ-junctions, and T-junctions. In microfluidic devices with a terrace, droplets detach when the disperse phase changes from a flat to a spherical shape due to interfacial tension effects, while the disperse phase drops off a shallow terrace into a deep well [1, 2]. At Ψ-junctions, droplets snap off when the nascent droplets are elongated by the surrounding continuous phase, which is known as flow-focusing or extensional flow [3, 4]. At T-junctions, the shear force of the cross-flowing continuous phase snaps off the disperse-phase droplets [5-7].

For high-throughput applications, shear-driven microfluidic devices are interesting because of their relatively simple design and the fact that in principle many can be used in parallel [8]. One of the most extensively studied shear-driven microfluidic geometries is the T-junction [5, 7, 9, 10]. Droplets produced with T-junctions are usually several to hundreds of micrometers in size with a polydispersity index (standard deviation to average droplet size ratio) of less than 5 % [8]. Typical applications include the production of microspheres [6] or double emulsions [11, 12].

A related geometry is the Y-junction. Kawai *et al.* [13] and Kubo *et al.* [14] applied Y-junctions for the production of microspheres of approximately 100 μm. Besides, Kawai *et al.* [13] mass-parallelised the Y-junction and operated up to 1500 Y-junctions simultaneously. In spite of this, neither the droplet-formation process, nor droplet-size-determining parameters are described in detail in the literature for Y-junctions. Therefore, in this article, we studied the effect of the droplet-formation mechanism, the process (*i.e.* continuous- and disperse-phase velocity), the material

(*i.e.* continuous-phase viscosity), and the interface properties (*i.e.* (static) interfacial tension) to derive a general model predicting droplet size at flat Y-junctions.

Experimental

Materials

Milli-Q water, 9, 19, 28, 38, 47, or 66 wt.% ethanol-water mixtures were used as the continuous phase. The ethanol-water mixtures were prepared from Milli-Q water and 96 %v/v ethanol (no. 20824, VWR BDH Prolabo, Amsterdam, The Netherlands). Anhydrous n-hexadecane with purity >99 % (no. 296317, Sigma-Aldrich, Steinheim, Germany) was used as the oil or disperse phase.

Viscosity

The viscosity of the various phases was obtained from the literature (see Table 1) and some values were experimentally verified at a controlled temperature of 23 °C. Viscosity was measured in duplicate with a Ubbelohde viscosimeter (OC 7373 or OC 7378, Poulten Self-e & Lee Ltd., Burnham on Crouch, U.K.), which was calibrated with Milli-Q water. The measured viscosities, 1.4 mPa·s for 9 wt.% ethanol-water and 2.7 mPa·s for 47 wt.% ethanol-water, were in agreement with the literature data (see Table 1). Therefore, the other literature data were also assumed to be reliable.

Static interfacial tension

The static interfacial tension at the hexadecane/ethanol-water interfaces was measured as function of time using a dynamic drop tensiometer (ADT, ITCONCEPT, Longessaigne, France) [15] (see Table 1). A 10 or 7 μL (the latter for 47 and 66 wt.% ethanol-water) hexadecane droplet was formed at the tip of a U-shaped needle positioned in a cuvette with the continuous phase. The measurement started from 1 to 2 s after droplet formation and took 1200 s. The interfacial tension was determined by droplet shape analysis as described by Benjamins *et al.* [15]. Each

measurement was performed in duplicate at a controlled temperature of 23 °C. The samples were measured in order of increasing concentration, and after each concentration, the cuvette and the needle were rinsed extensively with Milli-Q water.

Table 1: Viscosity η and static interfacial tension with hexadecane $\gamma_{hexadecane}$ of Milli-Q water, various ethanol-water phases, and hexadecane at temperature T.

sample	T [°C]	η [mPa·s]	$\gamma_{hexadecane}$ [mN·m^{-1}]
Milli-Q water	23	0.9 [16, 17]	41.0
9 wt.% ethanol-water	23	1.4 [17,a]	26.8
19 wt.% ethanol-water	23	1.9 [17]	19.8
28 wt.% ethanol-water	23	2.4 [17]	14.6
38 wt.% ethanol-water	23	2.5 [17]	11.6
47 wt.% ethanol-water	23	2.6 [17,a]	9.6
66 wt.% ethanol-water	23	2.2 [17]	6.9
hexadecane	20	3.34 [16]	-

[a] Experimentally verified viscosities.

Experimental setup

Microfluidic Y-junction device

We designed borosilicate glass microfluidic devices with Y-junctions, subsequently produced by Micronit Microfluidics BV (Enschede, The Netherlands). The microfluidic device consists of a lower plate in which the Y-channels are (chemically) etched and annealed to a top plate with inlets. After enclosure, the microchannels and collecting area have a uniform depth of 5 μm, which implies that the channels are flat (much wider than deep). The angle between the channels for the continuous and disperse phases was 97°, and the distance between the Y-junction and the collecting area was 0.46 mm (see Figure 1). The width of the channels varied slightly from device to device (see Table 2).

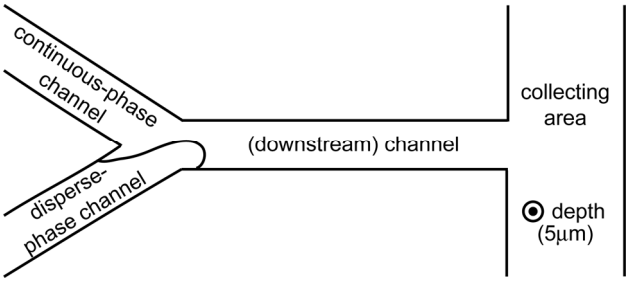

Figure 1: Outline of the Y-junction, which empties into the collecting area. The dimensions and angle are not to scale.

Table 2: Width of the continuous-phase w_c, disperse-phase w_d, and downstream channel $w_{channel}$ for the three studied microfluidic Y-junction devices. The values represent the 95 % confidence interval (average ± 1.96·standard deviation).

device	w_c [µm]	w_d [µm]	$w_{channel}$ [µm]
1	22.8 ± 0.4	23.2 ± 0.2	22.6 ± 0.4
2	22.7 ± 0.4	22.7 ± 0.4	22.6 ± 0.2
3	23.5 ± 0.2	23.7 ± 0.2	23.7 ± 0.4

Droplet-formation experiments

The Y-junction device was operated in the appropriate holder (no. 4515, Micronit Microfluidics BV, Enschede, The Netherlands). The continuous and disperse phases entered the device via two separate fused silica capillaries of approximately 13 cm length with an inner diameter of 150 µm (Polymicro Technologies, Phoenix, USA). Each fused silica capillary was connected to a 2.5 or 8 mL stainless steel Swagelock syringe using a 1/16" Swagelock connector (Alltech, Breda, The Netherlands), 9 cm PEEK tubing with an inner diameter of 1.6 mm (Alltech, Breda, the Netherlands), and a PEEK union assemblage with a capillary sleeve (Upchurch Scientific, Oak Harbor, USA).

The flow rate of the continuous and disperse phases was controlled with syringe pumps (PHD4400 (continuous phases) and PHD22/2000 (disperse phase), Harvard Apparatus, Holliston, USA). At applied continuous-phase flow rates ranging from

0.15 to 0.35 mL·h^{-1} and applied disperse-phase flow rates ranging from 3.0·10^{-4} to 1.2·10^{-3} mL·h^{-1} droplets were formed at the Y-junction. After changing the flow rate(s), droplet formation was allowed to equilibrate for at least 2 min to ensure steady state.

Droplet formation was recorded using a high-speed camera (MotionPro HS-4, Redlake, Tallahassee, USA) connected to an inverted transmitted light microscope (Axiovert 200, Carl Zeiss, Sliedrecht, The Netherlands). The formation of 25 subsequent droplets was recorded using (approximately) 20 frames per droplet, which corresponds to frame rates between 5000 and 94500 s^{-1}. Gain and exposure time were chosen such that the image quality was optimal. Besides, an "average" image was saved to confirm that the mechanisms had similar characteristics: it was found that during droplet formation, the continuous phase penetrated the disperse-phase channel. The penetration depth near the wall was found to be constant, but the angle of the contact line changed.

Analysis

Droplet size

Droplet size was automatically determined using a custom-written script based on the DIPimage toolbox operating in Matlab 7.0.1. The area of each droplet was determined to be the average over three subsequent frames. Ten subsequent droplets were measured; the droplet area used for further analysis was the average of these ten. The 95 % confidence interval was calculated as the average ± 1.96·standard deviation.

The droplet volume V was calculated from the droplet area. The studied droplets were disc-shaped when the diameter of the droplet was larger than the depth of the microchannel (discs) (see Figure 2a.) or were spherical when the diameter of the droplet was smaller than the depth of the microchannel (drops).

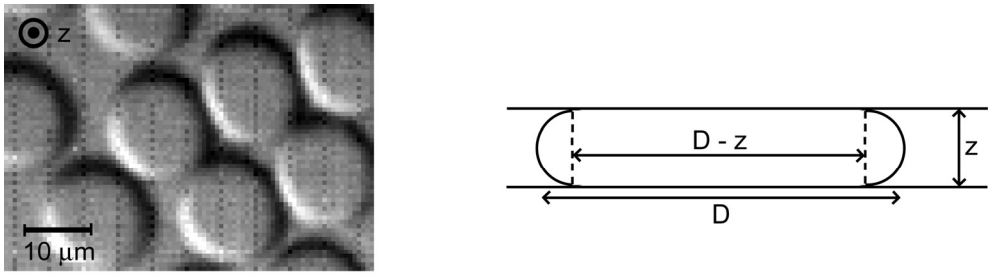

Figure 2: a. DIC (differential interference contrast) image of droplets enclosed in the 5-µm-deep collecting area and b. cross-section of a disc-shaped droplet enclosed in the collecting area.

The smallest curvature of the discs is assumed to be equal to the depth of the microfluidic device (see Figure 2b.); therefore, the accompanying disc volume V is:

$$V = \frac{\pi z}{4}(D-z)^2 + \frac{\pi^2 z^2}{8}\left(D - \left(1 - \frac{4}{3\pi}\right)z\right) \qquad (\mathrm{m}^3) \qquad (1),$$

where D is the diameter of a circle with an area equal to the determined disc area and z is the depth of the microchannels (which is also equal to the depth of the collecting area). To compare drops and discs, the equivalent diameter D_{3D} of an unrestricted spherical drop with the same volume as the disc was calculated and used for further analysis.

Droplet-formation quantities

Two characteristic quantities were defined in the second-to-last frame before droplet detachment: $w_{oil,start}$ and D_{neck} (see Figure 3a.). $w_{oil,start}$ is the width of the oil phase at the corner of the Y-junction and D_{neck} is the width of the thinnest point of the hexadecane filament keeping the droplet attached to the hexadecane bulk (neck).

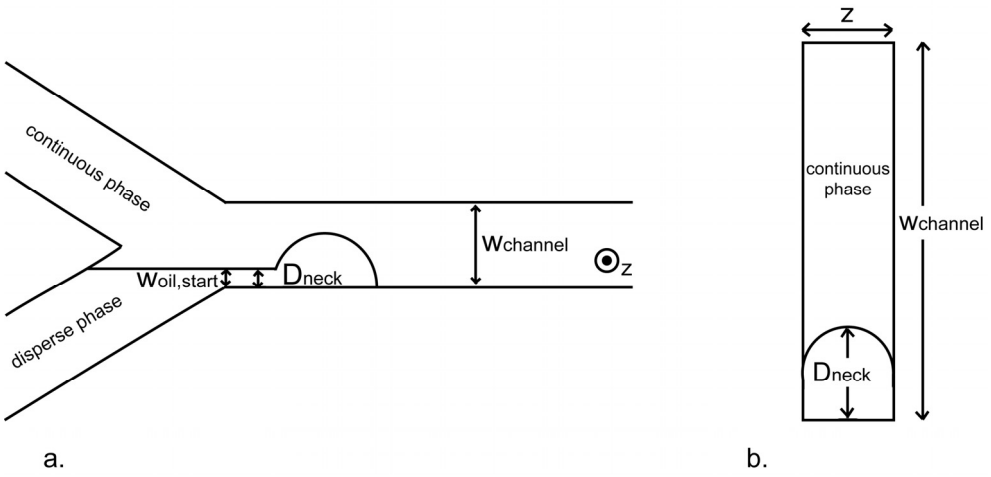

Figure 3: a. Outline of the quantities defined in the second-to-last frame before droplet detachment and b. cross-section through the downstream channel with the oil neck. In both images, the dimensions and angle are not to scale.

The quantities were manually determined with Image-Pro Plus 4.5.0.29. For each quantity, the average of ten incipient droplets was taken, and the accompanying 95 % confidence interval was calculated.

Flow rates at the Y-junction

The flow rates at the actual Y-junction were found to differ from the (applied) flow rates set on the pump, probably because of the large pressure drop in the microfluidic device (in the order of tens of bars). The continuous-phase flow rate ϕ_c at the Y-junction was determined from the velocity of the droplets in the downstream channel, assuming the droplet velocity to be equal to the velocity of the continuous phase. Using Image-Pro Plus 4.5.0.29, the length between the downstream corners of the Y-junction and the left side of the droplet was manually determined in the third frame after detachment and in the frame after which the droplet moved outside the image. Subsequently, the velocity followed from the difference in length divided by the accompanying time between the two frames (see Figures 4 and 5 for the accuracy of the continuous-phase flow rate).

The hexadecane flow rate ϕ_d at the Y-junction was calculated from droplet volume V and droplet-formation frequency f:

$$\phi_d = V \cdot f \qquad (m^3 \cdot s^{-1}) \quad (2)$$

(see Figure 4 and 5 for the accuracy of the disperse-phase flow rate). The actual continuous-phase flow rates at the Y-junction varied from $1.4 \cdot 10^{-2}$ to 0.37 mL·h^{-1}, and the hexadecane flow rates varied from $2.6 \cdot 10^{-4}$ to $5.3 \cdot 10^{-3}$ mL·h^{-1} (which is in contrast to the applied continuous-phase flow rates which vary between 0.15 and 0.35 mL·h^{-1} and the applied hexadecane flow rates which vary between $3.0 \cdot 10^{-4}$ and $1.2 \cdot 10^{-3}$ mL·h^{-1}, as reported previously).

Results and discussion

Droplet formation at Y-junctions

At Y-junctions, both drops and discs are formed through either of two visually discernible mechanisms occurring at the Y-junction (see Figure 4a.) or downstream from the Y-junction (see Figure 4b.). The first mechanism is characterised by snap off at the corner of the Y-junction, and the second mechanism features snap off away from the Y-junction. In the latter mechanism, the incipient droplet is attached to the hexadecane bulk with a hexadecane filament of varying length.

Though the two mechanisms look different, both go through similar stages. First, the hexadecane/ethanol-water interface expands without moving along the downstream channel (see Figure 4a.(B) and 4b.(B)). Subsequently, the hexadecane tip starts to move in the direction of the ethanol-water flow (see Figure 4a.(C) and 4b.(C)) until it remains to the hexadecane bulk with a neck (see Figure 4a.(D) and 4b.(D)). When the neck diameter becomes smaller than the depth of the microchannel, the neck diameter decreases swiftly until the droplet detaches and the hexadecane/ethanol-water interface returns to its original position (see Figure 4a.(E) and 4b.(E)). The similarities between both mechanisms indicate that it might be one droplet-formation mechanism with two break-up points rather than two

different droplet-formation mechanisms. Therefore, initially we will treat them in the same way.

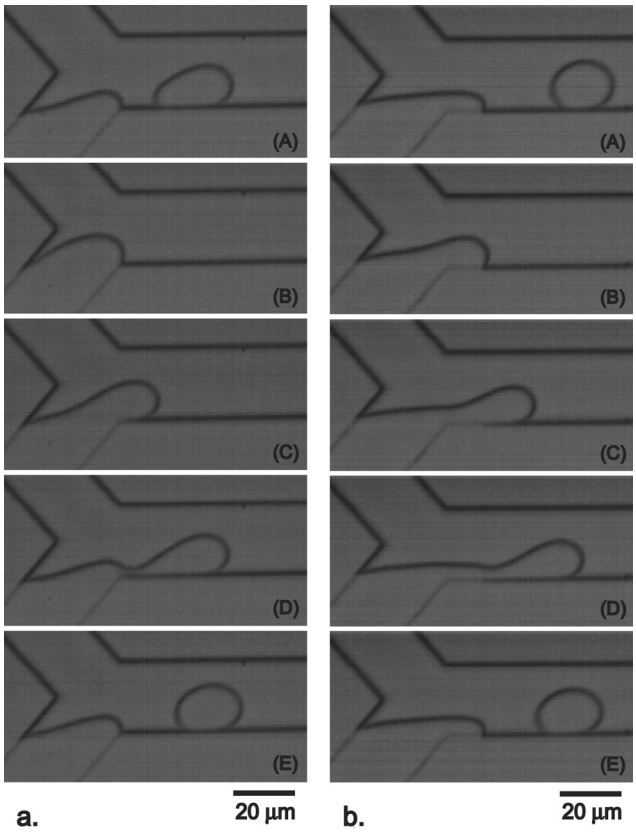

Figure 4: Droplet-formation mechanisms occurring at Y-junctions: a. hexadecane-in-38 wt.% ethanol-water droplet formation at the Y-junction with ϕ_c is $1.7 \cdot 10^{-2}$ ($\pm$ $3.7 \cdot 10^{-4}$) mL·h^{-1} and ϕ_d is $4.1 \cdot 10^{-4}$ ($\pm$ $7.6 \cdot 10^{-6}$) mL·h^{-1}: (A) t = 0 s, (B) t = 4.4 ms, (C) t = 7 ms, (D) t = 8.6 ms, and (E) t = 8.8 ms, b. hexadecane-in-19 wt.% ethanol-water droplet formation downstream from the Y-junction with ϕ_c is $3.8 \cdot 10^{-2}$ ($\pm$ $9.8 \cdot 10^{-4}$) mL·h^{-1} and ϕ_d is $1.0 \cdot 10^{-3}$ ($\pm$ $3.8 \cdot 10^{-5}$ mL·h^{-1}): (A) t = 0 s, (B) t = 1.4 ms, (C) t = 3.1 ms, (D) t = 4.1 ms, and (E) t = 4.3 ms.

Droplet size model

At the Y-junction, monodisperse droplets with a size typically between 4 and 16 μm (see Figure 5) are formed with frequencies of 100 up to 12000 droplets per second. To describe droplet size, a physical force-balance model was derived based on the model by Peng and Williams [18]. The two main forces involved in droplet formation on the micrometer scale are the interfacial tension force and the shear force exerted by the continuous phase. It is assumed that abating (the swift decrease of the neck resulting in detachment) starts when the shear force exceeds the interfacial tension force. As a starting point for our model, we assume that abating is an very fast process that does not contribute to droplet size. Therefore, the eventual droplet size equals the size of the incipient droplet just before abating.

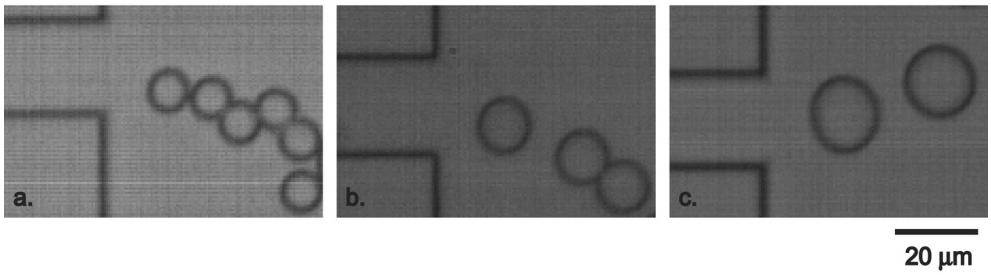

Figure 5: Monodisperse (disc-shaped) droplets in the collecting area. The droplet size depends on the liquid properties and processing conditions: a. hexadecane-in-9 wt.% ethanol-water droplets at ϕ_c 0.17 (± $5.1 \cdot 10^{-3}$) mL·h^{-1} and ϕ_d $3.5 \cdot 10^{-3}$ (± $1.1 \cdot 10^{-4}$) mL·h^{-1}, b. hexadecane-in-66 wt.% ethanol-water droplets at ϕ_c $2.5 \cdot 10^{-2}$ (± $5.0 \cdot 10^{-4}$) mL·h^{-1} and ϕ_d $6.6 \cdot 10^{-4}$ (± $2.1 \cdot 10^{-5}$) mL·h^{-1}, and c. hexadecane-in-Milli-Q water droplets at ϕ_c 0.21 (± $3.9 \cdot 10^{-2}$) mL·h^{-1} and ϕ_d $1.9 \cdot 10^{-3}$ (± $3.5 \cdot 10^{-5}$) mL·h^{-1}.

Just before abating, the incipient droplet remains connected to the bulk with a neck, as was also experimentally observed (see Figure 4a.(D) and 4b.(D)). We assumed that this neck is uniform along the whole downstream channel and has a diameter equal to the depth of the microchannel z, which is 5 μm (see Figure 6a. and b.). Therefore,

$$D_{neck} = w_{oil,start} = z \qquad \text{(m)} \qquad (3).$$

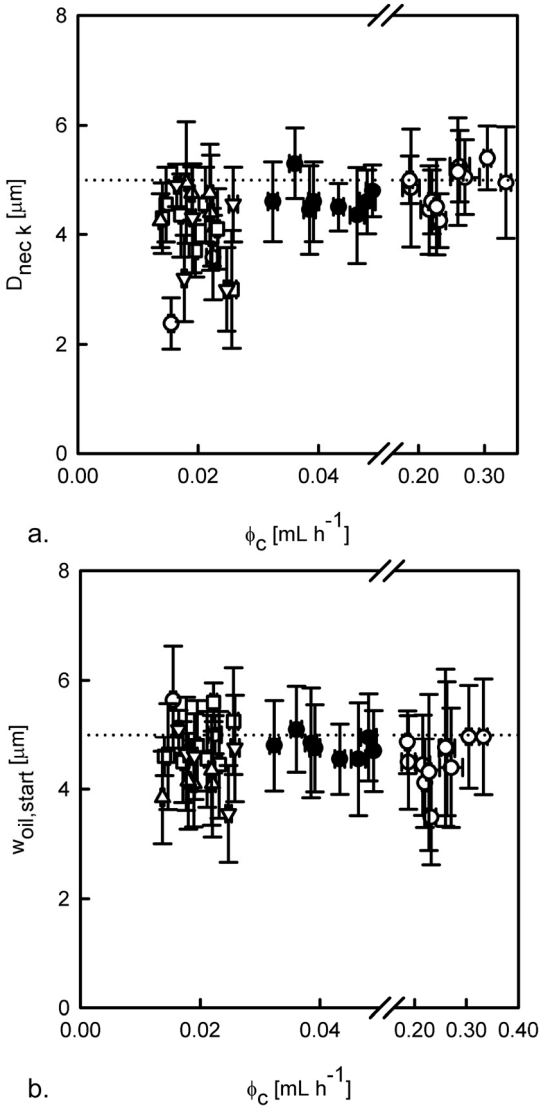

Figure 6: a. D_{neck} and b. $w_{oil,start}$ as functions of the continuous-phase flow rate ϕ_c for various continuous phases: ○ Milli-Q water, ● 19 wt.% ethanol-water, □ 38 wt.% ethanol-water, △ 47 wt.% ethanol-water, and ▽ 66 wt.% ethanol-water. The dotted line indicates the depth of the microchannels. The error bars represent the 95 % confidence interval.

Figure 6 shows some D_{neck} and $w_{oil,start}$ values with a 95 % confidence interval below 5 µm. Values below 5 µm are expected to be linked to a situation when abating has

already started in the penultimate frame before droplet detachment. This happened when more than 20 frames were recorded per droplet, *i.e.* when frame rate and droplet-formation frequency did not match completely. In spite of this, we decided to show all data points without introducing any bias related to preselection from our side.

The interfacial tension acts along the perimeter of the hexadecane neck with an interfacial tension force F_γ (see Figure 3b.):

$$F_\gamma = (2z + \frac{1}{2}\pi z)\gamma \approx 3.57 z\gamma \quad \text{(N)} \quad (4),$$

where γ is the interfacial tension at the oil/continuous-phase interface.

The continuous phase exerts a shear or drag force on the incipient droplet. This shear force is described as the drag exerted by the continuous phase on a sphere with an equivalent diameter of D_{3D} in contact with a wall. Because spheres and discs, the prevalent shapes of incipient droplets in the downstream channel, have similar drag coefficients at low Reynolds number (Re < 10) [19], this is a reasonable assumption. For the continuous phase, Poiseuille flow in a channel with a hydraulic diameter $D_{H,c}$, equal to the hydraulic diameter of the area through which the continuous phase flows, was assumed. The resulting shear force F_{shear} expressed in the equivalent droplet diameter is:

$$F_{shear} = K_{wall} \cdot C_D \cdot v \approx 8.01 D_{3D}^2 \left(\frac{8 v_c \eta_c}{D_{H,c}} \right) \quad \text{(N)} \quad (5),$$

with:

$$v_c = \frac{\phi_c}{z(w_{channel} - 0.89z)} \quad \text{(m·s}^{-1}\text{)} \quad (6) \text{ and}$$

$$D_{H,c} = \frac{4z(w_{channel} - 0.89z)}{1.57z + 2w_{channel}} \quad \text{(m)} \quad (7),$$

where K_{wall} is a correction factor for the wall (we used 1.7 [18]), C_D is the drag coefficient, v is the velocity, v_c is the average velocity of the continuous phase, η_c is the viscosity of the continuous phase, $D_{H,c}$ is the hydraulic diameter of the area

through which the continuous phase can flow past the neck (see Figure 3b.), ϕ_c is the flow rate of the continuous phase at the Y-junction, and $w_{channel}$ is the width of the channel downstream from the Y-junction.

As mentioned previously, just before the abating interfacial tension force and shear force are equal, the droplet size results from equating Equation 4 and 5:

$$D_{3D} = \sqrt{\frac{z^2(w_{channel} - 0.89z)}{4.49(1.57z + 2w_{channel})}} \cdot Ca_c^{-\frac{1}{2}} \quad \text{(m)} \quad (8),$$

where Ca_c is the capillary number of the continuous phase:

$$Ca_c = \frac{v_c \eta_c}{\gamma} \quad \text{(-)} \quad (9).$$

From Equation 8, it is expected that at Y-junctions the droplet size decreases with increasing continuous-phase viscosity, increasing continuous-phase flow rate, and decreasing interfacial tension, as is the case for shear-driven emulsification at T-junctions [6, 7, 20]. Besides, it is also expected that droplet size scales with the depth of the channel. This scaling becomes even clearer when Equation 8 is rewritten as:

$$\frac{D_{3D}}{z} = 0.334 \left(\frac{\frac{w_{channel}}{z} - 0.89}{\frac{w_{channel}}{z} + 0.79} \right)^{\frac{1}{2}} \cdot Ca_c^{-\frac{1}{2}} \quad \text{(-)} \quad (10).$$

Equation 10 shows that the system becomes relatively independent of the width of the channel at large width-to-depth ratios ($w_{channel}/z$). For $w_{channel}/z > 4.5$, *i.e.* for width-to-depth ratios larger than used in this chapter, the value of the geometry factor in Equation 10 increases from 0.83 to 1. In fact, at very large width-to-depth ratios, droplet size would be completely independent of the width of the channel as Equation 10 collapses to:

$$\frac{D_{3D}}{z} = 0.334 \cdot Ca_c^{-\frac{1}{2}} \quad \text{(-)} \quad (11).$$

In that case, it is expected that droplet size is determined by the capillary number of the continuous phase (Ca_c) and the channel depth. Besides this, Equation 11

shows that the droplet size can be tuned by adjusting the continuous phase; the disperse phase influences only the interfacial tension.

Comparison model and experimental data

The force-balance model was compared to forty-eight experimental Y-junction data points in which the continuous-phase flow rate, continuous-phase viscosity, interfacial tension, and hexadecane (disperse- or oil-phase) flow rate were varied (see Figure 7).

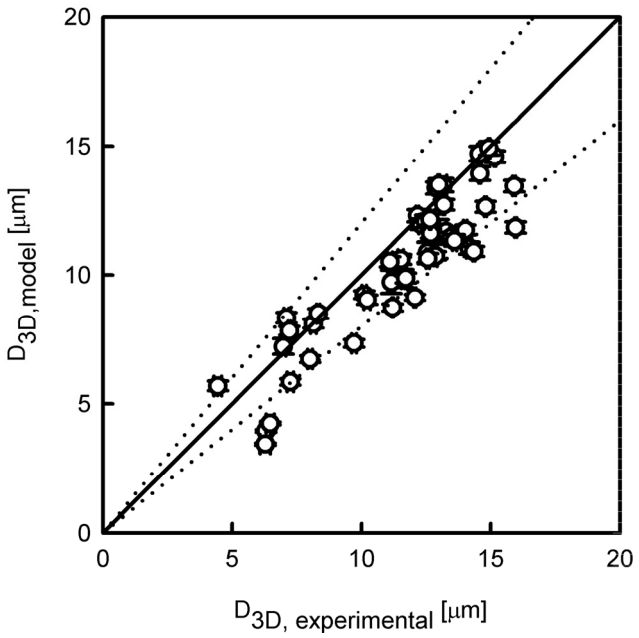

Figure 7: Comparison of the force-balance model to the experimental droplet size D_{3D}. The straight line is the line of parity, and the dotted lines mark 20 % deviation of the experimental droplet size. The error bars (which are relatively small) represent the 95 % confidence interval of the experimental droplet size.

From Figure 7, it is clear that the force-balance model generally describes the experimental droplet sizes within 20 % accuracy. The relatively small error bars are indicative of the monodispersity of the investigated droplets. The droplets have a

polydispersity index below 1 %, which is low compared to other emulsification techniques.

Regression analysis was performed on the data points using SPSS 15.0 based on the linearity of the relation between $Ca_c^{-1/2}$ and D_{3D} (see Equation 8).

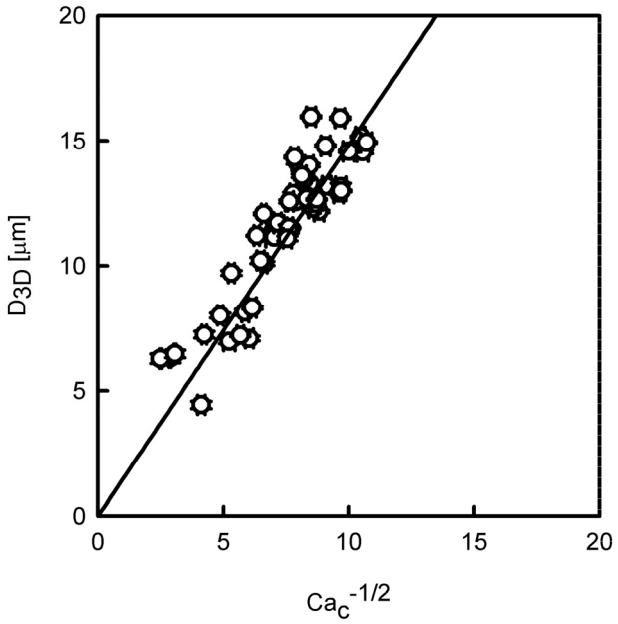

Figure 8: Experimental droplet size D_{3D} as a function of $Ca_c^{-1/2}$. The error bars represent the 95 % confidence intervals of the data points.

Although the current model describes the data points well, as is clear from Figure 8, we determined whether other droplet-formation mechanisms occurred. Therefore, we allowed an intercept:

$$D_{3D} = \beta_0 + \beta_1 Ca_c^{-\frac{1}{2}} \quad (\mu m) \qquad (12)$$

where β_0 is the intercept and β_1 is the slope of the line. A statistically insignificant intercept was found (the 95 % confidence interval included zero). Therefore, the experimental data were best described with a model with only regression parameter

β_1 (see Figure 8 and Table 3). A non-zero intercept could have pointed to a two-step mechanism, which assumes an additional droplet size contribution during necking [18].

Table 3: Estimation regression parameter β_1[a].

	95 % confidence interval β_1			
parameter	lower bound	upper bound	t-value	p-value
β_1	1.4	1.6	61.6	0.00

[a] p values of less than 0.05 were considered statistically significant. (H_0: β_1=0, n=48)

Table 3 shows that β_1 has a statistically significant value of between 1.4 and 1.6. Equation 8 has a slope of 1.4; therefore, the force-balance model is regarded as being statistically sound.

As mentioned previously, the experimental Y-junction data used in the evaluation comprise data from two visually discernible droplet-formation mechanisms (see Figure 4). The fact that both are described with the same force-balance model strengthens our premise that it is one mechanism with two break-up points, and in that sense the two phenomena do not have to be distinguished. For applications, this result suggests that droplet size is independent of the actual appearance of the droplet-formation mechanism.

In our experiments, interfacial tension and both liquid velocities were varied considerably, and the continuous-phase viscosity varied slightly. All of these variations were well covered by the same force-balance model, therewith giving it considerable predictive value for droplet size. Nevertheless, only one oil phase (*i.e.* hexadecane) was used. Therefore, to solidify our model, oils with other viscosities could be tested. In addition, experiments with more viscous continuous phases could contribute to exploring the applicability of our model.

Droplets formed at Y-junctions are monodisperse. Besides, they are formed with a one-step droplet-formation mechanism, in contrast to the more complex two-step mechanism valid for T-junctions [21]. Furthermore, the Y-junction design facilitates

monodispersity because the separate droplets can be stabilised with for example surfactants in the channel downstream from the Y-junction before they contact each other in the collecting area. The fact that droplets do not immediately contact each other after formation is important because fast droplet formation often results in problems with stability in the first moment after detachment because the interface is not yet sufficiently immune to coalescence. To quantify surfactant coverage and therewith droplet stability, the static interfacial tension results obtained in this chapter can form the basis to quantify dynamic interfacial tension effects during droplet formation at flat Y-junctions.

Finally, we draw attention to the fact that the microdevices used in this chapter came from different batches. Therefore, it is plausible that they possessed (slightly) different wetting properties. Because data from all devices were described by the same force-balance model, this may suggest that the exact wetting conditions are not crucial as long as the channel walls are hydrophilic enough to form oil-in-water emulsions.

Conclusion

The force-balance model that was derived showed good predictive value and pointed out that at flat Y-junctions the droplet size is determined by the channel dimensions, especially channel depth, and the capillary number of the continuous phase. The disperse-phase flow rate has no effect on droplet size. This means that when the continuous-phase flow rate is controlled carefully in a given Y-junction, the droplet size can be tuned to specifications. This is an important finding regarding scaling up since it implies that only one phase needs to be controlled instead of two, as is the case for T-junctions or flow-focusing devices.

Acknowledgements

We thank Amal Sawalha for performing the experiments, Michael van Ginkel for writing the droplet analysis script, and MicroNed for supporting this research.

References

1. S. Sugiura, M. Nakajima, J. H. Tong, H. Nabetani and M. Seki, *Journal of Colloid and Interface Science*, 2000, **227**, 95-103.
2. I. Kobayashi, K. Uemura and M. Nakajima, *Colloids and Surfaces A-Physicochemical and Engineering Aspects*, 2007, **296**, 285-289.
3. S. L. Anna, N. Bontoux and H. A. Stone, *Applied Physics Letters*, 2003, **82**, 364-366.
4. T. Nisisako, T. Torii, T. Takahashi and Y. Takizawa, *Advanced Materials*, 2006, **18**, 1152-1156.
5. T. Thorsen, R. W. Roberts, F. H. Arnold and S. R. Quake, *Physical Review Letters*, 2001, **86**, 4163-4166.
6. T. Nisisako, T. Torii and T. Higuchi, *Chemical Engineering Journal*, 2004, **101**, 23-29.
7. S. v. d. Graaf, M. L. J. Steegmans, R. G. M. v. d. Sman, C. G. P. H. Schroën and R. M. Boom, *Colloids and Surfaces A-Physicochemical and Engineering Aspects*, 2005, **266**, 106-116.
8. T. Nisisako and T. Torii, *Lab On A Chip*, 2008, **8**, 287-293.
9. T. Nisisako, T. Torii and T. Higuchi, *Lab On A Chip*, 2002, **2**, 24-26.
10. P. Garstecki, M. J. Fuerstman, H. A. Stone and G. M. Whitesides, *Lab On A Chip*, 2006, **6**, 437-446.
11. S. Okushima, T. Nisisako, T. Torii and T. Higuchi, *Langmuir*, 2004, **20**, 9905-9908.
12. T. Nisisako, S. Okushima and T. Torii, *Soft Matter*, 2005, **1**, 23-27.
13. A. Kawai, S. Matsumoto, H. Kiriya, T. Oikawa, K. Hara, T. Ohkawa, T. Futami, K. Katayama and K. Nishizawa, *TOSOH Research and Technology Review*, 2003, **47**, 3-9.

14. A. Kubo, H. Shinmori and T. Takeuchi, *Chemistry Letters*, 2006, **35**, 588-589.
15. J. Benjamins, A. Cagna and E. H. Lucassen-Reynders, *Colloids and Surfaces A-Physicochemical and Engineering Aspects*, 1996, **114**, 245-254.
16. *CRC Handbook of Chemistry and Physics* 52 edn., The Chemical Rubber Co., Ohio, USA, 1971.
17. L. P. B. M. Janssen and M. M. C. G. Warmoeskerken, *Transport phenomena data companion*, 3rd edn., Delft University Press, Delft, 2001.
18. S. J. Peng and R. A. Williams, *Trans IChemE*, 1998, **76**, 894-901.
19. D. W. Green and R. H. Perry, *Perry's chemical engineers' handbook*, 8th edn., McGraw-Hill, New York, 2007.
20. J. M. Kohler and T. Kirner, *Sensors and Actuators A-Physical*, 2005, **119**, 19-27.
21. M. L. J. Steegmans, C. G. P. H. Schroën and R. M. Boom, *Chemical Engineering Science*, 2009, **64**, 3042-3050.

Chapter 4

Comparative study of droplet formation at microfluidic Y-junctions

This chapter is submitted for publication as research note as: Maartje L.J. Steegmans, Karin G.P.H. Schroën, Remko M. Boom, Comparative study of droplet formation at microfluidic Y-junctions.

Introduction

Many microfluidic devices have been suggested for emulsification. One of the most studied designs is the T-junction [1-6]. Also Y-junctions are reported [7-10], and although their design seems very close to T-junctions, no systematic investigation has yet been carried out regarding the design, and how this relates to the droplet size that can be produced. Therefore, we experimentally investigated the effect of microfluidic (flat) Y-junction design on emulsion droplet size in the dripping and jetting regime for a hexadecane/ethanol-water model system with a range of static interfacial tensions and continuous-phase viscosities, and compared these to results obtained for T-junctions.

Experimental

Materials

Table 1: Viscosity η and static interfacial tension with hexadecane γ_{HD} at 23°C.

sample	η [mPa·s]	γ_{HD} [mN·m^{-1}]
Milli-Q water	1.0	41
9 wt.% ethanol-water	1.5	27
19 wt.% ethanol-water	2.0	20
28 wt.% ethanol-water	2.5	15
38 wt.% ethanol-water	2.6	12
47 wt.% ethanol-water	2.7	10
66 wt.% ethanol-water	2.3	7
hexadecane	3.5	-

Anhydrous n-hexadecane (no. 296317, Sigma-Aldrich, Steinheim, Germany) was used as the to-be-dispersed-phase. Milli-Q water, 9, 19, 28, 38, 47, or 66 wt.% ethanol-water mixtures were prepared from Milli-Q water and 96 %v/v ethanol (no. 20824, VWR BDH Prolabo, Amsterdam, The Netherlands), and were used as continuous phases. The viscosity of these Newtonian liquids was measured in a rheometer (MCR 301, Anton Paar, Graz, Austria) with a Couette geometry (DG

26.7, Anton Paar, Graz, Austria) (see Table 1). The static interfacial tension with hexadecane was measured using a dynamic drop tensiometer (ADT, ITCONCEPT, Longessaigne, France) [10, 11] (see Table 1).

Experimental setup

Microfluidic devices

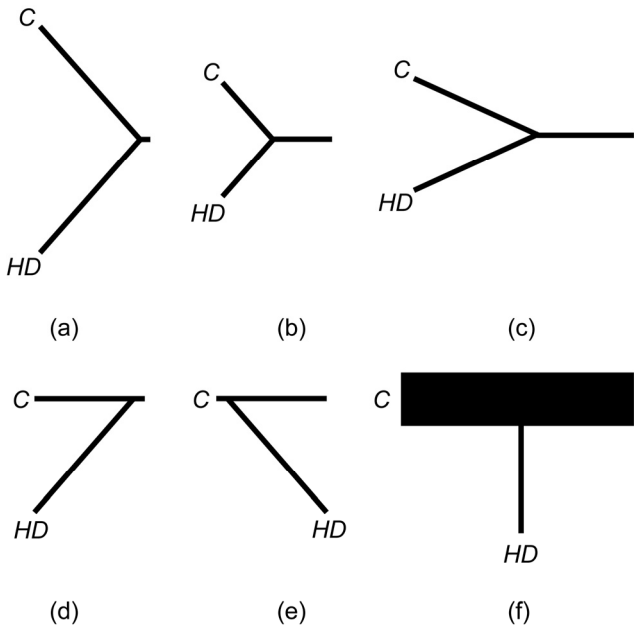

Figure 1: Y- (a to e) and T-junction (f) designs studied. *C* is the continuous-phase channel, *HD* the hexadecane channel, and at the junction between *C* and *HD* droplets are formed.

Borosilicate glass microfluidic devices with various Y- and T-junction designs were produced by Micronit Microfluidics BV (Enschede, The Netherlands) (see Figure 1 and Table 2). The devices consist of a plate in which the channels are (chemically) etched, and which is annealed to a top plate with inlets. The microchannels have a uniform depth of 5 μm and are much wider than deep (flat). The continuous phase

enters the junction via *C* and the hexadecane via *HD*. At the junction, both phases meet and hexadecane droplets are formed (see for instance Figure 3a.).

Table 2: Angle at the junction, length L and width w of the continuous-phase channel *C*, the hexadecane channel *HD*, and the downstream channel for the designs shown in Figure 1.

geometry	angle	L_c	w_c[a]	L_{HD}	w_{HD}[a]	$L_{downstream}$	$w_{downstream}$[a]
	[°]	[mm]	[μm]	[mm]	[μm]	[mm]	[μm]
a.1	97	6.66	23.0 ± 0.4	6.66	23.2 ± 0.4	0.46	23.0 ± 0.5
a.2	97	6.66	18.0 ± 0.5	6.66	18.3 ± 0.5	0.46	18.2 ± 0.5
b	97	3.36	18.4 ± 0.8	3.36	18.3 ± 0.8	2.66	18.3 ± 0.8
c	49	6.04	18.1 ± 0.8	6.04	18.7 ± 0.8	4.40	18.2 ± 0.8
d	49	4.40	18.0 ± 0.8	6.66	18.4 ± 0.8	0.46	18.0 ± 0.8
e	131	0.46	19.0 ± 0.5	6.66	19.3 ± 0.7	4.40	18.8 ± 0.5
f	90	5.13	303 ± 0.8	4.80	24 ± 0.8	5.13	303 ± 0.8

[a] Widths are given with their 95 % confidence interval (average ± 1.96·standard deviation).

Droplet-formation experiments

The microfluidic devices were operated in the appropriate holder (no. 4515, Micronit Microfluidics BV, Enschede, The Netherlands) and the continuous phase and the hexadecane were supplied as described in Chapter 3 and in literature [12]. At continuous-phase flow rates ranging from 0.014 to 0.44 mL·h^{-1} and hexadecane flow rates ranging from 0.29 to 13 μL·h^{-1} droplets were formed at the junctions (flow rates were estimated as described in Chapter 3). After setting the flow rate(s), droplet formation was allowed to equilibrate for at least 2 minutes to ensure steady state.

Droplet formation was recorded using a high-speed camera (MotionPro HS-4, Redlake, Tallahassee, USA) connected to an inverted transmitted light microscope (Axiovert 200, Carl Zeiss, Sliedrecht, The Netherlands). The formation of 25 subsequent hexadecane droplets was recorded using (approximately) 20 frames per droplet, which corresponds to frame rates between 500 and 94500 s^{-1}.

Image Analysis

Droplet size

The hexadecane droplet size was determined either automatically using a custom-written script based on the DIPimage toolbox operating in Matlab 7.0.1, or manually using Image-Pro Plus 4.5.0.29 when image contrast was too low. The area of each droplet was determined as the average over three subsequent frames. Ten subsequent droplets were measured; the reported size was the average of these ten with a 95 % confidence interval.

The droplet volume V was calculated from the droplet area. When the diameter of the droplet was smaller than the depth of the microchannel, the droplet was spherical (drop); otherwise, the droplet was squeezed in between the bottom and top surface and disc-shaped (disc). The volume V of discs was calculated assuming rounded edges with the channel depth as curvature [10]:

$$V = \frac{\pi z}{4}(D-z)^2 + \frac{\pi^2 z^2}{8}\left(D - \left(1 - \frac{4}{3\pi}\right)z\right) \qquad (\mathrm{m}^3) \qquad (1),$$

with D the diameter of a circle with an area equal to the determined disc area, and z the depth of the microchannels. To compare drops and discs, the equivalent diameter D_{3D} of an unrestricted spherical droplet was calculated.

Neck diameter

Just before detachment the droplet is kept to the bulk with a hexadecane filament, which thinnest width D_{neck} was manually determined with Image-Pro Plus 4.5.0.29 in the second-to-last frame before droplet detachment (see Figure 3a. and b.). The reported D_{neck} is the average over ten incipient droplets, and the error due to image analysis is 0.8 μm, at most.

Results and discussion

In Chapter 3, we found that the droplet size at Y-junctions scales with the inverse square root of the capillary number of the continuous phase Ca_c †. Figure 2 shows the data accordingly. For all Y-geometries the droplet size increases (seemingly linearly) with the inverse square root of Ca_c; *i.e.* as expected droplet size increases with increasing interfacial tension and decreasing continuous-phase velocity [8, 10]. Surprisingly, no differences are observed between the various Y-junction designs, which suggests that droplet size and therewith droplet-formation mechanism are not influenced by the junction angle, or the length of the various channels; this is in line with our visual observations. In contrast, for droplets formed at, what we expect are, wider Y-junctions with smaller angles than investigated here, Kawai *et al.* [8] found a decrease in droplet size with increasing angle.

Figure 2 shows that droplets generated at T-junctions are generally larger than at Y-junctions and show more scatter. This results from the fact that the disperse-phase flow rate also determines droplet size at T-junctions [13] and no simple relation with the capillary number is expected, in contrast to at Y-junctions. Droplet formation at T-junctions is described with a two-step droplet-formation model, and T-junctions with various channel sizes show a dependency on the disperse phase [14]; therefore, it seems safe to assume that the difference found here is not related to the width ratio of the channels. Y-junctions are clearly not just a variant of T-junctions, as is often assumed, and seem the preferred option for small monodisperse emulsion droplets.

† Capillary number of the continuous phase is defined as $Ca_c = \eta_c v_c / \gamma_{HD}$, with η_c and v_c the dynamic viscosity and the velocity of the continuous phase, respectively, and γ_{HD} the interfacial tension with hexadecane.

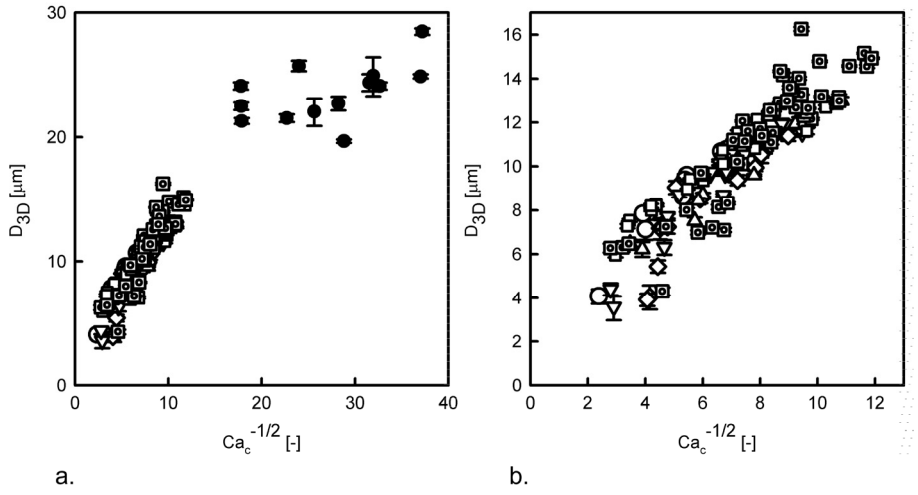

Figure 2: Droplet size D_{3D} as function of the inverse square root of the capillary number of the continuous phase $Ca_c^{-1/2}$ for Y-junctions a.1 (⊡), a.2 (□), b (O), c (◊), d (▽), and e (△), and T-junction f (●) at various flow rates and for various ethanol-water phases. Figure b is an enlargement; the error bars are 95 % confidence intervals.

Another important difference between T- and Y-junctions is observed in the neck diameter: for T-junctions the neck does not become as small as for Y-junctions and at equal neck diameter larger droplets are formed at T-junctions (see Figure 3c.). This may suggest that Y-junctions possibly facilitate deformation of the hexadecane filament resulting in faster collapse of the neck, and this could explain the difference in the observed droplet size.

Figure 3c. shows that for Y-junctions the droplet size is proportional to the diameter of the neck, which is expected assuming a force balance between the shear force and the interfacial tension force acting on the circumference of the neck [10]. Combination of Figures 2 and 3c. (result not explicitly shown) suggests that the neck diameter is proportional to Ca_c^{-1}; which implies that the interfacial tension, the continuous-phase velocity and viscosity determine the size of the neck, and therewith the size of the droplet.

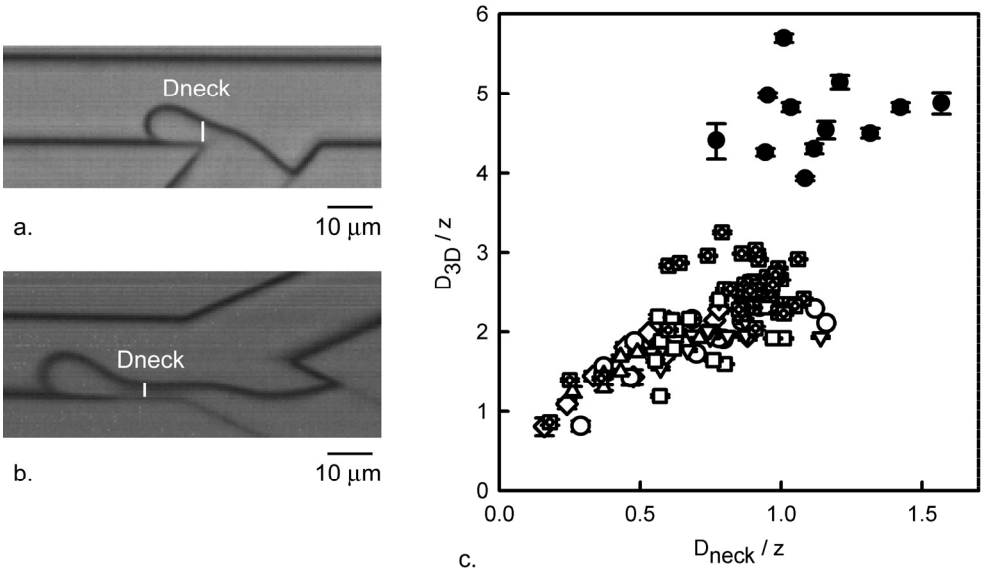

Figure 3: Picture of the neck in a. geometry e: hexadecane-in-19 wt.% ethanol-water (ϕ_c = 6.2·10^{-2} mL·h^{-1}, ϕ_d = 9.6·10^{-4} mL·h^{-1}) and b. geometry c: hexadecane-in-9 wt.% ethanol-water (ϕ_c = 0.10 mL·h^{-1}, ϕ_d = 3.2·10^{-3} mL·h^{-1}). c. dimensionless droplet size D_{3D}/z as function of the dimensionless neck diameter D_{neck}/z for Y-junctions a.1 (⊡), a.2 (□), b (O), c (◊), d (▽), e (△), and T- junction f (●) at various flow rates and for various ethanol-water phases. The error bars represent the 95 % confidence intervals.

There is a great demand for micron-sized, monodisperse emulsion droplets. Y-junctions yield smaller droplets than T-junctions and only the flow rate of the continuous phase needs to be controlled for monodisperse emulsification [10]. In contrast, for T-junctions both flow rates need to be controlled [13]. A complication for parallelising Y-junctions is the fact that two connections are needed to introduce both liquids. Thus, especially designs d and e seem suitable for mass parallelisation, as more oil channels can be positioned around one continuous-phase channel, leading to an area-efficient design (see Figure 4).

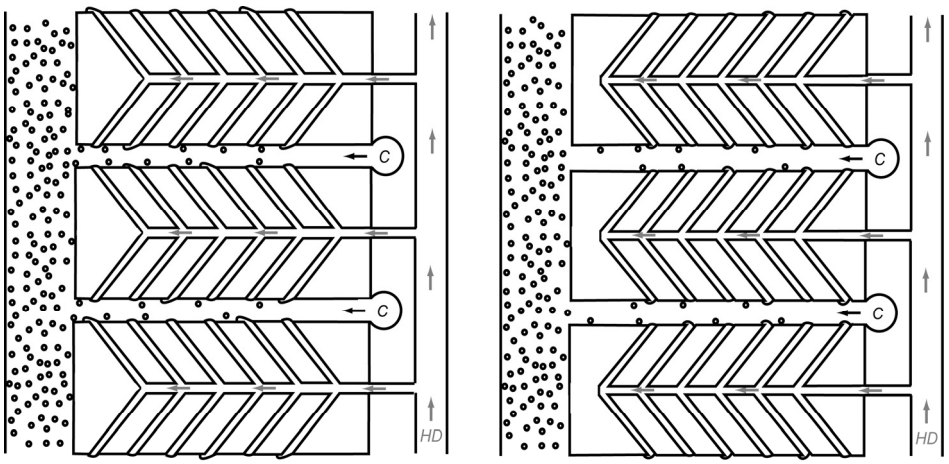

Figure 4: Outline of possible mass-parallelisation of Y-junction design d (a.) and e (b.). *C* represents the inlet of the continuous-phase channel and *HD* the inlet of the hexadecane channel. Dimensions are not to scale.

Acknowledgements

The authors wish to thank Amal Sawalha and Anja Warmerdam for performing part of the experiments, Michael van Ginkel for writing the droplet analysis script, and MicroNed for supporting this research.

References

1. M. De Menech, P. Garstecki, F. Jousse and H. A. Stone, *Journal of Fluid Mechanics*, 2008, **595**, 141-161.
2. P. Garstecki, M. J. Fuerstman, H. A. Stone and G. M. Whitesides, *Lab On A Chip*, 2006, **6**, 437-446.
3. S. v. d. Graaf, T. Nisisako, C. G. P. H. Schroën, R. G. M. v. d. Sman and R. M. Boom, *Langmuir*, 2006, **22**, 4144-4152.

4. T. Nisisako and T. Torii, *Lab On A Chip*, 2008, **8**, 287-293.
5. T. Thorsen, R. W. Roberts, F. H. Arnold and S. R. Quake, *Physical Review Letters*, 2001, **86**, 4163-4166.
6. J. H. Xu, S. W. Li, J. Tan and G. S. Luo, *Microfluidics and Nanofluidics*, 2008, **5**, 711-717.
7. L. Capretto, S. Mazzitelli, C. Balestra, A. Tosi and C. Nastruzzi, *Lab on a Chip*, 2008, **8**, 617-621.
8. A. Kawai, S. Matsumoto, H. Kiriya, T. Oikawa, K. Hara, T. Ohkawa, T. Futami, K. Katayama and K. Nishizawa, *TOSOH Research and Technology Review*, 2003, **47**, 3-9.
9. A. Kubo, H. Shinmori and T. Takeuchi, *Chemistry Letters*, 2006, **35**, 588-589.
10. M. L. J. Steegmans, C. G. P. H. Schroën and R. M. Boom, *Langmuir*, 2009, **25**, 3396-3401.
11. J. Benjamins, A. Cagna and E. H. Lucassen-Reynders, *Colloids and Surfaces A-Physicochemical and Engineering Aspects*, 1996, **114**, 245-254.
12. S. v. d. Graaf, M. L. J. Steegmans, R. G. M. v. d. Sman, C. G. P. H. Schroën and R. M. Boom, *Colloids and Surfaces A-Physicochemical and Engineering Aspects*, 2005, **266**, 106-116.
13. T. Nisisako, T. Torii and T. Higuchi, *Lab On A Chip*, 2002, **2**, 24-26.
14. M. L. J. Steegmans, C. G. P. H. Schroën and R. M. Boom, *Chemical Engineering Science*, 2009, **64**, 3042-3050

Chapter 5

A descriptive force-balance model for droplet formation at microfluidic Y-junctions

Abstract

Droplet formation in microfluidic (flat) Y-junctions was investigated by emulsifying various oils in glycerol-water and ethanol-water mixtures. To describe droplet size in the dripping and jetting regime, a force-balance model was derived at the position where the neck and the incipient droplet are connected. The resulting model describes droplet size for a broad range of process conditions, including continuous- and disperse-phase viscosity. Surprisingly enough, we found that the droplet size is hardly influenced by the disperse-phase viscosity, or the viscosity ratio, but is dominated by the resistance with the wall and the continuous-phase properties.

This chapter is submitted for publication as: Maartje L.J. Steegmans, Jolet de Ruiter, Karin G.P.H. Schroën, Remko M. Boom, A descriptive force-balance model for droplet formation at microfluidic Y-junctions.

Introduction

Traditionally, emulsions are prepared with mixers, rotor-stator systems, ultrasonic or high-pressure homogenisers [1-3]. With these techniques, droplets are formed by elongation and shear, which generally results in a broad droplet size distribution. Therefore, microfluidic emulsification has gained attention, as the produced emulsion droplets are monodisperse.

Microfluidic emulsification includes various geometries with typical channel sizes in the order of several to hundreds of micrometers. The observed droplet-formation mechanism depends on the geometry. In this chapter, we focus on emulsification at microfluidic Y-junctions, which gain little attention in literature. Y-junctions are mainly applied for the production of microspheres [4-6] and, until now, the effect of flow rates, interfacial tension, and continuous-phase properties on emulsion droplet size were studied [5, 7].

Recently, we discovered that emulsification at (flat) Y-junctions is much simpler than in other (shear-driven) microfluidic geometries as the droplet size is independent of the disperse-phase flow rate. In the dripping and jetting regime, droplet size could be described with a force balance between the interfacial tension force and the shear force [7]. The interfacial tension force is the main force keeping the incipient droplet attached to the bulk, and it acts opposite to the shear force exerted by the continuous phase. The derived force-balance model was validated for a broad range of interfacial tensions and flow rates, albeit for only one disperse-phase (viscosity) and a limited range of continuous-phase viscosities [7]. In this chapter, oils with viscosities between 1.0 and 105.0 mPa·s were emulsified in various aqueous continuous phases with viscosities between 1.0 and 6.4 mPa·s, which corresponds to disperse-to-continuous-phase-viscosity ratios between 0.4 and 105.0. The results were used to extend our force-balance model for the dripping and jetting regime to also include *e.g.* viscosity and wall effects.

Experimental

Materials

Disperse phases

n-Hexadecane (anhydrous, purity >99 %, no. 296317, Sigma-Aldrich, Steinheim, Germany), low-viscous paraffin oil (no. 1.07174.1000, Merck, Darmstadt, Germany), high-viscous paraffin oil (no. 1.07160.1000, Merck, Darmstadt, Germany), 40 wt.% pentane-hexadecane or 60 wt.% capric acid-hexadecane mixtures were used as disperse phase. The mixtures were prepared from n-hexadecane and n-pentane (no. 1.07177.1000, Merck, Darmstadt, Germany) or capric acid (purity ≥98 %, no. C1875, Sigma, Zwijndrecht, The Netherlands), respectively. Before use, the paraffin oils and 60 wt.% capric acid-hexadecane mixture were filtered with a hydrophobic 0.2 μm filter (no. 10463503, Whatman, Dassel, Germany). To prevent crystallisation, the 60 wt.% capric acid-hexadecane mixture was heated up to 40 °C and cooled down to 23 °C just before use.

Continuous phases

Milli-Q water, 20, 30, 50 wt.% glycerol-water, 9, or 28 wt.% ethanol-water mixtures were used as the continuous phase. The glycerol-water mixtures were prepared from Milli-Q water and glycerol (purity ≥99.5 %, no. 49767, Fluka, Buchs, Switzerland) and were filtered with a hydrophilic 0.2 μm filter (no. 62131, Alltech, Deerfield, USA). The ethanol-water mixtures were prepared from Milli-Q water and 96 %v/v ethanol (no. 20824, VWR BDH Prolabo, Amsterdam, The Netherlands).

Viscosity

The viscosities of the Newtonian continuous and disperse phases were measured in duplicate in a rheometer (MCR 301, Anton Paar, Graz, Austria) with a Couette geometry (DG 26.7, Anton Paar, Graz, Austria) (see Table 1). For each measurement, a forward and backward rate sweep were performed between 1 to 900 s^{-1} at a controlled temperature of 23 °C. Each of the 18 shear rates was applied

for at least 6 s (900 s^{-1}) up to 30 s (1 s^{-1}) and measurement occurred at the end of each period.

Table 1: Viscosity η and density ρ of the various phases at a temperature of 23°C.

sample[a]	η [mPa·s]	ρ [kg·m^{-3}]
<u>disperse phases</u>		
40 wt.% pentane-hexadecane (PHD40)	1.0	710
hexadecane (HD)	3.5	773
60 wt.% capric acid-hexadecane (CAHD60)	6.4	839
low-viscous paraffin oil (LPO)	29.8	848
high-viscous paraffin oil (HPO)	105.0	860
<u>continuous phases</u>		
Milli-Q water (M)	1.0	996
20 wt.% glycerol-water (G20)	1.8	1045
30 wt.% glycerol-water (G30)	2.6	1071
50 wt.% glycerol-water (G40)	6.2	1124
9 wt.% ethanol-water (E9)	1.5	980
28 wt.% ethanol-water (E28)	2.5	954

[a] The abbreviations used for the various liquids in this chapter are given between brackets.

Density

The densities of the phases were determined in duplicate with a calibrated 49.960 mL Gay-Lussac-type pyknometer (Brand, Wertheim, Germany) at a controlled temperature of 23°C (see Table 1).

Static interfacial tension

The static interfacial tensions (see Table 2) between the various continuous and disperse phases were measured in duplicate at a controlled temperature of 23 °C using a dynamic drop tensiometer (ADT, ITCONCEPT, Longessaigne, France) [8]. A

disperse-phase droplet between 5 to 10 μL was formed at the tip of a U-shaped needle positioned in a cuvette with the continuous phase; to prevent premature droplet detachment the droplet volume was decreased with decreasing interfacial tension. The interfacial tension was determined by droplet shape analysis as described by Benjamins *et al.* [8]. The samples were measured in order of increasing concentration of the continuous phase, and after each concentration, the cuvette and the needle were rinsed extensively with Milli-Q water. Between the various disperse phases and glycerol- and ethanol-water mixtures, the cuvette and the needle were rinsed with hot tap water, chloroform, tap water, and Milli-Q water.

Table 2: Static interfacial tension γ (in $mN \cdot m^{-1}$) at a temperature of 23°C.

disperse phase \ continuous phase	M	G20[a]	G30	G50[a]	E9[a]	E28[a]
PHD40	41	-	37	-	-	-
HD	41	37	35	34	27	15
CAHD60	12	-	12	12	-	-
LPO	49	-	45	39	-	-
HPO	55	-	44	-	-	-

[a] A dash means that the static interfacial tension was not measured.

Experimental setup

Microfluidic Y-junction device

We designed borosilicate glass microfluidic devices with Y-junctions, subsequently produced by Micronit Microfluidics BV (Enschede, The Netherlands) (for further details see Steegmans *et al.* [7]). The microfluidic device consists of a bottom plate in which the Y-channels are (chemically) etched, and which is annealed to a top plate with inlets. After enclosure, the microchannels and collecting area have a uniform depth of 5 μm.

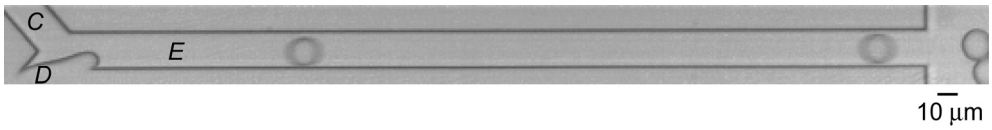

Figure 1: Picture of the Y-junction. Low-viscous paraffin oil droplets are formed in 30 wt.% glycerol-water at ϕ_{G30} = 89 (± 2) µL·h^{-1} and ϕ_{LPO} = 2.5 (± 0.1) µL·h^{-1}. All intervals given in this chapter for the continuous- and disperse-phase flow rate are derived from image analysis assuming a maximal experimental error of one pixel or one frame.

Figure 1 shows a picture of the Y-junction. The continuous phase enters the Y-junction via channel *C*, while the disperse phase enters via channel *D*. The angle between channels *C* and *D* is 97°. At the Y-junction, both phases meet and droplets are formed, which are transported through channel *E* towards the collecting area. Except for one device, channel width was between 18 and 20 µm (see Table 3).

Table 3: Width of the continuous-phase channel w_C, disperse-phase channel w_D, and downstream channel w_E of the studied microfluidic Y-junctions, which have a uniform depth of 5 µm. The disperse and continuous phase(s) used in each Y-junction are specified as well.

disperse phase	continuous phase	w_C[a] [µm]	w_D[a] [µm]	w_E[a] [µm]
PHD40	M, G30	18.8	19.2	19.0
PHD40	M, G30	18.6	18.9	18.9
HD	M, E9, E28	18.0	18.2	18.1
HD	M, G20	18.2	18.1	18.1
HD	M, G20	19.4	19.8	19.7
HD	G20, G30	19.4	19.9	19.6
CAHD60	M, G30	18.7	19.1	18.9
CAHD60	G30, G50	19.0	19.1	19.1
LPO	M, G30	19.0	19.0	19.1
HPO	M, G30	19.6	19.6	19.6
HD	M, G20, G30	12.9	13.1	12.8

[a] Measurement error is ± 0.5 µm.

Droplet-formation experiments

The Y-junction devices were operated in the appropriate holder (no. 4515, Micronit Microfluidics BV, Enschede, The Netherlands) and the continuous and disperse phase were supplied as described in Chapter 3. The actual flow rates were calculated to range from 1.39 $\mu L \cdot h^{-1}$ to 0.41 $mL \cdot h^{-1}$ for the continuous phase, and from 0.039 to 18.0 $\mu L \cdot h^{-1}$ for the disperse phase (for details on the calculation see Steegmans *et al.* [7]). After changing the flow rate(s), the droplet-formation process was allowed to equilibrate for at least 2 minutes.

Droplet formation in the dripping and jetting regime was recorded using a high-speed camera (MotionPro HS-4, Redlake, Tallahassee, USA) connected to an inverted transmitted light microscope (Axiovert 200, Carl Zeiss, Sliedrecht, The Netherlands). The formation of 25 subsequent hexadecane droplets was recorded using (approximately) 20 frames per droplet, which corresponds to frame rates between 210 and 73502 s^{-1}. The gain and the exposure time were chosen such that the image quality was optimal.

Analysis

Droplet size

The hexadecane droplet size was determined automatically using a custom-written script based on the DIPimage toolbox operating in Matlab 7.0.1. The area of each droplet was determined as the average over three subsequent frames. Ten subsequent droplets were measured; the reported size was the average of these ten with a 95 % confidence interval (average ± 1.96·standard deviation).

The droplet volume V was calculated from the droplet area. When the diameter of the droplet was smaller than the depth of the microchannel, the droplet was spherical (drop); otherwise, the droplet was squeezed in between the bottom and top surface and disc-shaped (disc). The volume V of discs was calculated assuming rounded edges with the channel depth as curvature [7]:

$$V = \frac{\pi z}{4}(D-z)^2 + \frac{\pi^2 z^2}{8}\left(D - \left(1 - \frac{4}{3\pi}\right)z\right) \qquad (\mathrm{m}^3) \qquad (1),$$

with D the diameter of a circle with an area equal to the determined disc area and z the depth of the microchannels. To compare drops and discs, the equivalent diameter D_{3D} of an unrestricted spherical droplet was calculated from Equation 1.

Droplet-formation quantities

Two characteristic droplet-formation quantities were determined in the second-to-last frame before droplet detachment: D_{head} and D_{neck} (see Figure 2). D_{head} is the largest diameter of the incipient droplet head and D_{neck} is the width of the thinnest point of the filament keeping the droplet attached to the disperse-phase bulk (neck). The quantities were manually determined with Image-Pro Plus 4.5.0.29. For each quantity, the average of ten incipient droplets was taken, and a corresponding 95 % confidence interval was calculated.

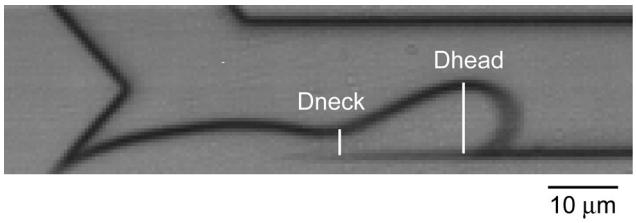

Figure 2: Picture of the second-to-last frame before low-viscous paraffin oil droplet detachment in 30 wt.% glycerol with herein indicated droplet-formation quantities D_{head} and D_{neck}. Flow rates are as stated for Figure 1.

Statistical analysis

The relation between D_{head} and D_{3D}, as described in the results section, was established using the least squares method. The standard deviations of the parameters (*a*, *b*, and *c*) were estimated as the product of the square root of the residual mean square and the square root of the variance of the parameter.

Minimal sum of squares, parameters, and standard deviations were found with the Levenberg-Marquardt method in Mathcad 14.

Results and discussion

Critical capillary number for Y-junctions

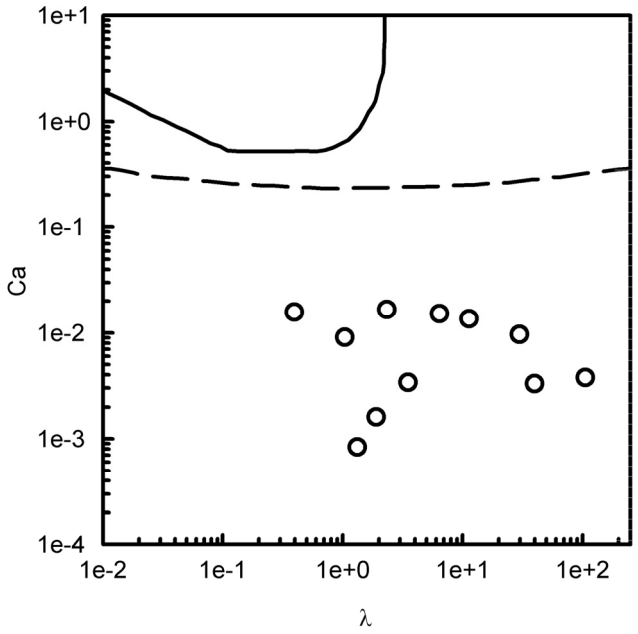

Figure 3: The critical capillary number ($Ca = (\gamma R_{3D}\eta_c)/\gamma$) as function of the disperse-to-continuous-phase-viscosity ratio λ. The spheres (O) are the capillary numbers obtained in our Y-junctions for the dripping and jetting regime. The solid line is the curve for (rotational) shear flow and the dashed line the curve for elongational flow after Grace, Fig. 19 [9].

At microfluidic Y-junctions in the dripping and jetting regime, monodisperse micron-sized droplets with a polydispersity index (standard deviation to average droplet size ratio) below 1 % were formed with frequencies of 10 up to more than 10000 droplets per second. In emulsification literature, it is common to use a critical capillary number for droplet break-up. For microfluidic Y-junctions, the

determined capillary numbers ($Ca = (\dot{\gamma} R_{3D} \eta_c)/\gamma$) for micron-sized droplets are in the order of 10^{-3} to 10^{-2} (see Figure 3), which is at least ten, but in most cases, one hundred times or more lower than reported by Grace [9] for millimetre-sized emulsion droplets generated by elongation or rotation. This implies that in microfluidic Y-junctions shear is used more efficiently to form droplets than in (rotational) shear or elongation. In other words, this finding seems to be an indication that geometric confinement in combination with angular channels promotes instability of the liquid column and therewith droplet break-up [10]. Besides, for microfluidic Y-junctions the dependency on viscosity ratio seems less pronounced than for (rotational) shear or elongation, which might indicate viscosity ratio independency.

Droplet formation at Y-junctions

In the next sections, the effect of *e.g.* viscosity ratio on emulsion droplet size at microfluidic Y-junctions is studied more extensively. We start by visual observation of the droplet-formation process. Regardless of the properties of the disperse and/or the continuous phase, we observed that droplet formation starts with interface expansion without movement along the downstream channel (see Figure 4a.B to 4d.B). Subsequently, the tip of the disperse phase starts to move along the downstream channel in the direction of the continuous-phase flow (see Figure 4a.C to 4d.C), until the incipient droplet is connected to the bulk with a neck (see Figure 4a.D to 4d.D). Then, the diameter of the neck swiftly decreases and the droplet detaches, after which the interface returns to its original position (see Figure 4a.E to 4d.E).

Emulsion droplet formation occurs either at the Y-junction (dripping, see Figure 4a. and c.) or downstream, near the bottom wall (jetting, see Figure 4b. and d.). For 40 wt.% pentane-hexadecane, hexadecane, low-viscous and high-viscous paraffin oil, monodisperse emulsion droplets were formed with both mechanisms, but for 60 wt.% capric acid-hexadecane this occurs only downstream. We previously found that both droplet formation at the junction and downstream can be treated as one

for the force-balance analysis [7], and therefore in the remainder of this chapter the two mechanisms will not be distinguished.

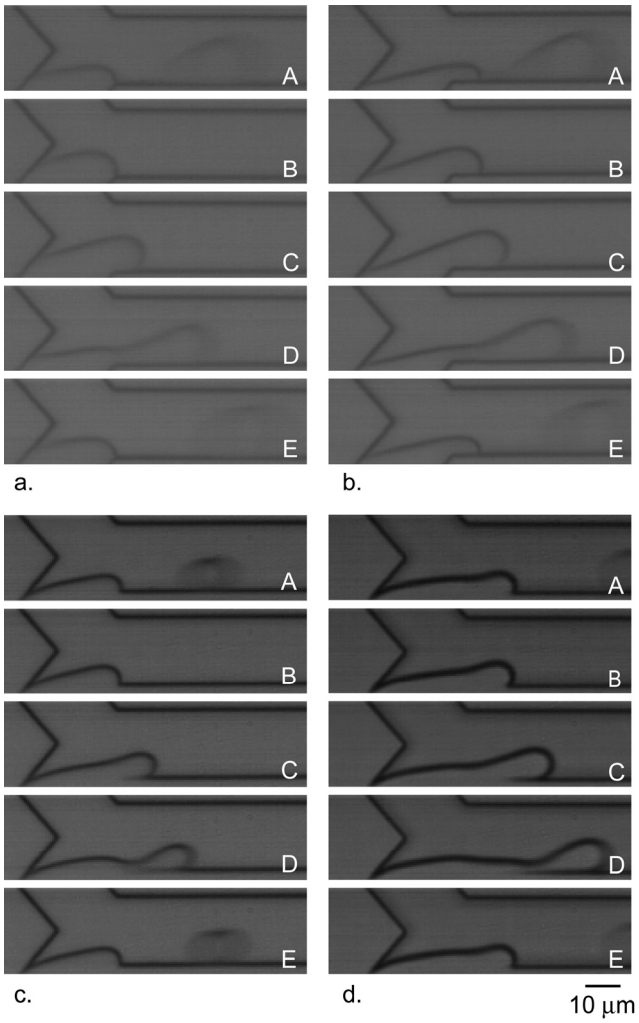

Figure 4: Droplet-formation at the Y-junction (dripping, a. and c.) and droplet formation downstream (jetting, b. and d.). For further details on the process conditions, see Table 4.

Table 4: Details of the pictures shown in Figure 4.

picture	disperse phase	continuous phase	ϕ_d [μL·h^{-1}]	ϕ_c [μL·h^{-1}]	time [ms]				
					A	B	C	D	E
a.	PHD40	M	9.4 ± 0.08	260 ± 8	0	0.08	0.22	0.32	0.36
b.	PHD40	M	8.2 ± 0.3	210 ± 9	0	0.14	0.27	0.39	0.43
c.	LPO	G30	2.2 ± 0.02	185 ± 6	0	0.11	0.43	0.54	0.60
d.	LPO	M	3.3 ± 0.1	256 ± 8	0	0.07	0.4	0.6	0.67

Force-balance model development

To estimate the droplet size at Y-junctions for different disperse-phases, we adapted the existing force-balance model [7] by redefining the interfacial tension force F_γ and the shear force F_{shear}. We assume that abating (the swift decrease of the neck resulting in detachment) is infinitely fast in the dripping and jetting regime, which implies that the eventual droplet size equals the droplet size when abating starts, *i.e.* when both forces are equal:

$$F_\gamma = F_{shear} \qquad \text{(-)} \qquad (2).$$

In the next sections, the various steps that were taken to redefine the interfacial tension force and the shear force are systematically presented.

Interfacial tension force

The diameter of the neck was experimentally determined, and as the disperse phase tends to minimise its contact area with the continuous phase, the neck was assumed to be cylindrical (see Figure 5). The interfacial tension force can therefore be estimated with:

$$F_\gamma = \pi D_{neck} \gamma \qquad \text{(N)} \qquad (3).$$

In Chapter 3, we assumed that the neck diameter is approximately equal to the channel depth (5 μm), but from the current investigation, it is clear that this is not the case for all disperse phases as shown in Figure 5c. Figure 5c suggests that the

neck diameter depends on the disperse phase, but no straightforward relation to describe this effect is available. Therefore, the experimentally determined value of D_{neck} is used when D_{neck} is below channel depth, otherwise $D_{neck} = z$, since the neck cannot start abating as long as $D_{neck} > z$.

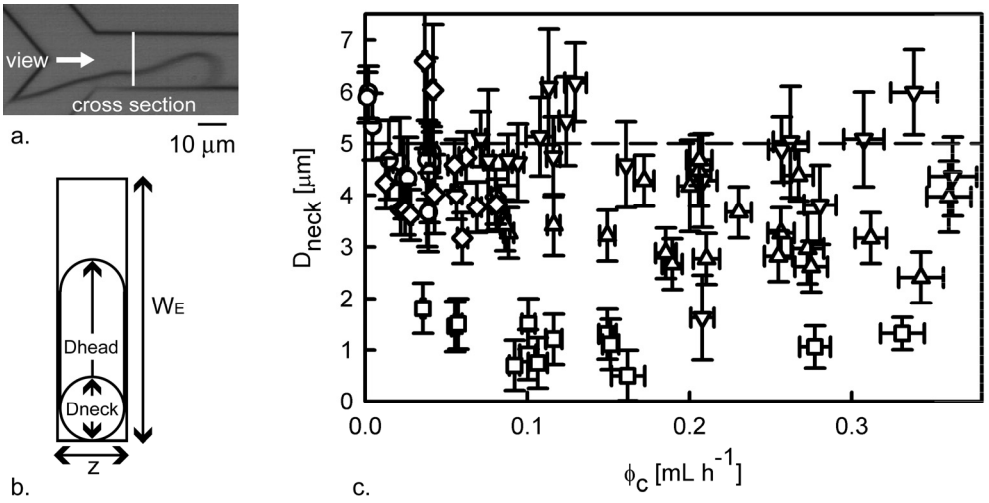

Figure 5: a. Picture of the second-to-last frame before hexadecane droplet detachment in 20 wt.% glycerol at ϕ_{G20} = 115 (± 5) µL·h^{-1} and ϕ_{HD} = 4.5 (± 0.1) µL·h^{-1}. The white line marks the position of the schematic cross-section shown in Figure 5b and the white arrow indicates the point of view. b. Schematic cross-section at the position where the neck is connected to the incipient droplet head (see Figure 5a). c. The neck diameter D_{neck} as function of the glycerol-water flow rate ϕ_c for various disperse phases: 40 wt.% pentane-hexadecane (▽), hexadecane (○), 60 wt.% capric acid-hexadecane (□), low-viscous paraffin oil (△), and high-viscous paraffin oil (◊). The dashed line indicates the channel depth.

Shear force

The shear force is based on the general drag equation [11]. For the cross-sectional area of the incipient droplet head exposed to the continuous-phase flow (*i.e.* minus the area shaded by the neck, see Figure 5) in a rectangular channel:

$$F_{shear} = 1.125 \rho_c v_c^2 A_{\perp} K_{wall} C_D \Lambda \quad \text{(N)} \qquad (4),$$

where ρ_c is the continuous-phase density, v_c is the (average) velocity of the continuous phase along the neck calculated with Equation 5, $A_\perp$ is the cross-sectional area of the incipient droplet head exposed to the continuous-phase flow calculated with Equation 6 or 7, K_{wall} is the wall correction factor, C_D is the drag coefficient, and Λ is the Hadamard viscosity correction factor [12-14]. The velocity along the neck is calculated as:

$$v_c = \frac{\phi_c}{A_{\perp,E} - A_{\perp,neck}} = \frac{\phi_c}{z w_E - \frac{\pi}{4} D_{neck}^2} \quad (\mathrm{m \cdot s^{-1}}) \quad (5),$$

where ϕ_c is the continuous-phase flow rate, $A_{\perp,E}$ is the cross-sectional area of the downstream channel, and w_E is the downstream-channel width. The cross-sectional area of the incipient droplet head exposed to the continuous phase $A_\perp$ is calculated for $D_{head} > z$ as:

$$A_\perp = A_{\perp,head} - A_{\perp,neck} = \frac{\pi}{4}\left(z^2 - D_{neck}^2\right) + z\left(D_{head} - z\right) \quad (\mathrm{m^2}) \quad (6), \text{ and}$$

otherwise (*i.e.* $D_{head} \leq z$):

$$A_\perp = A_{\perp,head} - A_{\perp,neck} = \frac{\pi}{4}\left(D_{head}^2 - D_{neck}^2\right) \quad (\mathrm{m^2}) \quad (7),$$

where $A_{\perp,head}$ is the cross-sectional area of the head and $A_{\perp,neck}$ that of the neck.

Wall correction factor

During droplet formation, the incipient droplet head is in contact with the channel wall. When the cross-sectional area of the downstream channel is largely occupied by the head, the resistance coefficient between the head and the wall can be described with [12, 15]:

$$K_{wall}(k,e) = 0.83\alpha_0(e)\left(k^{-\frac{5}{2}} + (2.62 + \alpha_1(e))k^{-\frac{3}{2}} + (2.01 + \alpha_t(e))k^{-\frac{1}{2}}\right) + \ldots \text{ (for k<1)(-)} \quad (8),$$

where k is the clearance between the channel and the droplet head defined for Y-junctions as:

$$k = \frac{w_E - D_{head}}{D_{head}} \quad (-) \quad (9),$$

e is a measure for the position of the centre of the droplet head compared to the wall, and $\alpha_0(e)$, $\alpha_1(e)$, and $\alpha_t(e)$ are (complex) functions which describe the resistance at position *e*. At the wall (*i.e.* $e = 1$), $\alpha_0(e)$, and $\alpha_1(e)$ attain finite limiting values of 0.52 and 0.27, respectively [15]. The exact expression of $\alpha_t(e)$ is unknown, but as it is of the order $k^{1/2}$ [15] it can be neglected for *k* values below one, so Equation 8 becomes:

$$K_{wall}(k) = 0.43\left(k^{-\frac{5}{2}} + 2.89k^{-\frac{3}{2}} + 2.01k^{-\frac{1}{2}}\right) + \ldots \quad \text{(for k < 1)(-)} \quad (10).$$

For *k* values larger than one, *i.e.* for small cross-sectional droplet head area [16, 17]:

$$K_{wall} = 1.7 \quad \text{(for k ≥ 1)(-)} \quad (11).$$

Drag coefficient and Hadamard viscosity correction factor

The Reynolds numbers in our Y-junctions are typically between 0.1 and 10. In this Reynolds number range, liquid discs and spheres have comparable drag coefficients described as [11, 13]:

$$C_D\Lambda = \frac{24}{\mathrm{Re}_c}\left(1 + 0.14 \cdot \mathrm{Re}_c^{0.7}\right)\Lambda \quad (-) \quad (12)$$

with:

$$\Lambda = \frac{3\lambda + 2}{3(\lambda + 1)} \quad (-) \quad (13),$$

where λ is the (dynamic) viscosity ratio and Re_c is the Reynolds number of the continuous phase. These quantities are calculated as:

$$\lambda = \frac{\eta_d}{\eta_c} \quad (-) \quad (14) \text{ and}$$

$$\mathrm{Re}_c = \frac{\rho_c v_c D_{H,c}}{\eta_c} \quad (-) \quad (15), \text{ with}$$

$$D_{H,c} = \frac{4(A_{\perp,E} - A_{\perp,neck})}{U_{\perp,E}} = \frac{2}{z + w_E}\left(zw_E - \frac{\pi}{4}D_{neck}^2\right) \quad \text{(m)} \quad (16),$$

where η_d and η_c are the disperse- and continuous-phase dynamic viscosity, respectively, $D_{H,c}$ is the hydraulic diameter of the area through which the continuous phase can flow past the neck, and $U_{\perp,E}$ is the perimeter of the downstream channel.

Force-balance model

From all the information mentioned in the section 'Force-balance model development', droplet size follows from equating the interfacial tension force and the shear force (*i.e.* Equation 3 and 4):

$$\pi D_{neck}\gamma = 2\rho_c v_c^2 A_\perp(D_{head})K_{wall}(D_{head})C_D\Lambda \quad \text{(-)} \quad (17).$$

This results in a complex equation, as both $A_\perp$ and K_{wall} are a function of D_{head}. Therefore, it was solved numerically with a script written in Matlab 7.0.1. This script determines F_{shear} for D_{head} values between 0 and 20 μm in steps of 0.1 μm, and returns the D_{head} for which F_{shear} equals F_γ.

Equivalent droplet size

As a final step, D_{head} is related to the unrestricted droplet diameter D_{3D} as this is a more prevalent quantity. Since the shape of the incipient droplet is complex, we derived an empirical relation through statistical analysis (implying no physical meaning):

$$D_{head} = \frac{1}{a + \dfrac{b}{D_{3D}^c}} \quad \text{(m)} \quad (18),$$

where a, b, and c are parameters with a 95 % confidence interval of $3.9\cdot10^{-2} \pm 8.2\cdot10^{-3}$, 3.8 ± 1.6, and 1.7 ± 0.2, respectively (see Figure 6).

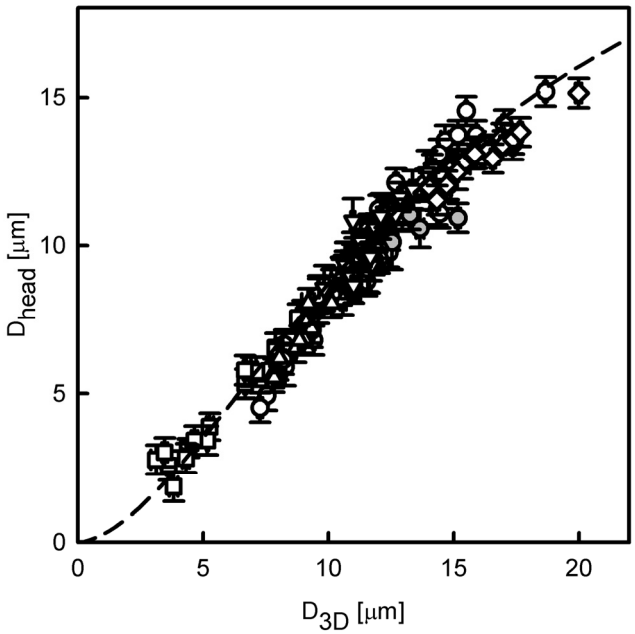

Figure 6: D_{head} as function of D_{3D} in the dripping and jetting regime at microfluidic Y-junctions for: 40 wt.% pentane-hexadecane (▽), hexadecane (○), 60 wt.% capric acid-hexadecane (□), low-viscous paraffin oil (△), and high-viscous-paraffin oil (◊) at various continuous- and disperse-phase flow rate, static interfacial tension, and continuous-phase viscosity as described in the experimental section. The grey filled circles are for the smaller channel width. The dashed line is Equation 18.

Comparison model and experimental data

The force-balance model was compared to all 137 experimental Y-junction data, and Figure 7 shows that all data were described adequately, irrespective of the considerable differences in disperse- and continuous-phase viscosity (η_d = 1.0 to 105.0 mPa·s, η_c = 1.0 to 6.2 mPa·s), flow rate (ϕ_d = 0.039 to 18.0 μL·h^{-1}, ϕ_c = 1.39 μL·h^{-1} to 0.41 mL·h^{-1}), (static) interfacial tension (γ = 12 to 55 mN·m^{-1}), and channel width (12.8 to 19.9 μm). Therewith, it is clear that the model has considerable predictive value, and covers factors that were not implemented before. For droplets

between 9 and 10 μm a slight overestimation of the force-balance model can be observed; most probably this is caused by the changeover from one K_{wall} equation to the other (Equations 10 and 11).

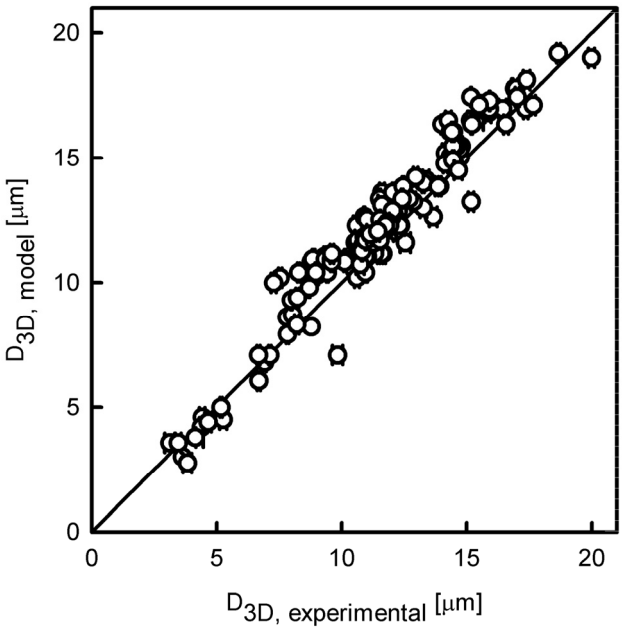

Figure 7: Comparison of the droplet size estimated with the force-balance model to the experimental droplet size D_{3D} for various process conditions as described in the experimental section. The diagonal line is the line of parity and the error bars represent the 95 % confidence interval of the experimental droplet size.

The sensitivity of the force-balance model was tested by leaving out the viscosity correction factor Λ or the wall correction factor K_{wall}. The standard deviation between the adjusted force-balance models and the data points was calculated. Table 5 shows that the influence of the viscosity correction factor is insignificant, especially when compared to the effect of the wall correction factor. This finding strongly suggests that emulsification in Y-junctions is ruled by the resistance with the wall, and not by disperse-phase viscosity, or viscosity ratio, as is observed for other emulsification systems (*e.g.* see Figure 3).

Table 5: Standard deviation between the force-balance model and the data points for the complete force-balance model (Equation 17 and 18), the model without the viscosity or the wall correction factor, and the model based on the assumption that $D_{neck} = z$.

model	standard deviation[a] [μm]
model following Equation 17 and 18	1.1
model without viscosity correction factor	1.0
model without wall correction factor	65.5
model assuming D_{neck} equals z	2.1

[a] $\sqrt{(SS/(n-1))}$, with SS the sum of squares and n the number of data points.

As mentioned previously, the initial Y-junction model [7] assumed D_{neck} equal to the channel depth (z), but current results suggest that this is not always correct (see Figure 5c), and that is also reflected in the predicted droplet sizes. When it was assumed that $D_{neck} = z$, the standard deviation doubled (see Table 5). This suggests that the D_{neck} value is clearly essential for the description of the data points. Ideally, this value, which can only be determined experimentally, should become more accessible. For this, the contact angle between the microchannel wall and the liquids could be a starting point as it plausibly influences the shape of the neck, but unfortunately, this parameter is not (easily) accessible under the conditions studied here.

Conclusion

Microfluidic Y-junctions were used to produce monodisperse emulsions. A force-balance model was derived based on the cross-sectional area of the incipient droplet just before detachment from a neck with a cylindrical shape. The model shows good predictive value for emulsification in microfluidic Y-junctions in the dripping and jetting regime over a broad range of disperse- and continuous-phase viscosities, flow rates, and interfacial tensions. The model shows that the droplet size generated by Y-junctions is controlled by interfacial tension, continuous-phase properties (viscosity, density, and flow rate), and resistance with the wall, and is independent of the disperse-phase viscosity, and viscosity ratio. As droplet size is

also not influenced by disperse-phase flow rate [7], operation of Y-junctions is intrinsically simpler than other (shear-driven) microfluidic geometries.

Acknowledgements

The authors wish to thank Anja Warmerdam for performing part of the experiments, Michael van Ginkel for writing the script for droplet analysis, and the MicroNed consortium for supporting this research.

References

1. V. Schröder and H. Schubert, *Colloids and Surfaces A-Physicochemical and Engineering Aspects*, 1999, **152**, 103-109.
2. D. J. McClements, *Food Emulsions - principles, practices and techniques*, 2nd edn., CRC Press, 2005.
3. S. M. Joscelyne and G. Trägårdh, *Journal of Food Engineering*, 1999, **39**, 59-64.
4. L. Capretto, S. Mazzitelli, C. Balestra, A. Tosi and C. Nastruzzi, *Lab on a Chip*, 2008, **8**, 617-621.
5. A. Kawai, S. Matsumoto, H. Kiriya, T. Oikawa, K. Hara, T. Ohkawa, T. Futami, K. Katayama and K. Nishizawa, *TOSOH Research and Technology Review*, 2003, **47**, 3-9.
6. A. Kubo, H. Shinmori and T. Takeuchi, *Chemistry Letters*, 2006, **35**, 588-589.
7. M. L. J. Steegmans, C. G. P. H. Schroën and R. M. Boom, *Langmuir*, 2009, **25**, 3396-3401.
8. J. Benjamins, A. Cagna and E. H. Lucassen-Reynders, *Colloids and Surfaces A-Physicochemical and Engineering Aspects*, 1996, **114**, 245-254.
9. H. P. Grace, *Chemical Engineering Communications*, 1982, **14**, 225-277.
10. P. Guillot, A. Colin and A. Ajdari, *Physical Review E - Statistical, Nonlinear, and Soft Matter Physics*, 2008, **78**.

11. D. W. Green and R. H. Perry, *Perry's chemical engineers' handbook*, 8th edn., McGraw-Hill, New York, 2007.
12. H. Shintaku, T. Kuwabara, S. Kawano, T. Suzuki, I. Kanno and H. Kotera, *Microsystem Technologies*, 2007, **13**, 951-958.
13. J. Husny and J. J. Cooper-White, *Journal of Non-Newtonian Fluid Mechanics*, 2006, **137**, 121-136.
14. Y. C. Chang and H. J. Keh, *Journal of Fluids and Structures*, 2006, **22**, 647-661.
15. P. M. Bungay and H. Brenner, *International Journal of Multiphase Flow*, 1973, **1**, 25-56.
16. M. E. O'Neill, *Chemical Engineering Science*, 1968, **23**, 1293-1298.
17. P. M. Bungay and H. Brenner, *Journal of Fluid Mechanics*, 1973, **60**.

Chapter 6

Dynamic interfacial tension measurements with microfluidic Y-junctions

Abstract

Emulsification in microdevices (microfluidic emulsification) involves micrometer-sized droplets and fast interface expansion rates. In addition, droplets are formed in less than milliseconds, and therefore traditional tensiometric techniques cannot be used to quantify the actual interfacial tension. In this chapter, monodisperse droplets formed at flat microfluidic Y-junctions were used to quantify the apparent dynamic interfacial tension during (microfluidic) emulsification. Hexadecane droplets were formed in ethanol-water solutions with a range of static interfacial tensions to derive a calibration curve, which was subsequently used to access the dynamic interfacial tension of hexadecane droplets formed in surfactant solutions. For SDS and Synperonic PEF108, various continuous- and disperse-phase (hexadecane) flow rates were studied, and these conditions were linked to interfacial tension effects, which also allowed convective transport of surfactants to be investigated. On the basis of these findings, various strategies for the formation of emulsion droplets can be followed and are discussed.

This chapter is published as: Maartje L.J. Steegmans, Anja Warmerdam, Karin G.P.H. Schroën, Remko M. Boom, Dynamic Interfacial Tension Measurements with Microfluidic Y-junctions, Langmuir, 2009, 25 (17), 9751-9758.

Introduction

In processes such as emulsification, but also foaming, coating, and wetting, surfactant solutions act (per definition) under non-equilibrium conditions [1-3]. Equilibrium is eventually obtained by transfer of surfactants from the bulk toward the (sub)interface and subsequent adsorption to the interface. During this process, the interfacial tension decreases (Gibbs adsorption) until the equilibrium interfacial tension is reached [1]. The rate at which interfacial tension decreases depends on the characteristics of the used surfactant (*e.g.* adsorption and diffusion coefficient), its concentration, and the mass transfer mechanism (*i.e.* diffusion and/or convection).

In the past decade, emulsification with microfluidic devices (microfluidic emulsification) has gained attention as it offers an opportunity to control emulsion droplet size and dispersity [4, 5]. Microfluidic emulsification involves micrometer-sized droplets, fast interface expansion rates, and convective transport of surfactants. Moreover, droplet-formation time [6-8] and surfactant adsorption rates are of the same order of magnitude, and therewith microfluidic emulsification becomes a typical example of a non-equilibrium process. Two early examples of dynamic interfacial tension effects related to emulsification with microdevices are described by van der Graaf *et al.* [9] and Anna and Meyer [10].

In emulsification, surfactant adsorption plays two key roles; first, surfactant adsorption decreases the interfacial tension and, therewith, the droplet formation is facilitated; second, adsorbed surfactant molecules stabilise the emulsion droplets against coalescence [1, 11-14]. During emulsification, the actual interfacial tension can have a value between the interfacial tension of the two pure liquids and the equilibrium interfacial tension. The actual value is of great influence on the resulting droplet size, and therefore, it is important to quantify the dynamic interfacial tension in the sub-millisecond range relevant to microfluidic emulsification [6-8].

Two prevalent tensiometric techniques to measure (dynamic) interfacial tension in the millisecond range at liquid-gaseous surfaces are commercially available,

namely, the oscillating jet and the maximum bubble pressure methods [1, 2]. Nguyen *et al.* [15] and Wang *et al.* [16] measured interfacial tensions at liquid-liquid interfaces with microfluidic T-junctions, but still in the millisecond range. Nguyen *et al.* [15] used the droplet-formation frequency to quantify interfacial tension, and Wang *et al.* [16] used the droplet size to quantify interfacial tension.

In this chapter a new microfluidic tensiometric technique is reported in which monodisperse droplet formation at Y-junctions is used to access the interfacial tension in the sub-millisecond range. This geometry is known for monodisperse microfluidic emulsification [17-19], but here it is used to estimate the (apparent) dynamic interfacial tension at freshly formed highly curved liquid-liquid interfaces subjected to shear and convective surfactant transport.

Experimental

Materials

Anhydrous n-hexadecane with purity of >99 % (no. 296317, Sigma-Aldrich, Steinheim, Germany) was used as the to-be-dispersed-phase. Milli-Q water, 9.0, and 28.0 wt.% ethanol-water mixtures were used as the continuous phases with static interfacial tension. The ethanol-water mixtures were prepared from Milli-Q water and 96 %v/v ethanol (no. 20824, VWR BDH Prolabo, Amsterdam, The Netherlands).

Sodium dodecyl sulfate (SDS) and Synperonic PEF108 were used as surfactants. SDS-solutions with concentrations of 0.03, 0.15, 0.25, 1.5, and 3.0 wt.% were prepared by dissolving SDS (no. L-4390, Sigma-Aldrich, Steinheim, Germany) in Milli-Q water. The SDS concentrations were chosen relative to its CMC of 0.24 wt.% [20, 21]. Synperonic PEF108-solutions with concentrations of 0.025, 0.25, 1.25, and 5.0 wt.% were prepared by dissolving Synperonic PEF108 (a gift from Uniqema, Emmerich, Germany) in Milli-Q water. The Synperonic PEF108 concentrations were chosen relative to its CMC of 2 wt.% [22]. Synperonic PEF108 is a triblock copolymer consisting of a hydrophobic poly(propylene oxide) (PPO) block enclosed

between two hydrophilic poly(ethylene oxide) (PEO) blocks (*i.e.* PEO-PPO-PEO) with a total molecular mass of approximately 14000 Da. These block copolymers are also commercially available under the name Pluronics.

Viscosity

The viscosities of the continuous phases and hexadecane were measured in a rheometer (MCR 301, Anton Paar, Graz, Austria) with a Couette geometry (DG 26.7, Anton Paar, Graz, Austria). Rate sweeps were performed between 1 and 900 s^{-1} to exclude non-Newtonian behaviour. Each of the 18 shear rates was applied for at least 6 s (900 s^{-1}) up to 30 s (1 s^{-1}) and measurement occurred at the end of each period. For each viscosity measurement, forward and backward rate sweeps were performed in duplicate at a controlled temperature of 23 °C (see Table 1).

Table 1: Viscosity η, and interfacial tension with hexadecane $\gamma_{hexadecane}$ of Milli-Q water, ethanol-water mixtures, SDS-solutions, Synperonic PEF108-solutions, and hexadecane at a controlled temperature of 23 °C.

sample	η [mPa·s]	$\gamma_{hexadecane}$ [mN·m^{-1}]
Milli-Q water	1.0	41
9.0 wt.% ethanol-water	1.5	27
28.0 wt.% ethanol-water	2.5	15
0.03 wt.% SDS-solution	1.0	27[a]
0.15 wt.% SDS-solution	1.0	13[a]
0.25 wt.% SDS-solution	1.0	9[a]
1.5 wt.% SDS-solution	1.2	8[a]
3.0 wt.% SDS-solution	1.3	8[a]
0.025 wt.% Synperonic PEF108-solution	1.0	11[a]
0.25 wt.% Synperonic PEF108-solution	1.1	6[a]
1.25 wt.% Synperonic PEF108-solution	1.4	5[a]
5.0 wt.% Synperonic PEF108-solution	3.0	5[a]
hexadecane	3.5	-

[a] Equilibrium interfacial tension.

Interfacial tension

The static interfacial tensions at the hexadecane/ethanol-water interfaces and the equilibrium interfacial tensions at the hexadecane/surfactant-solution interfaces were measured using a dynamic drop tensiometer (ADT, ITCONCEPT, Longessaigne, France) [23] (see Table 1). A hexadecane droplet of 3, 5, or 10 μL was used depending on the (equilibrium) interfacial tension; to prevent premature droplet detachment, the droplet volume was decreased with decreasing (equilibrium) interfacial tension. The hexadecane droplet was formed at the tip of a U-shaped needle positioned in a cuvette with the continuous phase. The measurement started 1 up to 2 s after droplet formation and took 1200 or 20000 s (the latter for the Synperonic PEF108-solutions). The interfacial tension was determined by droplet shape analysis as described by Benjamins *et al.* [23]. Each measurement was performed at least in duplicate at a controlled temperature of 23 °C. The samples were measured in order of increasing concentration, and after each concentration, the cuvette and the needle were rinsed extensively with Milli-Q water. Between the measurements with ethanol, SDS, and Synperonic PEF108, the cuvette and the needle were rinsed with hot tap water, cleaned with chloroform, and successively rinsed with cold tap water and Milli-Q water.

Experimental setup

Microfluidic Y-junction device

Chemically etched borosilicate glass (flat) microchannel Y-junctions (Micronit Microfluidics BV, Enschede, The Netherlands) were used as tensiometric devices (for further details see Steegmans *et al.* [19]).

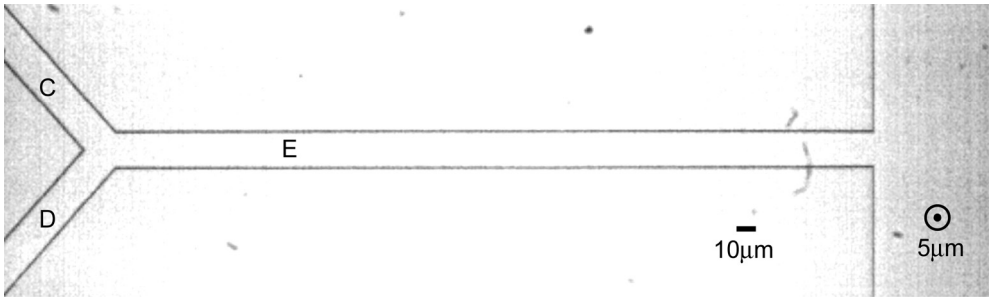

Figure 1: Picture of the Y-junction with an angle of 97° between channel C and D.

Figure 1 shows a picture of the Y-junction, which has channel widths of approximately 18 µm (Table 2 shows the exact channel widths) and a uniform depth of 5 µm. The continuous phase enters the Y-junction via channel C, whereas hexadecane enters via channel D. The angle between channels C and D is 97°. At the Y-junction, both phases meet and hexadecane droplets are formed (see Figure 2), which are transported through channel E toward the collecting area. Due to the shallowness of the channels, the formed droplets are actually disc-shaped in the channel and the collecting area when the droplet size is larger than the channel depth.

Table 2: Width of the continuous-phase w_c, hexadecane w_D, and downstream channel w_E for the three studied microfluidic Y-junction devices. The values represent the 95 % confidence interval (average ± 1.96·standard deviation).

device	w_c [µm]	w_D [µm]	w_E [µm]
1	18.0 ± 0.5	18.2 ± 0.5	18.1 ± 0.5
2	17.9 ± 0.5	18.5 ± 0.5	18.2 ± 0.5
3	18.1 ± 0.5	18.2 ± 0.5	18.2 ± 0.5

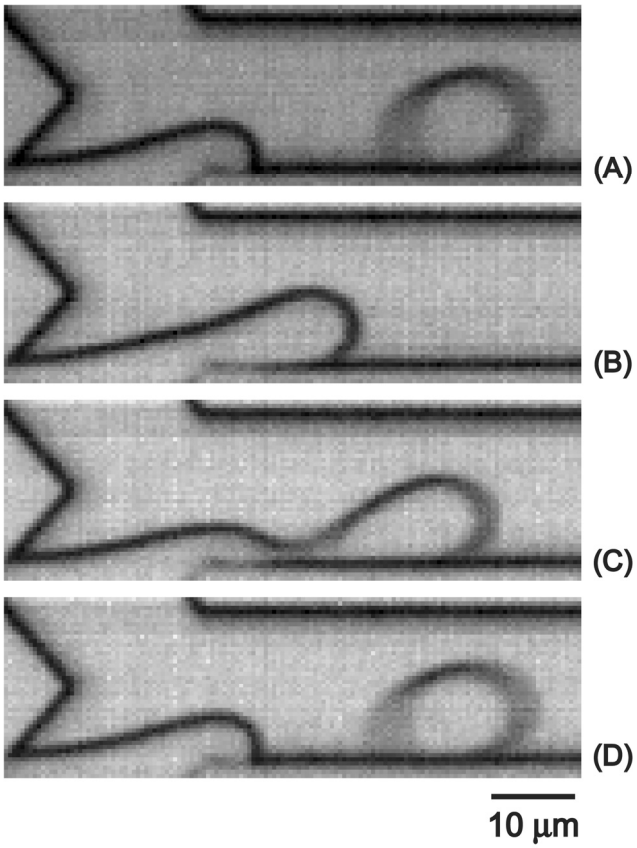

Figure 2: Various stages during droplet formation of hexadecane-in-9.0 wt.% ethanol-water with an ethanol-water flow rate of $1.3 \cdot 10^{-1}$ ($\pm$ $5.4 \cdot 10^{-3}$) mL·h^{-1} and a hexadecane flow rate of $5.4 \cdot 10^{-3}$ ($\pm$ $8.1 \cdot 10^{-4}$) mL·h^{-1}. (A) t = 0 s, (B) t = 0.30 ms, (C) t = 0.42 ms, and (D) t = 0.44 ms. All intervals given in this chapter for the continuous-phase and hexadecane flow rate are derived from image analysis assuming a maximal experimental error of one pixel or one frame.

Droplet-formation experiments

The Y-junction device was operated in the appropriate holder (no. 4515, Micronit Microfluidics BV, Enschede, The Netherlands). The continuous phase and hexadecane entered the device via two separate fused silica capillaries of approximately 35 cm length with an inner diameter of 150 µm (Polymicro Technologies, Phoenix, USA) and a 0.5 µm filter (Upchurch Scientific, Oak Harbor,

USA) halfway. Each fused silica capillary was connected to a 2.5 mL stainless steel Swagelock syringe using a 1/16" Swagelock connector (Alltech, Breda, The Netherlands), 8 cm PEEK tubing with an inner diameter of 1.6 mm (Alltech, Breda, The Netherlands), and a PEEK union assemblage with a capillary sleeve (Upchurch Scientific, Oak Harbor, USA).

The flow rates of the continuous phase and hexadecane were controlled with syringe pumps (PHD4400 (continuous phases) and PHD22/2000 (hexadecane), Harvard Apparatus, Holliston, USA). At applied continuous-phase flow rates ranging from 0.10 to 0.35 $mL \cdot h^{-1}$ and applied hexadecane flow rates ranging from $3.0 \cdot 10^{-3}$ to 0.05 $mL \cdot h^{-1}$ droplets were formed at the Y-junction. After the flow rate(s) had been changed, the droplet formation process was allowed to assume steady state for at least 2 min.

Droplet formation was recorded using a high-speed camera (MotionPro HS-4, Redlake, Tallahassee, USA) connected to an inverted transmitted light microscope (Axiovert 200, Carl Zeiss, Sliedrecht, The Netherlands). The formation of 25 subsequent hexadecane droplets was recorded using (approximately) 20 frames per droplet, which corresponds to frame rates between 8000 and 73502 s^{-1}. The gain and the exposure time were chosen such that the image quality was optimal.

Image Analysis

Droplet size

The droplet size was automatically determined using a custom-written script based on the DIPimage toolbox operating in Matlab 7.0.1. The area of each disc-shaped hexadecane droplet was determined to be the average over three subsequent frames. Ten subsequent droplets were measured in this way; the droplet area used for further analysis was the average of these ten. The 95 % confidence interval was calculated as the average ± 1.96·standard deviation.

Flow rates at the Y-junction

The actual continuous-phase flow rate ϕ_c at the Y-junction was determined from the velocity of the droplets in the downstream channel, assuming that the droplet velocity was equal to the velocity of the continuous phase. Using Image-Pro Plus 4.5.0.29, the length between the downstream corners of the Y-junction and the left side of the hexadecane droplet was manually determined in the third frame after detachment and in the frame just before the droplet moved outside the viewing area. The velocity was then calculated from the difference in position divided by the time interval between the two frames. Multiplying this velocity with the cross-sectional area of the downstream channel resulted in the actual continuous-phase flow rate.

The actual hexadecane flow rate ϕ_d at the Y-junction was calculated from the droplet volume V and the droplet-formation frequency f:

$$\phi_d = V \cdot f \qquad (m^3 \cdot s^{-1}) \quad (1).$$

The droplet volume was calculated from the droplet area by assuming that the droplets were disc-shaped with rounded edges with a curvature in the order of the depth of the channel [19].

The actual continuous-phase flow rates at the Y-junction varied from $6.7 \cdot 10^{-2}$ to 0.45 $mL \cdot h^{-1}$, and the hexadecane flow rates varied from $3.8 \cdot 10^{-4}$ to $6.5 \cdot 10^{-3}$ $mL \cdot h^{-1}$; this is in contrast to the applied continuous-phase flow rates between 0.10 and 0.35 $mL \cdot h^{-1}$ and the applied hexadecane flow rates between $3.0 \cdot 10^{-3}$ and 0.05 $mL \cdot h^{-1}$. The actual flow rates at the Y-junction were found to differ from the (applied) flow rates set on the pump, probably due to a significant pressure drop in the microfluidic device (in the order of tens of bars); therefore, the actual (calculated) flow rates are used.

Statistical analysis

The calibration curve was determined using the least squares method. The standard deviations of the parameters were estimated as the product of the square

root of the residual mean square and the square root of the variance of the parameter.

Results and discussion

Emulsion droplet size

Emulsion droplets produced at microfluidic Y-junctions were monodisperse, as shown in Figure 3; the polydispersity index (standard deviation to average droplet size ratio) of these droplets was consistently below 1 % for ethanol-water mixtures, SDS-solutions, and Synperonic PEF108-solutions. This implies that the conditions in the microfluidic devices can be controlled precisely. It is therefore reasonable to assume that microfluidic Y-junctions can be used for accurate tensiometric measurements.

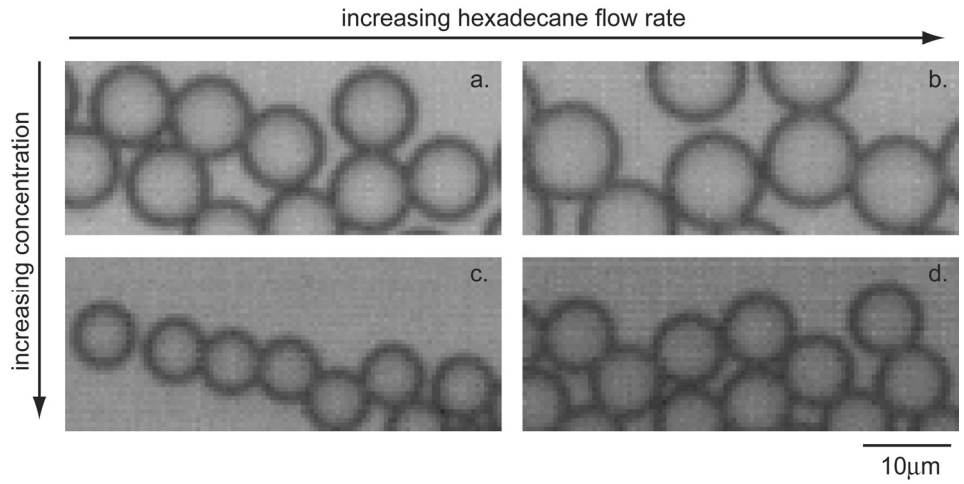

Figure 3: Monodisperse (disc-shaped) hexadecane droplets in the collecting area produced at equal continuous-phase flow rate of 0.3 (± $3 \cdot 10^{-2}$) $mL \cdot h^{-1}$ and further conditions as indicated in Table 3.

Table 3: The droplet area A (represented with its 95 % confidence interval) and apparent dynamic interfacial tension γ (as determined with the method explained later) at droplet detachment are a function of the SDS concentration and the hexadecane flow rate ϕ_d for the pictures shown in Figure 3.

Picture	SDS concentration [wt.%]	ϕ_d [mL·h^{-1}]	A [μm^2]	γ [mN·m^{-1}]
a.	0.25	$1.6 \cdot 10^{-3}$ ($\pm 4 \cdot 10^{-5}$)	80 ± 1	21
b.	0.25	$3.2 \cdot 10^{-3}$ ($\pm 7 \cdot 10^{-5}$)	105 ± 2	29
c.	3.0	$1.6 \cdot 10^{-3}$ ($\pm 6 \cdot 10^{-5}$)	45 ± 1	14
d.	3.0	$3.3 \cdot 10^{-3}$ ($\pm 2 \cdot 10^{-4}$)	59 ± 3	19

Figure 3 shows that droplet size increases with increasing hexadecane flow rate and increasing SDS concentration, as will be discussed under section 'Effect of disperse-phase flow rate and SDS concentration'. How the interfacial tension was determined from droplet size is explained in the following sections; for clarity reasons, the term apparent dynamic interfacial tension will be used if referred to this value.

Calibration curve

The microfluidic tensiometric technique discussed in this chapter is based on a calibration curve of hexadecane/ethanol-water systems with a range of static interfacial tensions. In Chapter 3, it was shown that in Y-junctions, the main force keeping the droplet attached to the hexadecane bulk is proportional to the interfacial tension, and a droplet detaches when this interfacial tension force is exceeded by a shear force exerted by the continuous phase. As a result, the droplet size is related to both the interfacial tension and the velocity of the continuous phase, which are incorporated in the capillary number of the continuous phase Ca_c:

$$Ca_c = \frac{\eta_c v_c}{\gamma} \qquad (-) \qquad (2),$$

where η_c is the dynamic viscosity of the continuous phase, v_c is the velocity of the continuous phase, and γ is the interfacial tension.

The calibration curve, shown in Figure 4, relates the droplet area of (disc-shaped) hexadecane droplets formed in water and ethanol-water solutions to the capillary number of the continuous phase. This graph implies that droplet area increases with decreasing capillary number, therewith indicating that droplet size increases with increasing interfacial tension and decreasing continuous-phase velocity, as expected.

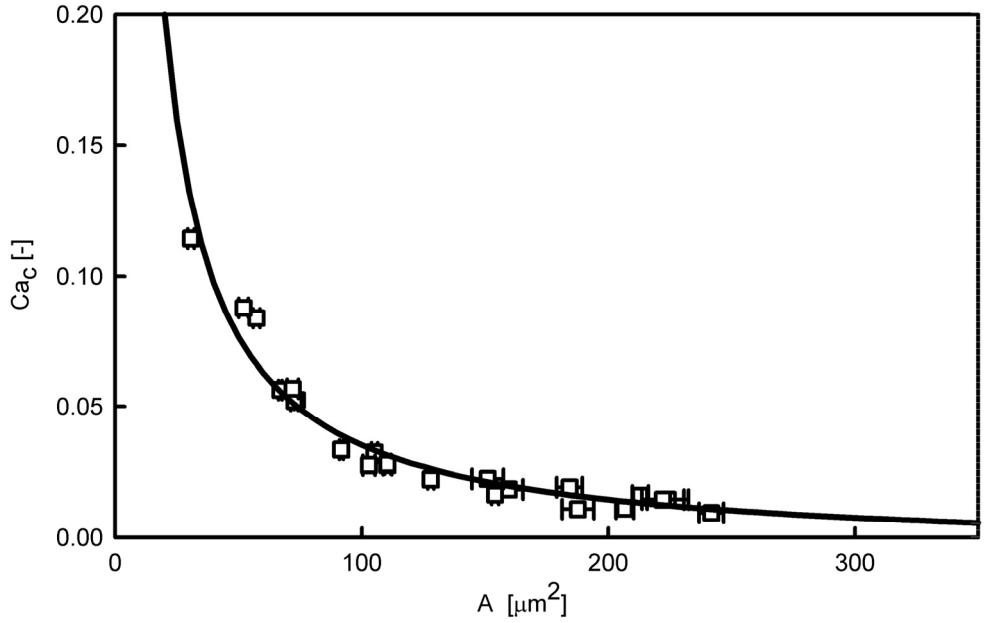

Figure 4: Droplet area *A* as function of capillary number of the continuous phase Ca_c. The squares (□) represent the experimental data, and the solid line is the calibration curve derived from these data with the least squares method. The error-bars represent the 95 % confidence interval of the droplet area.

The following purely empirical relationship was selected through statistical analysis (without implying any physical meaning):

$$Ca_c = a + \frac{b}{A} \quad (-) \quad (3),$$

where A is the droplet area, and a and b are parameters with a 95 % confidence interval of $-6.23 \cdot 10^{-3} \pm 5.22 \cdot 10^{-3}$ and 4.15 ± 0.44 μm², respectively. In this chapter, the calibration curve is only used to estimate apparent dynamic interfacial tension in the experimental size range, that is, from 31 to 242 μm², but most probably the range for which the calibration curve can be used is wider.

Apparent dynamic interfacial tension in hexadecane/SDS-solutions

The calibration curve was used to convert droplet area to apparent dynamic interfacial tensions at fast expanding hexadecane/SDS-water interfaces. In our system, the expansion rate is influenced by both continuous- and disperse-phase flow rate, and values between 250 and 2500 s^{-1} were reached for hexadecane/SDS-solutions.

Figure 5 shows that the apparent dynamic interfacial tension at the moment of droplet detachment, as determined with the calibration curve, is generally between the interfacial tension of the pure liquids and the equilibrium interfacial tension. Despite the high expansion rate and the sub-millisecond adsorption time, SDS monomers are fast enough to adsorb to the interface during emulsification, but the interface is not yet fully covered. This is also the case for SDS concentrations above its CMC (viz 0.25, 1.5, and 3.0 wt.%); which was not expected from adsorption times in the order of milliseconds reported in literature [16]. In (microfluidic) emulsification literature, it is common practice to use the equilibrium interfacial tension, but, as shown here, this may lead to substantial underestimation of the actual value of the interfacial tension.

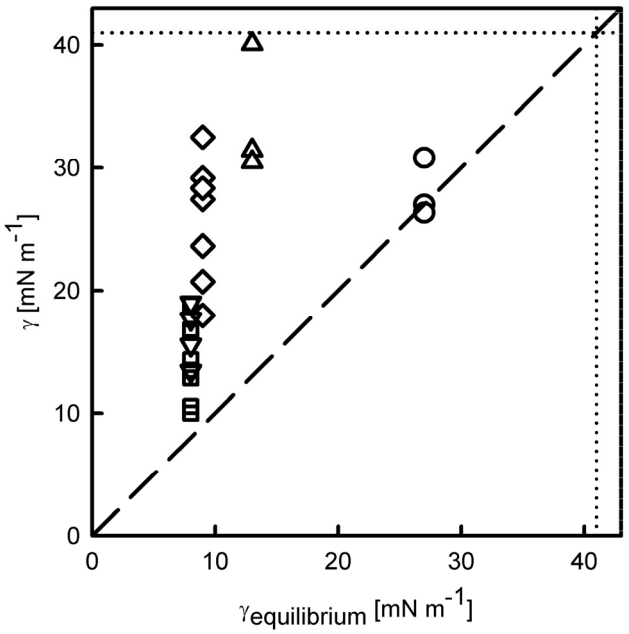

Figure 5: Apparent dynamic interfacial tension γ (determined with the calibration curve) as a function of equilibrium interfacial tension $\gamma_{equilibrium}$ (determined with dynamic drop tensiometry (see Table 1)) for hexadecane with 0.03 (O), 0.15 (△), 0.25 (◊), 1.5 (▽), and 3.0 wt.% SDS-solution (□) at various continuous-phase (0.14 to 0.45 mL·h^{-1}) and hexadecane flow rates ($3.8 \cdot 10^{-4}$ to $4.7 \cdot 10^{-3}$ mL·h^{-1}) (see Appendix B for the flow rates per data point). The dashed line indicates the line of parity, and the dotted lines indicate the interfacial tension between hexadecane and pure water.

Different conditions may lead to the same interfacial tension. To illustrate this, the experimental data points from a hexadecane/0.03 wt.% and a hexadecane/0.25 wt.% SDS–solution were compared. The continuous-phase flow rate is the same for both experiments, and the size of the droplets is virtually the same, but Table 3 shows that to obtain the same interfacial tension, the hexadecane flow rate is considerably higher for the highest SDS concentration.

Table 4: Continuous-phase flow rate ϕ_c and hexadecane flow rate ϕ_d for two SDS concentrations with comparable droplet areas A (represented with its 95 % confidence interval) and apparent dynamic interfacial tensions γ.

SDS-concentration [wt.%]	A [μm^2]	γ [$mN \cdot m^{-1}$]	ϕ_c [$mL \cdot h^{-1}$]	ϕ_d [$mL \cdot h^{-1}$]
0.03	152 ± 2	30.8	$0.21 \pm 2 \cdot 10^{-2}$	$1.6 \cdot 10^{-3} \pm 3 \cdot 10^{-5}$
0.25	157 ± 4	32.5	$0.21 \pm 1 \cdot 10^{-2}$	$4.7 \cdot 10^{-3} \pm 2 \cdot 10^{-4}$

When an interface is not fully covered and the surfactant monomers are non-uniformly distributed along the interface (which will be the case in our system), interfacial tension gradients can arise, leading to Marangoni stresses [24]. Despite the fact that our interfaces are usually partly covered with SDS monomers, we suspect little or no Marangoni effects during droplet formation and detachment as Marangoni flow is too slow. Marangoni flow is maximally roughly 1 $\mu m \cdot ms^{-1}$ [25], whereas the continuous-phase flow rate over the droplets is typically in the order of 1000 $\mu m \cdot ms^{-1}$ and the emulsion droplets are generally formed in less than a millisecond and typical length scales are in the order of micrometers.

Effect of disperse-phase flow rate and SDS concentration

Since the flow rates have to be determined by image analysis, it is not straightforward to show the effect of isolated parameters. Despite this, a selection of data that illustrate various effects was found.

Figure 6a shows that the apparent dynamic interfacial tension increases with increasing hexadecane flow rate at constant SDS concentration and continuous-phase flow rate. As expected, at increasing hexadecane flow rate the interface becomes less occupied with SDS monomers, resulting in higher interfacial tensions at equal droplet formation time. As shown in Figure 6b, where the continuous-phase flow rate was slightly less constant than in Figure 6a, the apparent dynamic interfacial tension is a function of the SDS concentration, albeit that at high SDS concentration, the dependency on disperse-phase flow rate seems less strong than at low SDS concentrations.

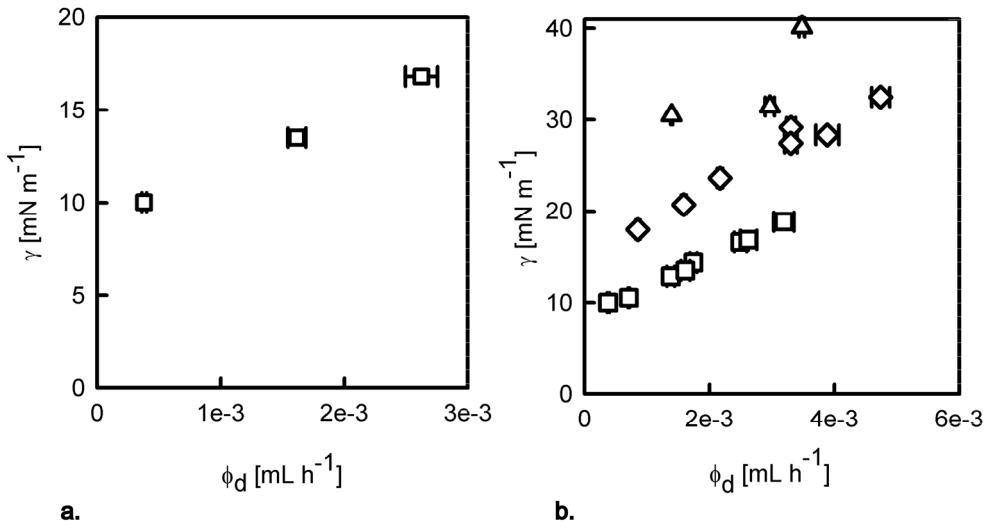

Figure 6: Apparent dynamic interfacial tension γ as function of hexadecane flow rate ϕ_d for a. 3.0 wt.% SDS-solution (□) at a constant continuous-phase flow rate of 0.23 mL·h^{-1}, and for b. 0.15 (△), 0.25 (◊), and 3.0 wt.% SDS-solution (□) at continuous-phase flow rates varying between 0.14 and 0.45 mL·h^{-1} (see Appendix B for the flow rates per data point).

SDS transport

In our microfluidic Y-junctions, dynamic interfacial tension is determined by a combination of diffusive and convective transport of surfactants, in the form of monomers or micelles, from the bulk to the so-called subinterface (*i.e.* an imaginary continuous-phase layer adjacent to the interface [2]) and subsequent adsorption from this subinterface to the interface. Assuming that the latter step is not rate limiting for the decrease in interfacial tension, we attempted to quantify the contribution of convection to the surfactant transport to a hexadecane interface for 0.25 and 1.5 wt.% SDS-solution.

No dynamic interfacial tension data are available for solely diffusive SDS transport to a hexadecane interface expanding at several hundreds to thousands per second, like in our Y-junctions. Therefore, data obtained with the bursting membrane method for a vegetable oil/2 wt.% SDS-solution interface [26] were used. For these

data, the expansion rate could be assumed to be proportional to the inverse time †. As a result, the typical dynamic interfacial tension versus time curve could be converted to a dynamic interfacial tension versus expansion rate curve (*i.e.* inverse time curve; Figure 7a.).

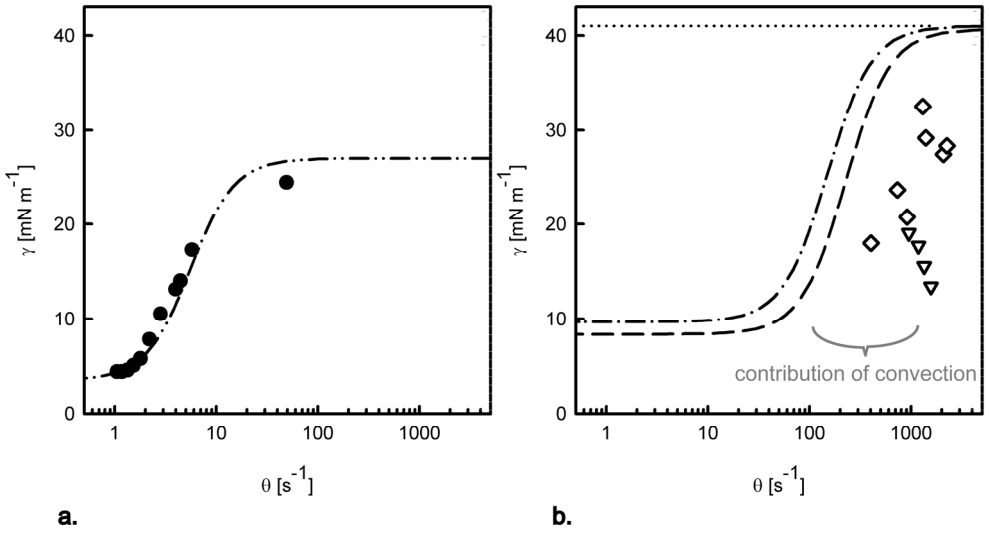

Figure 7: Apparent dynamic interfacial tension γ versus expansion rate θ for a. vegetable oil/2 wt.% SDS-solution data obtained by Schröder *et. al.* [26] (•) with its fitted curve [26] (dashed-dotted-dotted line) and b. modified curves for hexadecane/0.25 (dashed-dotted line) and 1.5 wt.% SDS-solution (dashed line) with (experimental) hexadecane/0.25 (◊) and 1.5 wt.% SDS-solution (▽) data obtained with our microfluidic Y-junctions. The dotted line indicates the interfacial tension between hexadecane and pure water.

Due to the limitation in available literature data, it was assumed that the trend of the dynamic interfacial tension as a function of expansion rate for a system with solely diffusion is comparable for vegetable oil/SDS-solution and for

† Expansion rate θ is defined as: $\theta = d\ln A/dt$ [27], where A is the droplet area and t is the time. In the bursting membrane method surfactants can only adsorb to the interface after the membrane is broken [12], therefore it was assumed that there was no interface at $t = 0$ and $\theta = 1/t$.

hexadecane/SDS-solution interfaces above the CMC. On this basis, the vegetable oil/2 wt.% SDS-solution curve was modified to describe a hexadecane/0.25 and 1.5 wt.% SDS-solution interface using the interfacial tension between hexadecane and pure water and the equilibrium interfacial tension as measured with dynamic drop tensiometry (see Figure 7b.) as extremes. When the trend of these modified curves was compared to literature data from air/SDS-solutions with comparable SDS concentration [28], a similar trend was observed, which suggests that these curves are reasonable.

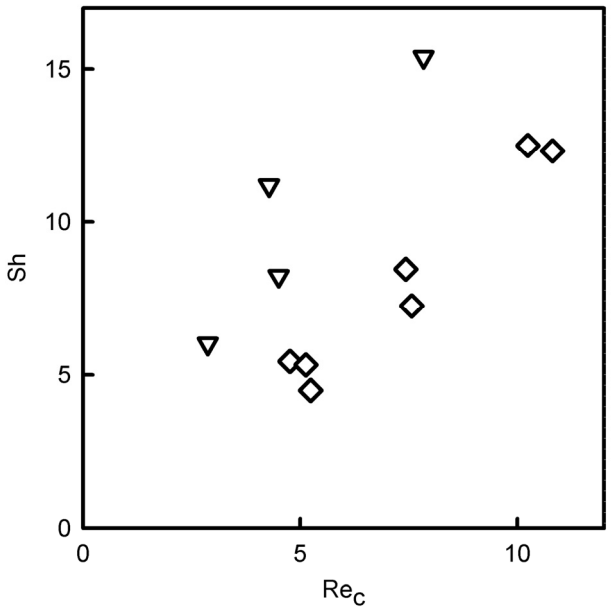

Figure 8: Estimation of the Sherwood number *Sh* as function of the Reynolds number of the continuous phase Re_c [‡] at a microfluidic Y-junction for hexadecane/0.25 (◊) and 1.5 wt.% (▽) SDS-solution interfaces at expansion rates varying between 404 and 2251 s^{-1}.

[‡] The Reynolds number of the continuous phase Re_c was calculated: $Re_c = (\rho_c \upsilon_c D_{H,E})/\eta_c$, where $D_{H,E}$ is the hydraulic diameter of the downstream channel (see Figure 1) and ρ_c, υ_c, and η_c are the density, velocity, and dynamic viscosity of the continuous phase, respectively.

In literature, the Sherwood number *Sh* is defined as the ratio between the total and diffusive mass transport [29]. To give a semi-quantitative impression of the extent to which surfactant transport is dominated by convection in microfluidic Y-junctions, *Sh* was used. It was defined as the ratio between the expansion rate determined in our Y-junction system (*i.e.* the open diamonds and triangles in Figure 7b.) and the expansion rate read for a solely diffusive system with the same interfacial tension and hexadecane/SDS-solution concentration from the curves in Figure 7b.

Figure 8 suggests that convection dominates surfactant transport in microfluidic Y-junctions and that its contribution increases with increasing SDS concentration and increasing Reynolds number of the continuous phase (seemingly linearly in the observed range). In principle, this graph could be the basis for estimating droplet size for certain process conditions and SDS concentration by inverting the approach shown so far. However, due to the large number of assumptions needed to derive Figure 8, we currently perceive this as the proverbial bridge too far.

Our approach gives an impression of the importance of convection relative to diffusion and based on our estimation convection seems to be very significant. Therefore, when an interfacial tension value is based on diffusion behaviour only, presumably its value is highly overestimated. Especially for emulsification, this is not a desired situation, since the droplet size is directly linked to the interfacial tension and the droplets would become smaller than intended.

Discussion and outlook

Our calibration curve can, in principle, be used to estimate the apparent dynamic interfacial tension for any surfactant or surface-active polymer, and from this, differences in fast interfacial behaviour can be investigated. To show the versatility of the approach discussed in this chapter, a macromolecular surfactant, Synperonic PEF108, was chosen, which is expected to diffuse much more slowly than SDS. The diffusion coefficient for Synperonic PEF108 is roughly $2.7 \cdot 10^{-12}$ $m^2 \cdot s^{-1}$ (see Appendix A), in contrast to $1.4 \cdot 10^{-10}$ $m^2 \cdot s^{-1}$ for SDS monomers [30] and $8.7 \cdot 10^{-11}$ $m^2 \cdot s^{-1}$ for SDS micelles [31].

Figure 9 shows that also in the case of a macromolecular surfactant, apparent dynamic interfacial tension effects are significant, albeit that the interfacial tension is much closer to that of the pure liquids than was found for SDS. Nonetheless, the surfactant does reach the interface, and this is probably due to the fact that surfactant transport is dominated by convection, as previously illustrated for SDS. Besides, Synperonic PEF108 molecules are expected to need time to change configuration at the interface, that is, obtain a U-shape (*i.e.* form a polymer brush) [22], which may delay adsorption of other Synperonic PEF108 molecules and therewith the decrease in interfacial tension.

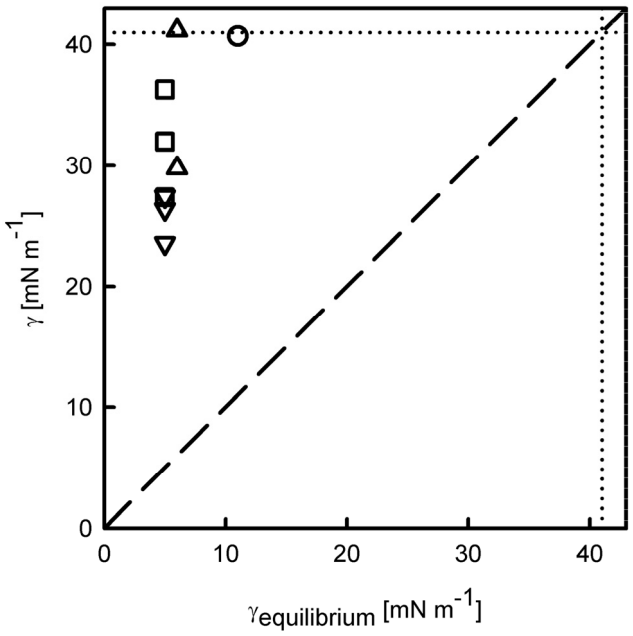

Figure 9: Apparent dynamic interfacial tension γ (determined with the calibration curve) as function of equilibrium interfacial tension $\gamma_{equilibrium}$ (determined with dynamic drop tensiometry (see Table 1)) for hexadecane with 0.025 (O), 0.25 (△), 1.25 (□), and 5.0 wt.% (▽) Synperonic PEF108-solution at various continuous-phase (0.10 to 0.38 mL·h^{-1}) and hexadecane flow rates (6.8·10^{-4} to 6.1·10^{-3} mL·h^{-1}) (see Appendix B for the flow rates per data point). The dashed line indicates the line of parity, and the dotted lines indicate the interfacial tension between hexadecane and pure water.

In summary, the tensiometric technique described in this chapter can be used to estimate apparent dynamic interfacial tension in the sub-millisecond time range at a liquid-liquid interface subjected to convection. In emulsification with microfluidic Y-junctions, this apparent dynamic interfacial tension is an important parameter as it determines the size of the emulsion droplets. Therefore, through the calibration curve presented here, the processing conditions relating to a specific interfacial tension, and therewith, droplet size can be determined. Interfacial tension can be tuned by the disperse-phase flow rate, but always in combination with the surfactant and its concentration and the flow rate of the continuous phase.

The lowest interfacial tensions and, therewith, the smallest emulsion droplet sizes are reached at low disperse-phase flow rates and/or high surfactant concentrations. The latter is common practice in emulsification, but low disperse-phase flow rates seem to be less practical, as, ideally, the oil flow rate should be as high as possible for acceptable productivity. At high disperse-phase flow rates the effects of higher interfacial tension can be counteracted by a high continuous-phase flow rate, but this will influence the volume fraction of the dispersed phase.

For production of larger droplets, it is advisable to work at high disperse-phase flow rates for maximal productivity, even though the interface may be hardly covered by surfactants at detachment. By avoiding contact between the emulsion droplets, one can prevent coalescence. In our microfluidic Y-junctions, this is facilitated by the horizontal transport channel (channel *E* in Figure 1), which stretches the time for adsorption up to several times the droplet-formation time (depending on the continuous-phase velocity). This finding is in accordance with the findings of Baret *et al.* [32], who very recently came to the same conclusion for flow-focusing devices. They also described that surfactant adsorption after droplet formation is diffusion dominated, which may be used as a guideline in the design of the length of the transport channel. Therewith, monodispersity can be maintained at high production rates without the need for using excessive amounts of surfactants.

Conclusion

A new microfluidic tensiometric technique is described to estimate (apparent) dynamic interfacial tension in systems subjected to significant convection. Our technique uses the droplet size of monodisperse emulsion droplets formed at a microfluidic Y-junction to estimate interfacial tension at sub-millisecond timescales. A calibration curve was derived for a model system with static interfacial tension: hexadecane droplets in ethanol-water mixtures. With this calibration curve, the apparent dynamic interfacial tension in surfactant systems, namely SDS and Synperonic PEF108, was estimated. Besides, it was shown that surfactant transport is dominated by convection.

Acknowledgements

The authors wish to thank Michael van Ginkel for writing the droplet analysis script and MicroNed for supporting this research.

Appendix A

The gyration radius R_g of Synperonic PEF108 was estimated by assuming an ideal chain with constant bond angles and equal length of the ethylene oxide and propylene oxide segments with the following equation:

$$R_g = \left(\frac{1}{6}\right)^{\frac{1}{2}} \left(\frac{1-\cos\alpha}{1+\cos\alpha}\right)^{\frac{1}{2}} l N^{\frac{1}{2}} \quad \text{(m)} \qquad \text{(A.1)},$$

where α is the (constant) bond angle, l is the segment length, and N is the sum of the number of PEO and PPO segments (see Table A for their values).

Table A: Quantities of Synperonic PEF108 obtained from the literature.

Quantity	Value	Source
α	110°	[33]
l	3.64 Å	[33]
N	314	[22]
N_{PPO}	50	[22]
N_{PEO}	2 x 132	[22]

Subsequently, the diffusion coefficient D was estimated assuming a spherical coil with hydraulic radius R_h:

$$D = \frac{k_B T}{6\pi\eta_c R_h} = \frac{k_B T}{4\pi\eta_c R_g} \quad (\mathrm{m^2 \cdot s^{-1}}) \quad \text{(A.2)},$$

where k_B is the Boltzmann constant ($1.38 \cdot 10^{-23}$ $\mathrm{J \cdot K^{-1}}$), T is the absolute temperature, and η_c is the dynamic viscosity of the continuous phase. For a temperature of 23 °C, a diffusion coefficient of $2.7 \cdot 10^{-12}$ $\mathrm{m^2 \cdot s^{-1}}$ was estimated for Synperonic PEF108 in Milli-Q water.

Appendix B

Table B.1: Disperse- and continuous-phase flow rates ϕ_d and ϕ_c, SDS concentration, and apparent dynamic interfacial tension γ for the data points shown in Figure 5 and 6b.

SDS concentration [wt.%]	γ [mN·m^{-1}]	ϕ_d [mL·h^{-1}]	ϕ_c [mL·h^{-1}]
0.03	27	1.8·10^{-3}	0.16
0.03	31	1.6·10^{-3}	0.21
0.03	26	8.6·10^{-4}	0.17
0.15	32	3.0·10^{-3}	0.19
0.15	31	1.4·10^{-3}	0.19
0.15	40	3.5·10^{-3}	0.36
0.25	24	2.2·10^{-3}	0.20
0.25	29	3.3·10^{-3}	0.32
0.25	21	1.6·10^{-3}	0.31
0.25	27	3.3·10^{-3}	0.45
0.25	28	3.9·10^{-3}	0.43
0.25	18	8.6·10^{-4}	0.22
0.25	33	4.7·10^{-3}	0.21
1.5	16	2.1·10^{-3}	0.21
1.5	18	2.0·10^{-3}	0.23
1.5	13	1.1·10^{-3}	0.39
1.5	19	2.6·10^{-3}	0.14
3.0	13	1.4·10^{-3}	0.15
3.0	11	7.1·10^{-4}	0.15
3.0	17	2.5·10^{-3}	0.14
3.0	19	3.2·10^{-3}	0.31
3.0	14	1.7·10^{-3}	0.31
3.0	10	3.8·10^{-4}	0.23
3.0	14	1.6·10^{-3}	0.22
3.0	17	2.6·10^{-3}	0.23

Table B.2: Disperse- and continuous-phase flow rates ϕ_d and ϕ_c, Synperonic PEF108 concentration, and apparent dynamic interfacial tension γ for the data points shown in Figure 9.

Synperonic PEF108 concentration [wt.%]	γ [mN·m^{-1}]	ϕ_d [mL·h^{-1}]	ϕ_c [mL·h^{-1}]
0.025	41	$3.3 \cdot 10^{-3}$	0.37
0.25	41	$5.8 \cdot 10^{-3}$	0.15
0.25	30	$3.2 \cdot 10^{-3}$	0.36
1.25	36	$6.1 \cdot 10^{-3}$	0.15
1.25	32	$4.3 \cdot 10^{-4}$	0.22
1.25	32	$5.0 \cdot 10^{-3}$	0.38
1.25	27	$3.2 \cdot 10^{-3}$	0.11
5.0	24	$6.8 \cdot 10^{-4}$	0.10
5.0	26	$1.6 \cdot 10^{-3}$	0.10
5.0	27	$1.2 \cdot 10^{-3}$	0.14

References

1. T. Battal, C. D. Bain, M. Weiss and R. C. Darton, *Journal of Colloid and Interface Science*, 2003, **263**, 250-260.
2. R. Miller, P. Joos and V. B. Fainerman, *Advances in Colloid and Interface Science*, 1994, **49**, 249-302.
3. M. van den Tempel and E. H. Lucassen-Reynders, *Advances in Colloid and Interface Science*, 1983, **18**, 281-301.
4. T. Nisisako and T. Torii, *Lab On A Chip*, 2008, **8**, 287-293.
5. I. Kobayashi, S. Hirose, T. Katoh, Y. P. Zhang, K. Uemura and M. Nakajima, *Microsystem Technologies-Micro-and Nanosystems-Information Storage and Processing Systems*, 2008, **14**, 1349-1357.
6. L. Yobas, S. Martens, W. L. Ong and N. Ranganathan, *Lab on a Chip*, 2006, **6**, 1073-1079.
7. I. Kobayashi, K. Uemura and M. Nakajima, *Colloids and Surfaces A-Physicochemical and Engineering Aspects*, 2007, **296**, 285-289.
8. T. Nisisako, T. Torii and T. Higuchi, *Lab On A Chip*, 2002, **2**, 24-26.

9. S. v. d. Graaf, M. L. J. Steegmans, R. G. M. v. d. Sman, C. G. P. H. Schroën and R. M. Boom, *Colloids and Surfaces A-Physicochemical and Engineering Aspects*, 2005, **266**, 106-116.
10. S. L. Anna and H. C. Mayer, *Physics of Fluids*, 2006, **18**.
11. S. M. Joscelyne and G. Trägårdh, *Journal of Membrane Science*, 2000, **169**, 107-117.
12. M. Stang, H. Karbstein and H. Schubert, *Chemical Engineering and Processing*, 1994, **33**, 307-311.
13. J. Tong, M. Nakajima, H. Nabetani and Y. Kikuchi, *Journal of Surfactants and Detergents*, 2000, **3**, 285-293.
14. G. Urbina-Villalba, *Langmuir*, 2004, **20**, 3872-3881.
15. N. T. Nguyen, S. Lassemono, F. A. Chollet and C. Yang, *Ieee Sensors Journal*, 2007, **7**, 692-697.
16. K. Wang, Y. C. Lu, J. H. Xu and G. S. Luo, *Langmuir*, 2009, **25**, 2153-2158.
17. A. Kawai, S. Matsumoto, H. Kiriya, T. Oikawa, K. Hara, T. Ohkawa, T. Futami, K. Katayama and K. Nishizawa, *TOSOH Research and Technology Review*, 2003, **47**, 3-9.
18. A. Kubo, H. Shinmori and T. Takeuchi, *Chemistry Letters*, 2006, **35**, 588-589.
19. M. L. J. Steegmans, C. G. P. H. Schroën and R. M. Boom, *Langmuir*, 2009, **25**, 3396-3401.
20. S. v. d. Graaf, C. G. P. H. Schroën and R. M. Boom, *Journal of Membrane Science*, 2005, **251**, 7-15.
21. T. F. Tadros, *Surfactants*, Academic Press, London, 1984.
22. P. Alexandridis, V. Athanassiou, S. Fukuda and T. A. Hatton, *Langmuir*, 1994, **10**, 2604-2612.
23. J. Benjamins, A. Cagna and E. H. Lucassen-Reynders, *Colloids and Surfaces A-Physicochemical and Engineering Aspects*, 1996, **114**, 245-254.
24. W. J. Milliken and L. G. Leal, *Journal of Colloid and Interface Science*, 1994, **166**, 275-285.
25. D. D. Johnson Jr, B. Kang, J. L. Vigorita, A. Amram and E. M. Spain, *Journal of Physical Chemistry A*, 2008, **112**, 9318-9323.

26. V. Schröder, O. Behrend and H. Schubert, *Journal of Colloid and Interface Science*, 1998, **202**, 334-340.
27. V. B. Fainerman, A. V. Makievski and R. Miller, *Colloids and Surfaces a-Physicochemical and Engineering Aspects*, 1994, **87**, 61-75.
28. T. H. Iliev and C. D. Dushkin, *Colloid & Polymer Science*, 1992, **270**, 370-376.
29. L. P. B. M. Janssen and M. M. C. G. Warmoeskerken, *Transport phenomena data companion*, 3rd edn., Delft University Press, Delft, 2001.
30. M. Rayner, *Membrane emulsification: modelling interfacial and geometric effects on droplet size*, Lund University, 2005.
31. R. Piazza and A. Guarino, *Physical Review Letters*, 2002, **88**.
32. J. Baret, F. Kleinschmidt, A. El Harak and A. D. Griffiths, *Langmuir*, 2009.
33. A. I. Toryanik, *Journal of Structural Chemistry*, 1984, **25**, 385-388.

Chapter 7

General discussion

Introduction

The preceding chapters have shown that microfluidic Y-junctions are suitable for monodisperse emulsification. In literature, this is also shown for other shear-driven microfluidic emulsification techniques, viz T-junctions and flow-focusing devices (*i.e.* ψ-junctions). Despite the monodispersity of the produced emulsions, shear-driven microfluidic devices are not yet applied on large scale as mass-parallelisation is needed to obtain industrially relevant production rates [1, 2]. In this chapter, the effect of flow rate(s), monodispersity, energy input, and ease of parallelisation are evaluated to indicate the potential of these techniques for large-scale application. Cross-flow membrane emulsification is used as a benchmark technology as it is already relatively mature and easy to scale up by using larger membranes or positioning several membranes together [3].

Table 1: General comparison of the current status of shear-driven emulsification techniques.

emulsification technique	mono-dispersity[a]	ease of parallelisation[a]	energy input[a,b]
Y-junction	++[c]	-	+[d]
ψ-junction	++[4, 5]	--	+[d]
T-junction	+[1]	-	+[d]
cross-flow membrane emulsification	o[3, 6]	o	o

[a] Membrane emulsification is the benchmark.

[b] Assuming equal channel dimensions for the microfluidic devices.

[c] See Chapter 3, 5, and 6.

[d] A plus indicates that more energy is required.

Table 1 shows a summary of the current status of various aspects relevant to scale up. It is shown that emulsions produced with Y- and ψ-junctions are most monodisperse. With respect to energy input and scale up, currently cross-flow membrane emulsification is expected to exceed the existing shear-driven microfluidic devices due to its relatively low applied pressure and relative ease of scale up [3, 7]. Nevertheless, optimisation of the microchannel lengths and further research on parallelisation may well bring shear-driven microfluidic devices and membranes closer together in future.

In the remainder of this chapter more detailed information is given on the characteristics of emulsification with microfluidic Y-junctions in comparison to other shear-driven emulsification techniques (Table 1 lists these techniques). A separate section is devoted to the dynamic interfacial tension, which is often neglected, but of prime importance for emulsification. The chapter will be concluded with a short outlook, including possible applications.

Detailed comparison of emulsification techniques

Droplet-formation mechanism

Effect of flow rates

In contrast to other shear-driven emulsification techniques, the droplet size in microfluidic Y-junctions is only influenced by the continuous-phase flow rate, which implies that emulsification in Y-junctions is easier to control than in other shear-driven emulsification devices (for further details see Chapter 3 and 5). In contrast, for T-junctions at comparable Reynolds numbers (approximately $0.1 < Re < 10$), the continuous- and disperse-phase flow rate were observed to influence the emulsion droplet size [4]. This difference is expressed in the one-step droplet-formation model suggested for Y-junctions (see Chapter 3 and 5) and the two-step model suggested for T-junctions (see Chapter 2); only the second step is influenced by the disperse-phase flow rate. Similar effects were reported for membrane emulsification [3], which is not surprising as T-junctions are used as a model system

for membrane emulsification [8]. Also in flow-focusing devices the droplet size is determined by both flow rates [9]. The only other microfluidic emulsification technique in which only one phase needs to be controlled, straight-through-microchannel emulsification, is not using shear to form droplets, as droplets are formed spontaneous when the incipient droplet changes from a flat into a spherical shape [10]. As this droplet formation mechanism is totally different (see Chapter 1), these microfluidic systems have been considered outside the scope of this discussion and are not further considered.

Effect of disperse-phase viscosity

In emulsification, microfluidic Y-junctions are unique as no effect of disperse-phase viscosity on droplet size was found (see Chapter 5). In contrast, for emulsification with traditional techniques, cross-flow membranes, dead-end membranes, and flow-focusing devices (*i.e.* ψ-junctions) [11-14] the disperse-phase viscosity was found to have influence on the droplet size; for the latter even at comparable viscosities for the continuous and disperse phase. For microfluidic T-junctions some effects of continuous- and disperse-phase viscosity were observed, which are not yet fully understood [15-17].

Monodispersity

Monodisperse emulsions are advantageous compared to polydisperse emulsions as physical destabilisation processes are delayed. Microfluidic Y-junctions are suited for the production of monodisperse emulsions (see *e.g.* the polydispersity indices in Chapter 1) as a single break-up mechanism occurs, and as the contact between emulsion droplets is delayed through the specific design of the junctions, which allows surfactants more time to adsorb and therewith stabilise the droplets. Besides, from literature it is expected that monodispersity is maintained even after parallelisation of Y-junctions [18]. ψ- and T-junctions also enable delayed contact between the produced monodisperse emulsion droplets [1, 19], albeit that for T-junctions the produced emulsion droplets are less monodisperse (see Table 1).

Emulsions produced with other emulsification techniques are more polydisperse than those produced with microfluidic devices [3, 6, 20]. In membranes, this presumably results from differences in pore size and from the fact that several droplet formation mechanisms occur simultaneously [21]. Besides, when a large number of pores in a membrane is active and insufficiently stabilised droplets are formed at pores in close proximity, droplets contact already during droplet formation and this may lead to coalesce [3, 20]. Further, for microsieves Abrahamse *et al.* [22] showed that even without coalescence polydispersity can be caused by steric hindrance of incipient droplets formed at neighbouring pores.

Parallelisation

In the work of Gijsbertsen-Abrahamse *et al.* [23] various membranes and microsieves were compared based on the required area to process a specific volume of oil. No values are available for shear-driven microfluidic devices, and therefore, some calculations had to be made. The parallelisation strategies of Kawai *et al.* [18] and our own work (see Chapter 4) are evaluated for emulsification of 1 cubic meter of oil per hour based on the extreme values in production rate reported in this thesis (see Table 2).

Table 2: Details of the minimal and maximal experimental production rate f for a single microfluidic Y-junction. V is the volume of the produced emulsion droplets, and ρ_c, η_c, and v_c are the density, viscosity, and velocity of the continuous phase, respectively.

f [s^{-1}]	V [μm^3]	ρ_c [$kg \cdot m^{-3}$]	η_c [mPa·s]	v_c [$m \cdot s^{-1}$]
20833	35.6	915.8	2.7	0.63
38	1519.0	996.3	1.0	0.24

To maintain monodispersity, parallelised Y-junctions should not hinder each other when droplet formation occurs downstream from the junction (see Chapter 3 and 5). Therefore, the system suggested by Kawai *et al.* [18], where parallel Y-junctions are positioned around a central collecting area, would be suitable. This system is shown in Figure 1, and although it looks like ψ-junctions positioned around a central collecting area, emulsion droplets are formed alternately at the oppositely

positioned Y-junctions, and therewith the system is operated as parallel Y-junctions rather than as ψ-junction. Since no data on the device dimensions of the Kawai system are available, our estimation is based on dimensions by Nisisako *et al.* [1] for similarly parallelised T-junctions.

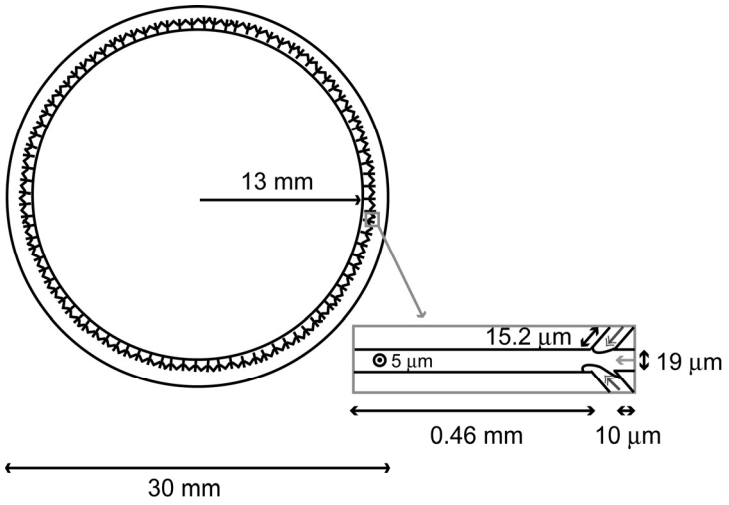

Figure 1: Outline of mass-parallelisation of Y-junctions by positioning them parallel around a circular collecting area. In the enlargement a parallel Y-junction is shown where droplets are formed alternately at the oppositely positioned Y-junctions. The continuous-phase flow in the middle is indicated by a light-grey arrow and the disperse-phase flow, which flows in from above and below, is indicated by dark-grey double-headed arrows. Dimensions are not according to scale.

Assuming channel dimensions as shown in Figure 1 †, 2015 parallel Y-junctions can be positioned around one collecting area on one disc with an assumed

† The continuous- and disperse-phase channel lengths are estimated based on the entrance length of a Newtonian fluid in laminar flow $L_{entrance}$ (*i.e.* the length where the centre line velocity is 99% developed). For Reynolds numbers *Re* between 0 and 500: $L_{entrance} = D_H(0.379\exp(-0.148Re)+0.0550Re+0.260)$, where D_H is the hydraulic diameter [24]. For the Y-junctions studied in this thesis, a value between 4 and 7 µm is found for the continuous

thickness of 1 mm. Besides, droplets are assumed to be formed alternately at parallel Y-junctions, like observed for T-junctions [1, 25], each at a productivity equal to that of a single Y-junction. As more discs are to be stacked, a spacer to supply the phases is needed with an assumed thickness of 1 mm. Table 3 shows that this design results in a volume and required area in a feasible range. Optimisation of the design enables a further decrease as shown for a collecting area diameter of 1 mm and a disc diameter of 3 mm in Table 3.

Table 3: Estimation of the device volume V_{device} and required area A_{device} that handles oil at 1 $m^3 \cdot h^{-1}$ for various shear-driven emulsification devices discussed in this chapter.

Emulsification device	V_{device} [L]	A_{device} [m^2]
Y-junctions around circular area ID=26 mm and OD=30mm (configuration Figure 1)	100-1700	8-98
Y-junctions around circular area ID=1 mm and OD=3mm	18-235	4-52
80 Y-junctions at one continuous-phase channel (configuration Figure 2)	40-500	0.9-12
500 Y-junctions at one continuous-phase channel	7-90	0.1-2
microsieve	0.05[a]	0.1[23]
ceramic membrane	2[b]	0.3[23]
SPG membrane	29[b]	7[23]

[a] The thickness of the microsieve is assumed 1 μm and the continuous-phase and disperse-phase supply channel height 260 μm [22].

[b] A tubular membrane with an outer diameter of 10 mm [26, 27] surrounded by a disperse-phase supply channel with a width of 1.25 mm is assumed, *i.e.* OD=12.5 mm.

The design with a central collecting area has already been successfully applied for Y-, T-, and ψ-junctions [1, 18]. The values given here for parallelised Y-junctions are expected to be also good estimations for T-junctions. For ψ-junctions the values should be twice as high because of their specific lay-out [1] (*i.e.* compared to Y-junctions half the number of ψ-junctions can be positioned around a central collecting area).

phase and a value of 1 μm is found for the disperse phase. The downstream channel length is the minimum studied in this thesis (see Chapter 4).

Please note that only low disperse-phase volume fractions can be attained with the parallelised Y-junction design shown in Figure 1 (see Table 4). To obtain higher disperse-phase fractions, a T-junction [2], now applied for concentration purposes, could be positioned after the parallel Y-junction to remove part of the continuous phase.

Table 4: Disperse-phase volume fractions φ of emulsions produced with the mass-parallelised Y-junction designs suggested by Kawai *et al.* [18] and in this thesis (see Figure 4a., Chapter 4).

mass-parallelised design	φ^a [%]
Y-junctions around circular area ID=26 mm and OD=30mm (configuration Figure 1)	0.5 to 2.4
Y-junctions around circular area ID=1 mm and OD=3mm	0.5 to 2.4
80 Y-junctions at one continuous-phase channel (configuration Figure 2)	1.3 to 5.9
500 Y-junctions at one continuous-phase channel	7.4 to 28.2

[a] $\varphi = (\phi_d/(\phi_c+\phi_d))*100$ %, where ϕ_d and ϕ_c are the disperse- and continuous-phase flow rate, respectively.

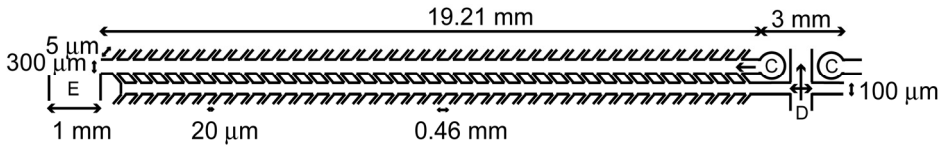

Figure 2: Outline of part of a mass-parallelised Y-junction pattern as shown in Figure 4a, Chapter 4. *C* and *D* represent the continuous-phase and disperse-phase supply, respectively, and *E* the emulsion collecting area. The device has a uniform depth of 5 µm and the single-headed arrows indicate the direction of flow. Dimensions are not according to scale.

In this thesis, another pattern to parallelise Y-junctions was suggested by positioning several Y-junctions along a straight continuous-phase channel (see Figure 2 and Chapter 4, Figure 4a.). To estimate the typical volume and the required area, two extreme situations are evaluated: droplet formation downstream from the junction and droplet formation at the junction (see Chapter 3 and 5). For droplet formation (far) downstream, a distance between subsequent Y-junctions of

0.46 mm ‡, a wafer thickness of 1 mm, and other dimensions as shown in Figure 2 are assumed.

In this case, 80 Y-junctions can be positioned per continuous-phase channel and a device volume comparable to that of the previous circular mass-parallelised design is obtained, albeit that the required area is smaller and disperse-phase volume fraction is higher (see Table 3 and 4). Assuming detachment to occur at the Y-junction, the distance between subsequent junctions can be decreased to 60 μm § and assuming other dimensions as shown in Figure 2, 500 junctions can be positioned per continuous-phase channel. This clearly brings the device volume and required area down (see Table 3) and allows production of emulsions with higher disperse-phase fraction as shown in Table 4. T-junctions can be mass-parallelised similarly to Y-junctions, and therefore comparable device volumes and areas are expected, but for ψ-junctions this design does not seem feasible.

In summary, these estimations demonstrate that processing 1 $m^3 \cdot h^{-1}$ of oil is achievable with a reasonable mass-parallelised Y-junction volume, especially when positioning 500 Y-junctions per continuous-phase channel. With respect to the device area, the mass-parallelised Y-junction designs from Figure 2 seem much more feasible than the circular ones with a central collecting area (*i.e.* Figure 1). As mentioned previously, Gijsbertsen-Abrahamse *et al.* [23] estimated the required membrane and microsieve area for culinary cream production. For 1 $m^3 \cdot h^{-1}$ of oil this results in the volumes and the areas shown in Table 3. The volume values for microsieves are lowest, followed by mass-parallelised Y-junctions, which give similar values as membranes. The values for the area are comparable for Y-junctions parallelised according to Figure 2, microsieves, and ceramic membranes; the SPG membranes and Y-junctions parallelised around a central collecting area are roughly one order of magnitude higher. According to Table 3 especially the design with 500 Y-junctions along one continuous–phase channel shows true

‡ This is the minimal downstream channel length studied in this thesis (see Chapter 4).

§ In our experiments, the incipient droplet moved at most 57 μm downstream before detaching at the corner of the Y-junction.

potential for application on large scale. Nevertheless, to make this a reality the design of the stack, *e.g.* the pressure drop in the entire system and the effect of droplet formation on the cross-flow at neighbouring junctions, needs to be investigated in more detail.

Energy efficiency

Generally, it is assumed that the energy input into microfluidic devices is low. However, due to the small dimensions of the microchannels in our Y-junctions, the pressure drop and therefore the energy input are rather high. To give an impression, the energy density of Y-junctions is compared to other emulsification devices [6, 11, 28-30] (see Figure 1). For Y-junctions, the energy density was defined as the pressure drop of the continuous phase over the total length of the continuous-phase channel and the downstream channel (see *e.g.* previous chapter) as calculated with the Bernoulli equation [**].

Figure 3 shows that the overall energy input into microfluidic Y-junctions resembles that of colloid mills, rotor-stator systems, and high-pressure homogenisers; that is if Y-junctions are designed exactly as used in this thesis with relatively long channels, *i.e.* large pressure drops. For other shear-driven microfluidic devices, comparable energy densities are expected if channel dimensions are comparable. Decreasing the continuous-phase channel length to the entrance length [24] (*i.e.* 4 to 7 μm, see footnote on page 123) and assuming no effect on droplet size, results in an energy density between $5 \cdot 10^3$ and $3 \cdot 10^6$ $J \cdot m^{-3}$, therewith bringing this technique closer to membrane emulsification in regard of energy usage (see Figure 3).

[**] The pressure drop ΔP is calculated for laminar flow neglecting the kink in the channel (contribution < 0.01%): $\Delta P = 0.5((16L_C)/(Re_{c,C}R_{H,C}))\rho_c v^2_{c,C} + 0.5((16L_E)/(Re_{c,E}R_{H,E}))\rho_c v^2_{c,E}$, where subscripts C and E relate to continuous and downstream channel, respectively, L is the microchannel length, Re_c is the Reynolds number of the continuous phase, R_H is the hydraulic radius, ρ_c and v_c are the continuous phase density and velocity, respectively [31, 32].

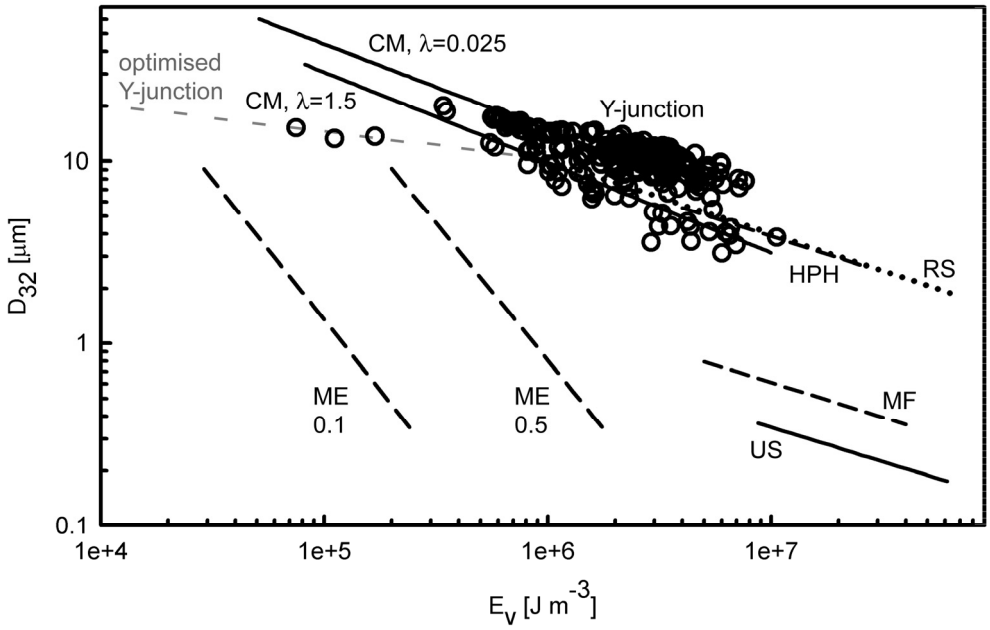

Figure 3: Sauter droplet diameter D_{32} as function of energy density E_V for various emulsification devices: ME is cross-flow membrane emulsification and the numbers denote the disperse-phase fraction, CM is colloid mill and the numbers denote the (dynamic) disperse-to-continuous-phase viscosity ratio λ, RS is rotor-stator, HPH is high-pressure homogeniser, MF is microfluidiser, and US is ultrasonic generator. The spheres (o) are the Y-junction data from this thesis, the solid lines are reprinted from Walstra *et al.* [29], the dashed lines are reprinted from Lambrich *et al.* [6], and the dotted lines are reprinted from Eisner [33]. The grey dashed line is a rough estimation of the Y-junctions after optimisation by decreasing the continuous-phase channel length to the entrance length and assuming no effect on droplet size.

Maturation of emulsification with microfluidic Y-junctions

The previous sections showed that emulsification with microfluidic Y-junctions has potential, especially when monodisperse emulsions are required and when the Y-junction design can be optimised, including adaptation for production of smaller emulsion droplets. The latter was not targeted as our current microfluidic Y-junction design was optimised for experimental observation, *i.e.* for the formation of

droplets which can be observed and recorded with a high-speed camera connected to a light microscope.

The droplet formation mechanism in microfluidic Y-junctions is well understood, as described in Chapter 3, 4, and 5, except for the neck diameter just before detachment (see Chapter 5). Currently this is the only parameter that needs to be measured in the force-balance model used to predict the droplet size at Y-junctions, and therefore, it would be worthwhile to investigate whether a closing relation can be found. Such a relation would allow complete prediction of the droplet size as function of the process and material properties. The findings from this thesis may serve as a starting point, as it was found that the neck diameter is influenced by the disperse phase and the capillary number of the continuous phase (see Chapter 4 and 5). Besides, it can be expected that the contact angle between the disperse-phase liquid column, the continuous phase, and the wall will be of influence.

Dynamic interfacial tension

A parameter that is very difficult to quantify during emulsification in shear-driven microfluidic devices is the dynamic interfacial tension. This may seem contradictory since the interfacial tension is an essential parameter in the various scaling relations published for shear-driven microfluidic devices (see *e.g.* Chapter 2, 3, and 5). However, dynamic interfacial tension measurement at these conditions is far from trivial.

In Chapter 6, (apparent) dynamic interfacial tension effects were quantified at sub-millisecond timescales relevant to droplet formation at Y-junctions. For liquid-liquid interfaces this timescale was not assessed before. A decrease in the apparent dynamic interfacial tension was shown with an increase in surfactant concentration, a decrease in molecular weight of the surfactant, and a decrease in the disperse-phase flow rate. Therefore, the presence of surfactants disperse-phase flow rate indirectly influences the droplet size at microfluidic Y-junctions. Similar

effects on dynamic interfacial tension were observed for surfactants (generally SDS and Tween 20) in emulsification with cross-flow ceramic membranes [20], microfluidic T-junctions [8], and at a single pore [34], albeit in the millisecond timescale. The unique feature of microfluidic Y-junctions is that they allow tuning of the droplet size through the (apparent) dynamic interfacial tension, which might lead to scaling relations in which the actual interfacial tension value is used as a design parameter.

Applications and outlook

Currently, Y-junctions are only used to form spherical microcapsules or single emulsions [18, 35, 36]. Y-junctions in serial order could be deployed to form complex emulsions, *i.e.* an emulsion in an emulsion. A possible application of these complex emulsions could be 'light' products as the oil content can be decreased by inclusion of water droplets into the oil droplet. Alternatively, capsules can be made, for which commercial interest is foreseen, due to the micrometer size of the generated droplets, and even more importantly their monodispersity, which allows specific and accurate dosage. Further, Y-junctions may also be used to prepare foams by dispersing air in liquid, although this may prove difficult since the high pressure compresses the air that will later expand upon leaving the device, or in extreme cases may dissolve in the liquid without generating bubbles.

Ideally, emulsification with microfluidic Y-junctions results in emulsions with small monodisperse droplets and high disperse-phase fractions. Besides, throughputs are high and energy input is low. Based on the estimations discussed in this chapter, this seems most feasible through mass-parallelisation by positioning several Y-junctions at one continuous-phase channel. However, mass-parallelised operation in this configuration has not yet been experimentally demonstrated and therefore new challenges can be expected in practical realisation, *e.g.* emulsion droplets might start to wet the walls during operation. However, various surface modification methods that have recently become available are a step in the right direction towards stable operation of mass-parallelised Y-junctions for a prolonged

period [37, 38]. Therefore, we think that emulsification with microfluidic Y-junctions has clear potential.

References

1. T. Nisisako and T. Torii, *Lab On A Chip*, 2008, **8**, 287-293.
2. P. Panizza, W. Engl, C. Hany and R. Backov, *Colloids and Surfaces a-Physicochemical and Engineering Aspects*, 2008, **312**, 24-31.
3. C. Charcosset, *Journal of Food Engineering*, 2009, **92**, 241-249.
4. T. Nisisako, T. Torii and T. Higuchi, *Chemical Engineering Journal*, 2004, **101**, 23-29.
5. P. Garstecki, H. A. Stone and G. M. Whitesides, *Physical Review Letters*, 2005, **94**, 164501-164501-164501-164504.
6. U. Lambrich and H. Schubert, *Journal of Membrane Science*, 2005, **257**, 76-84.
7. R. Katoh, Y. Asano, A. Furuya, K. Sotoyama and M. Tomita, *Journal of Membrane Science*, 1996, **113**, 131-135.
8. S. v. d. Graaf, M. L. J. Steegmans, R. G. M. v. d. Sman, C. G. P. H. Schroën and R. M. Boom, *Colloids and Surfaces A-Physicochemical and Engineering Aspects*, 2005, **266**, 106-116.
9. S. L. Anna, N. Bontoux and H. A. Stone, *Applied Physics Letters*, 2003, **82**, 364-366.
10. K. C. van Dijke, K. Schroën and R. M. Boom, *Langmuir*, 2008, **24**, 10107-10115.
11. S. Schultz, G. Wagner, K. Urban and J. Ulrich, *Chemical Engineering & Technology*, 2004, **27**, 361-368.
12. Z. Nie, M. Seo, S. Xu, P. C. Lewis, M. Mok, E. Kumacheva, G. M. Whitesides, P. Garstecki and H. A. Stone, *Microfluidics and Nanofluidics*, 2008, **5**, 585-594.
13. D. X. Hao, F. L. Gong, G. A. Hu, Y. J. Zhao, G. P. Lian, M. Guang-Hui and Z. Su, *Industrial and Engineering Chemistry Research*, 2008, **47**, 6418-6425.

14. M. Kukizaki, *Journal of Membrane Science*, 2009, **327**, 234-243.
15. P. Garstecki, M. J. Fuerstman, H. A. Stone and G. M. Whitesides, *Lab On A Chip*, 2006, **6**, 437-446.
16. J. H. Xu, S. W. Li, J. Tan, Y. J. Wang and G. S. Luo, *Aiche Journal*, 2006, **52**, 3005-3010.
17. J. D. Tice, A. D. Lyon and R. F. Ismagilov, *Analytica Chimica Acta*, 2004, **507**, 73-77.
18. A. Kawai, S. Matsumoto, H. Kiriya, T. Oikawa, K. Hara, T. Ohkawa, T. Futami, K. Katayama and K. Nishizawa, *TOSOH Research and Technology Review*, 2003, **47**, 3-9.
19. J. Baret, F. Kleinschmidt, A. El Harak and A. D. Griffiths, *Langmuir*, 2009.
20. V. Schröder, O. Behrend and H. Schubert, *Journal of Colloid and Interface Science*, 1998, **202**, 334-340.
21. G. T. Vladisavljevic, I. Kobayashi, M. Nakajima, R. A. Williams, M. Shimizu and T. Nakashima, *Journal of Membrane Science*, 2007, **302**, 243-253.
22. A. J. Abrahamse, R. Van Lierop, R. G. M. Van der Sman, A. Van der Padt and R. M. Boom, *Journal of Membrane Science*, 2002, **204**, 125-137.
23. A. J. Gijsbertsen-Abrahamse, A. van der Padt and R. M. Boom, *Journal of Membrane Science*, 2004, **230**, 149-159.
24. N. Dombrowski, A. Foumeny, S. Ookawara and A. Riza, *The Canadian Journal of Chemical Engineering*, 1993, **71**, 472-476.
25. S. Okushima, T. Nisisako, T. Torii and T. Higuchi, *Langmuir*, 2004, **20**, 9905-9908.
26. S. M. Joscelyne and G. Trägårdh, *Journal of Food Engineering*, 1999, **39**, 59-64.
27. G. T. Vladisavljevic and H. Schubert, *Desalination*, 2002, **144**, 167-172.
28. H. Karbstein and H. Schubert, *Chemical Engineering and Processing*, 1995, **34**, 205-211.
29. P. Walstra and P. E. A. Smulders, in *Modern aspects of emulsion science*, ed. B. P. Binks, The royal Society of Chemistry, Cambridge, 1998, pp. 56-99.
30. E. A. van der Zwan, C. Schroen and R. M. Boom, *Aiche Journal*, 2008, **54**, 2190-2197.

31. D. W. Green and R. H. Perry, *Perry's chemical engineers' handbook*, 8th edn., McGraw-Hill, New York, 2007.
32. L. P. B. M. Janssen and M. M. C. G. Warmoeskerken, *Transport phenomena data companion*, 3rd edn., Delft University Press, Delft, 2001.
33. V. Eisner, *Emulsion processing with a rotating membrane*, ETH Zurich, 2007.
34. S. v. d. Graaf, C. G. P. H. Schroën, R. G. M. v. d. Sman and R. M. Boom, *Journal of Colloid and Interface Science*, 2004, **277**, 456-463.
35. L. Capretto, S. Mazzitelli, C. Balestra, A. Tosi and C. Nastruzzi, *Lab on a Chip*, 2008, **8**, 617-621.
36. A. Kubo, H. Shinmori and T. Takeuchi, *Chemistry Letters*, 2006, **35**, 588-589.
37. M. Rosso, M. Giesbers, A. Arafat, K. Schroen and H. Zuilhof, *Langmuir*, 2009, **25**, 2172-2180.
38. A. Arafat, M. Giesbers, M. Rosso, E. J. R. Sudholter, K. Schroen, R. G. White, L. Yang, M. R. Linford and H. Zuilhof, *Langmuir*, 2007, **23**, 6233-6244.

Summary

On a daily basis, we encounter many emulsion-based products such as butter or sun cream, which consist of oil droplets in water, or water droplets in oil. Traditionally, these emulsions are produced with systems that allow a high throughput, but yield a broad droplet size distribution. Therefore, the industry is interested in emulsification techniques that give more monodisperse emulsions, such as emulsification with microfluidic devices, *i.e.* defined geometries with channel diameters in the order of several to hundreds of micrometers.

The goal of this thesis was to develop a new microfluidic emulsification technique that has the potential to be scaled up for the production of large volumes of monodisperse emulsion. We chose to study shear-driven microfluidic devices, *i.e.* T- and Y-junctions, due to their high productivity per junction and their potential for mass-parallelisation. However, reliable application of these junctions is only possible when the droplet-formation mechanism and droplet size determining parameters are fully understood. Therefore, we took a single junction both as a starting and as a focal point of this thesis.

The thesis starts off by indicating and quantifying the parameters that determine droplet size in microfluidic T-junctions. In literature, (monodisperse) emulsification at T-junctions is studied for a broad range of channel dimensions, flow rates, and materials. However, it is not yet clear which parameters determine the droplet size. Therefore, in Chapter 2 statistical analysis is used to quantitatively relate droplet size data from various literature sources. For T-junctions it is found that emulsion droplet size of drops, discs, and plugs can be described by a two-step model consisting of a droplet growth and a droplet detachment step. This suggests that an emulsion droplet grows until a certain volume is reached, after which it starts to detach. The channel dimensions determine droplet growth, while the continuous-

and the disperse-phase flow rate determine the abating time (*i.e.* the fast decrease of the neck resulting in detachment).

In the remainder of this thesis microfluidic (flat) Y-junctions are discussed; they resemble T-junctions, but are hardly studied in literature. In Chapter 3, emulsification of hexadecane in various ethanol-water mixtures at different process conditions, *i.e.* flow rates and static interfacial tensions, is experimentally investigated. We focus on droplet formation at the Y-junction or downstream without the incipient droplet blocking the downstream channel (*i.e.* the dripping and the jetting regime). For Y-junctions, the droplet size is described with a force balance between the interfacial tension force and the shear force at the point where the incipient droplet is kept to the bulk by a neck. It is found that the droplet size at Y-junctions is determined by the interfacial tension, the channel dimensions, and the viscosity and flow rate of the continuous phase; but not by the flow rate of the disperse phase. This makes operation of Y-junctions intrinsically easier than T-junctions, for which the flow rates of both phases need to be (accurately) controlled.

Where Chapter 3 concentrates on process conditions, in Chapter 4 the effect of (Y-) junction design on the droplet size is investigated. In five different Y-junction geometries and one T-junction with a depth of 5 μm, hexadecane is emulsified in ethanol-water mixtures at a given static interfacial tension and at various process conditions, *e.g.* flow rates. For the various Y-junctions, no effect on droplet size is observed from the junction angle and the length(s) and/or the width(s) of the microchannel(s). In contrast, significant differences are observed between T- and Y-junctions.

In Chapter 5, the force balance, found in Chapter 3, is extended by including the effect of the viscosity of the disperse phase and a broader range of viscosities and/or flow rates of the continuous phase. The force balance is mainly adapted by rewriting the shear force from the drag force on a sphere to the drag force on the cross-sectional area of the squeezed incipient droplet (head). It is found that the emulsion droplet size at Y-junctions is determined by the interfacial tension, the

channel dimensions, the viscosity, density, and flow rate of the continuous phase, and the resistance with the wall. The influence of the viscosity of the disperse phase and the viscosity ratio were found negligible, just as the disperse-phase flow rate.

The first five chapters show that droplet size at microfluidic Y-junctions is strongly influenced by the interfacial tension and therefore it is important to quantify its value under dynamic conditions. Traditional tensiometric techniques do not allow interfacial tension measurement under the conditions applied in Y-junctions: high shear and droplet formation in less than milliseconds. Therefore, in Chapter 6, (monodisperse) emulsification at microfluidic Y-junctions is proposed as a new tensiometric technique. A calibration curve is derived for hexadecane in various ethanol-water mixtures with a range of static interfacial tensions. Subsequently, this curve is used to estimate the apparent dynamic interfacial tension for solutions with the surfactants SDS or Synperonic PEF108. The apparent dynamic interfacial tension is found to be determined by the flow rates of the continuous and disperse phase, the surfactant and its concentration. In addition, we showed that surfactant transport in Y-junctions is dominated by convection.

In Chapter 7, the thesis is concluded by comparing emulsification with microfluidic Y-junctions to other shear-driven microfluidic geometries with cross-flow membrane emulsification as a benchmark technology. Especially, the negligible effect of the flow rate and the viscosity of the disperse phase on the droplet size makes microfluidic Y-junctions unique. To illustrate the large-scale feasibility of microfluidic Y-junctions, typical emulsification device volumes and required areas to process 1 $m^3 \cdot h^{-1}$ of disperse phase were calculated. The requirements are found to be comparable to values obtained from literature for membranes and microsieves. The energy input of the current microfluidic Y-junction design is comparable to traditional emulsification techniques, but since there is room for optimisation, we are hopeful that these values may well be reduced.

Samenvatting

In het dagelijks leven gebruiken we veel producten gebaseerd op emulsies, zoals boter en zonnebrandcrème, die bestaan uit oliedruppels in water of waterdruppels in olie. Deze producten worden gemaakt met traditionele emulgeertechnieken die in korte tijd grote hoeveelheden emulsie kunnen produceren. De emulsiedruppels zijn echter niet allemaal even groot, oftewel de emulsie is polydispers. Daarom heeft de industrie belangstelling voor nieuwe emulgeertechnieken die druppels van gelijke grootte maken (monodisperse emulsies), zoals emulgeren met microstructuren. Bij deze techniek worden kanalen met een breedte van enkele tot honderden micrometers op een specifieke manier ten opzichte van elkaar geplaatst om op deze manier emulsies te maken.

Het doel van dit proefschrift was het ontwikkelen van een nieuwe microstructuur die geschikt is om grote hoeveelheden monodisperse emulsie te kunnen produceren. We hebben gekozen om te kijken naar microstructuren waarin druppels worden gevormd door middel van afschuiving, zoals T- en Y-splitsingen, omdat deze een hoge productiviteit (druppelvormingssnelheid) per splitsing hebben en omdat vele splitsingen parallel kunnen worden geschakeld. Deze microstructuren kunnen echter alleen betrouwbaar worden toegepast als het druppelvormings-mechanisme en de variabelen van invloed op de druppelgrootte worden begrepen. Daarom legt dit proefschrift zich toe op individuele T- en Y-splitsingen.

Het proefschrift begint met het aanwijzen en kwantificeren van de druppelgrootte bepalende variabelen in T-splitsingen. In de literatuur is (monodispers) emulgeren met T-splitsingen bestudeerd voor een breed scala aan kanaalafmetingen, stroomsnelheden en materialen. Desalniettemin is het onduidelijk welke variabelen de druppelgrootte bepalen. In hoofdstuk 2 wordt daarom statistische analyse gebruikt om data van verschillende bronnen samen te brengen. Voor T-splitsingen

wordt gevonden dat de druppelgrootte van zowel ronde, schijfvormige en buisvormige emulsiedruppels kan worden beschreven met een tweestapsmodel bestaande uit een druppelgroei- en afbreekfase. Dit suggereert dat een druppel eerst groeit tot een specifiek volume, waarna deze begint af te breken. Hierbij wordt de druppelgroei bepaald door de kanaalafmetingen, terwijl de tijd voor afbreken wordt bepaald door het debiet van de continue en disperse fase.

De overige hoofdstukken van dit proefschrift richten zich op (platte) Y-splitsingen; deze lijken veel op T-splitsingen, maar worden nauwelijks bestudeerd in de literatuur. Hoofdstuk 3 beschrijft het emulgeren van hexadecaan in verschillende ethanol-water mengsels bij verschillende procescondities, zoals het debiet en de statische grensvlakspanning. Hierbij beperken we ons tot emulsiedruppels die tijdens hun groei het kanaal niet blokkeren (met andere woorden het 'dripping' en het 'jetting' regime). Voor Y-splitsingen wordt de emulsiedruppelgrootte beschreven door een balans tussen de grensvlakspanningskracht en de afschuifkracht op het punt waar de groeiende druppel door een nek wordt vastgehouden aan de rest van de disperse fase. De druppelgrootte wordt bepaald door de grensvlakspanning, de kanaalafmetingen, de viscositeit en het debiet van de continue fase. Het debiet van de disperse fase blijkt geen effect te hebben, wat betekent dat Y-splitsingen makkelijker te gebruiken zijn dan T-splitsingen, waarvoor het debiet van beide fasen (nauwkeurig) moeten worden gecontroleerd.

Terwijl hoofdstuk 3 zich toelegt op procescondities, wordt in hoofdstuk 4 het effect van het ontwerp van een (Y-)splitsing op de druppelgrootte onderzocht. Vijf verschillende Y-splitsingen en één T-splitsing met een diepte van 5 μm worden gebruikt om hexadecaan te emulgeren in verschillende ethanol-water mengsels bij verschillende procescondities, zoals het debiet en de statische grensvlakspanning. Voor de verschillende Y-splitsingen wordt geen effect van de hoek waaronder de kanalen bij elkaar komen en de lengte(s) en/of de breedte(s) van de kanalen op de druppelgrootte gevonden. Tussen T- en Y-splitsingen daarentegen worden wel duidelijke verschillen waargenomen.

In hoofdstuk 5 wordt de krachtenbalans, afgeleid in hoofdstuk 3, uitgebreid met het effect van de viscositeit van de disperse fase en een breder scala aan viscositeiten en/of debieten van de continue fase. De grootste verandering in de krachtenbalans is het omschrijven van de afschuifkracht op basis van de sleepkracht op een druppel naar de sleepkracht op de dwarsdoorsnede van de vervormde groeiende druppel. Op basis van deze herziene krachtenbalans wordt de druppelgrootte in Y-splitsingen bepaald door de grensvlakspanning, de kanaalafmetingen, de weerstand met de kanaalwand, de viscositeit, de dichtheid en het debiet van de continue fase. De viscositeit van de disperse fase en de viscositeitverhouding blijken geen effect te hebben, net zoals het debiet van de disperse fase.

De eerste vijf hoofdstukken laten zien dat de druppelgrootte in Y-splitsingen sterk wordt beïnvloed door de grensvlakspanning en daarom is het belangrijke om deze in dynamische systemen te kunnen bepalen. Met traditionele technieken voor het meten van de grensvlakspanning (tensiometrie) is dit onmogelijk, omdat de afschuifsnelheden in Y-splitsingen hoog zijn en druppels in minder dan milliseconden worden gevormd. Daarom wordt in hoofdstuk 6 (monodispers) emulgeren met Y-splitsingen geïntroduceerd als een nieuwe techniek voor het meten van grensvlakspanningen. De basis van deze techniek is een calibratiecurve afgeleid voor hexadecaan in ethanol-water mengsels met verschillende statische grensvlakspanningen. Deze curve is vervolgens gebruikt om de effectieve dynamische grensvlakspanning te schatten voor oplossingen van de surfactants SDS en Synperonic PEF108. De effectieve dynamische grensvlakspanning blijkt te worden bepaald door het debiet van de disperse en continue fase, het type surfactant en zijn concentratie. Daarnaast laat dit hoofdstuk zien dat transport van surfactants in Y-splitsingen wordt gedomineerd door convectie.

In hoofdstuk 7 wordt het proefschrift afgesloten met een vergelijking tussen emulgeren met Y-splitsingen en andere strominggedreven microstructuren met langsstroom (‘cross-flow’) membraan emulgeren als een referentietechniek. Vooral het feit dat het debiet en de viscositeit van de disperse fase geen effect op de druppelgrootte hebben, maakt Y-splitsingen uniek. Om de haalbaarheid van

grootschalige toepassing van Y-splitsingen te illustreren, zijn het systeemvolume en het oppervlak berekend om 1 kubieke meter olie (disperse fase) per uur te verwerken. De waarden zijn vergelijkbaar met literatuur data voor membranen en microzeven. De energie-input nodig voor de huidige Y-splitsing is vergelijkbaar met die van traditionele emulgeertechnieken, maar aangezien er ruimte is voor optimalisatie, is het waarschijnlijk dat deze waarden nog aanzienlijk verlaagd kunnen worden.